

Clemson University

TigerPrints

All Theses

Theses

8-2021

A Manufacturing-To-Response Pathway for Formed Carbon Fiber Reinforced Polymer Composite Structures

Madhura Limaye

Clemson University, mlimaye@clemson.edu

Follow this and additional works at: https://tigerprints.clemson.edu/all_theses



Part of the [Applied Mechanics Commons](#), [Computer-Aided Engineering and Design Commons](#), and the [Manufacturing Commons](#)

Recommended Citation

Limaye, Madhura, "A Manufacturing-To-Response Pathway for Formed Carbon Fiber Reinforced Polymer Composite Structures" (2021). *All Theses*. 4067.

https://tigerprints.clemson.edu/all_theses/4067

This Thesis is brought to you for free and open access by the Theses at TigerPrints. It has been accepted for inclusion in All Theses by an authorized administrator of TigerPrints. For more information, please contact kokeefe@clemson.edu.

A MANUFACTURING-TO-RESPONSE PATHWAY FOR FORMED CARBON
FIBER REINFORCED POLYMER COMPOSITE STRUCTURES

A Thesis
Presented to
the Graduate School of
Clemson University

In Partial Fulfillment
of the Requirements for the Degree
Master of Science
Mechanical Engineering

by
Madhura Vidyadhar Limaye
August 2021

Accepted by:
Dr. Gang Li, Committee Chair
Dr. Srikanth Pilla, Committee member
Dr. Oliver J. Myers, Committee member

ABSTRACT

Over the past decade, there has been an increased adoption of thermoplastic and thermoset based continuous carbon fiber reinforced polymer (CFRP) composites for structural applications in several industries. Among the different manufacturing methods, thermoforming process for thermoplastic based continuous CFRP's offer a major advantage in reducing cycle times for large scale productions. Similarly, out-of-autoclave curing process for thermoset based continuous CFRP's using heated tooling enables production of large composite structures. However, these manufacturing processes can have a significant impact on the structural performance of parts by inducing undesirable effects. These effects include inhomogeneous fiber orientations, thickness variations, and residual stresses in the formed CFRP structures. This necessitates the development of an optimal manufacturing process that minimizes the introduction of the undesirable factors in the structure and thereby achieves the targeted mechanical performance. This can be done by first establishing a relationship between manufacturing process and mechanical performance and successively optimizing it to achieve the desired targets. To this end, a few attempts have been made to connect the design, manufacturing, and structural simulation steps in series, by developing virtual process chains (CAE chains) and mapping methods. However, the recent publications implementing these methods are missing some of the relevant effects or steps of the manufacturing process.

The present work establishes two Manufacturing-to-Response (MTR) pathways for end-to-end analysis of CFRP composite structures. The current study focuses on establishing a relationship between manufacturing process and mechanical performance.

As case studies, the MTR pathway was implemented for 1. thermoplastic based Composite Hat structure manufactured by thermoforming process and 2. thermoset based Composite Boom structure manufactured by Out-of-Autoclave (OOA) molding process using self-heated tool. The pathway primarily comprised of material characterization, finite element simulations and experimental validation. The first case study details the MTR pathway for thermoforming process of Composite Hat structure. Thermoforming process effects were studied and incorporated in structural analysis. The second case study details a framework of the MTR pathway for OOA molding of Composite Boom structure. The first two steps of the pathway namely Composite boom tool design and curing analysis were accomplished as a part of the present study. The MTR pathway(s) were validated experimentally for the Composite Hat structure and validation for the Composite Boom structure is planned for future work. Both studies indicated the significance of incorporating the manufacturing process effects into the structural performance of a composite structure.

DEDICATION

I dedicate this thesis work to my family and friends, especially my grandparents, parents, Seema and Vidyadhar Limaye, brother Chinmay Limaye and sister-in-law Sanika Parchure Limaye and my dear friend Aishwarya Patwardhan for their constant support and encouragement during my graduate studies.

ACKNOWLEDGMENTS

Foremost, I sincerely thank my advisor Dr. Gang Li for believing and strongly supporting me throughout the course my graduate research work. His constant motivation and valuable guidance helped me learn and grow as a research student. He has provided me with unique opportunities which allowed me to work on some challenging yet exciting research tasks. I am glad and look forward to continuing working with him for my PhD study.

I would like to thank Dr. Srikanth Pilla for his substantial contribution in terms of guidance, suggestions, and feedback in my thesis work. I would not have been able to successfully complete the critical part of my research without his backing and support. I take this opportunity to also thank Dr. Oliver J Myers for teaching me Advanced Strength of materials course and extending cooperation and support through my thesis effort. Special thanks to Dr. Lonny Thompson for teaching me Finite Element Analysis courses that built a strong foundation for my research work.

A big thanks to my research colleagues Anmol Kothari and Sai Aditya Pradeep from whom I have learned a great deal and have always been a huge source of help and encouragement.

Just as importantly, I would like to thank my family and friends for their unconditional love, blessings, and enormous encouragement to pursue my dreams.

TABLE OF CONTENTS

	Page
TITLE PAGE	i
ABSTRACT	ii
DEDICATION	iv
ACKNOWLEDGMENTS	v
TABLE OF CONTENTS.....	vi
LIST OF TABLES.....	ix
LIST OF FIGURES	x
CHAPTER 1 : INTRODUCTION	1
1.1 Introduction to Composites.....	1
1.2 Fiber reinforced Polymer Composites	1
1.3 Continuous and Discontinuous Fiber reinforced polymer composites.....	2
1.4 Continuous Carbon Fiber Reinforced Polymer composites (continuous CFRPs)	3
1.5 Manufacturing Processes of continuous CFRPs.....	4
1.5.1 Thermoforming.....	4
1.5.2 Out-of-autoclave molding using self-heated tool	5
1.6 Development of composite structures for load-bearing applications	6
1.7 Literature review on development of composite structures	7
1.8 Virtual process chains for development of CFRP structures	9
1.9 Thesis Organization	12
CHAPTER 2 : MTR PATHWAY FOR THERMOFORMED THERMOPLASTIC COMPOSITE HAT STRUCTURE	13
2.1 Introduction and motivation.....	13
2.2 Manufacturing-to-response pathway	16
2.3 Experimental setup for material characterization and model validation	19
2.3.1 Material characterization for thermoforming analysis.....	19

2.3.2	Material characterization for cooling analysis and residual stresses calculation	21
2.3.3	Material characterization for mechanical analysis.....	23
2.3.4	Experimental tests for model validation	24
2.3.4.1	Hat section fabrication (thermoforming setup).....	25
2.3.4.2	Three-point bend test	28
2.3.4.3	Dynamic Tests	29
2.4	Modeling pathway	29
2.4.1	Thermoforming simulation	30
2.4.2	Cooling analysis.....	33
2.4.2.1	Heat transfer analysis.....	34
2.4.2.1	Determination of residual stresses	37
2.4.3	Mapping of numerical results	42
2.4.4	Mechanical performance validation.....	43
2.4.4.1	Quasi-static three-point bend test.....	43
2.4.4.2	Dynamic impact test	44
2.4.5	Numerical parametric study: Static and dynamic analysis	47
2.4.5.1	Static analysis.....	48
2.4.5.2	Dynamic analysis	49
2.5	Results and discussion	50
2.5.1	Model validation (Experimental vs numerical)	50
2.5.1.1	Thermoforming results: Thickness variation and Fiber Orientations	50
2.5.1.2	Residual stresses: validation and results	54
2.5.2	Mechanical performance validation.....	58
2.5.2.1	Quasi static test validation	58
2.5.2.2	Dynamic impact test validation	60
2.5.3	Numerical parametric study: manufacturing process effects on static and dynamic response.....	63
2.5.3.1	Thickness variation	63
2.5.3.2	Fiber orientations variation.....	67
2.5.3.3	Cooling rate variation	73
2.6	Conclusion	77

CHAPTER 3 : MTR PATHWAY FOR OUT-OF-AUTOCLAVE MOLDED THERMOSET COMPOSITE BOOM STRUCTURE 80

3.1	Introduction to Composite Boom structures.....	80
3.1.1.	Self-heated Composite Boom Tool.....	81
3.2	Manufacturing-to-Response Pathway.....	85
3.3	Modeling Pathway	87
3.3.1	Heat transfer analysis.....	87
3.3.1.1	Composite Boom Tool Model setup	89
3.3.1.2	Model validation: Experimental method and Computational models for Flat Plate cases.....	92

3.3.2	Curing analysis.....	97
3.3.2.1	Thermo-chemical analysis.....	99
3.3.2.2	Flow-compaction analysis.....	101
3.3.2.3	Stress-Deformation analysis.....	103
3.3.2.4	Model Cases	105
3.4	Results and Discussion	105
3.4.1	Model Validation results.....	105
3.4.1.1	Case 1: CFOAM plate.....	109
3.4.1.2	Case 2: CFOAM plate + 0.25mm SS400 heat spreader.....	110
3.4.1.3	Case 3: CFOAM plate + 0.25mm SS400 heat spreader + BMI laminate (12 plys)	111
3.4.1.4	Case 4: Graphite plate	112
3.4.2	2D Heat Transfer analysis results	113
3.4.2.1	Optimization approach	113
3.4.2.2	Design of experiments (DOE).....	114
3.4.2.3	Results of model concepts.....	117
3.4.2.4	Summary of Composite Boom tool design results.....	126
3.4.3	Cure simulation results	127
3.4.3.1	Case 1	128
3.4.3.2	Case 2	132
3.5	Conclusions and Future work	134
CHAPTER 4 : CONCLUSIONS		137
REFERENCES		139
APPENDICES		145

LIST OF TABLES

Table	Page
Table 2.1: Material properties for cooling analysis	22
Table 2.2: Average mechanical properties for investigated woven Carbon/PA6 composite	24
Table 2.3: Fiber orientations in degree from experiments and simulation at four locations on the hat structure.....	53
Table 2.4: Magnitude of residual stresses ($\sigma_z, \sigma_x, \sigma_y, \sigma_{xy}$) at Surface, $h = \pm 1$ and center, $h = 0$ plies	57
Table 2.5: Dynamic impact test comparing experiment and numerical performance	63
Table 2.6: Static performance: effects of variation in thickness distribution	64
Table 2.7: Static performance for the two orientation variants	69
Table 2.8: Static performance at different cooling rates.....	75
Table 3.1: Material properties used for the transient heat transfer analysis	107
Table 3.2: Flat Plate test cases	109
Table 3.3: Composite Boom tool thermal analysis results for CFOAM and GFOAM core concepts.....	120
Table 3.4 Material properties used for cure analysis	128

LIST OF FIGURES

Figure	Page
Figure 1.1: (a) Random and aligned/biased orientation of discontinuous fiber reinforced polymer composites (DicoFRPs), (b) Unidirectional and laminated continuous fiber reinforced polymer composites (CoFRPs).....	3
Figure 1.2: (a) Unidirectional carbon fiber prepreg, (b) Woven (2*2 Twill) carbon fiber prepreg	4
Figure 1.3: Thermoforming process steps of thermoplastic FRPs [21]	5
Figure 1.4: A comparison between autoclave, oven and self-heated tool molding processes [23].....	6
Figure 1.5: Conventional development process of structures/components for load-bearing composite structures.....	7
Figure 1.6: (a) Fiber orientation variations in a hemispherical dome [27], (b) thickness variations in a hat structure [28], and (c) residual stress induced warpage in an L-shaped structure [29].....	8
Figure 1.7: Virtual process chain developed for Resin transfer molding (RTM) process [35].....	10
Figure 1.8: “Building-block approach” implemented for development of thermoplastic CFRP component [28].	11
Figure 2.1: Driver side front door of an OEM’s mid-size luxury crossover selected for light-weighting.....	14
Figure 2.2: Structural components of the ultralightweight door.....	15
Figure 2.3: Location of the hat section on the inner frame of the light-weight door used to implement the MTR pathway	16
Figure 2.4: Manufacturing-to-response (MTR) pathway.....	18
Figure 2.5: Composite specimen under the bias-extension test (a) undeformed and (b) deformed configurations (after Lebrun et al. [43]).	21
Figure 2.6: (a) Thermal chamber equipped with thermocouple data acquisition system and.....	27

Figure 2.7: Thermocouple data for punch, die and blank during thermoforming process showing heating, forming and cooling phases.....	27
Figure 2.8: (a) Dimensions of bonded hat structure (b) Experimental setup for 3-point bend test showing the bonded hat structure, supports and punch.	28
Figure 2.9: Experimental setup for dynamic tests showing the constrained hat structure, support, constraints and punch.....	29
Figure 2.10: (a) Finite element model for forming simulations showing components namely punch, die, blank, binder tabs and forming direction, (b) dimensions and arrangement of components in cross-section view	31
Figure 2.11: Warp and weft tows of the continuous fiber reinforced composite sheet	32
Figure 2.12: (a) Finite element 3D model setup in global coordinate system (x,y,z), (b) simplified 2D (x,y) model setup for transient heat transfer simulation (c) FE discretization of the laminated hat structure	36
Figure 2.13: Cooling curves defined for Punch and Die obtained as average from 3 experimental trials. Punch has an initial cooling rate of -1.3 °C/s, Die has a cooling rate of -1.8 °C/s.....	37
Figure 2.14: Illustration of (a) a discretized laminate orientated at an angle (theta) w.r.t. global coordinate system (x,y,z). (b) k-th ply at a distance h_k from laminate midplane, and (c) stress free strains vs average laminate strain.....	39
Figure 2.15: FE model setup for mechanical tests showing thermoformed hat structure adhesively bonded with spine along with rigid impactor and supports.	44
Figure 2.16: FE model setup for impact test showing thermoformed hat structure with rigid impactor and fixed support. Each colored zone on hat represents LSDYNA part composite that embodies a unique set of stack up order of composite laminate	47
Figure 2.17: A schematic diagram of six static load cases representing (a) longitudinal compression, (b) longitudinal shear, (c) longitudinal bending, (d) transverse compression, (e) transverse shear and (f) transverse bending.....	49
Figure 2.18: FE model setup of the impact test showing composite hat structure with fixed edges impacted by a rigid plate (a) front view and (b) 2D cross sectional view.	50
Figure 2.19: Thickness variation in the hat structure: (a) Side 1, (b) Side 2 represented as (upper) measured average thickness \pm standard deviation and (lower) predicted thickness variation.	52

Figure 2.20: Fiber orientation in degree as observed in thermoforming trials and simulation at marked locations of the hat structure	53
Figure 2.21: Validation of Residual stresses code with model prediction data from Chapman et al. [62] (a) Comparison of transverse residual stresses σ_y evolution for surface and center plies, (b) comparison of transverse residual stresses σ_y distribution through the laminate thickness at $t = 60$ sec	55
Figure 2.22: (a) A discretized laminate considered from the hat structure, (b) evolution of residual stresses (σ_z) in surface plies S1, S2 and center ply through $t = 400$ s, (c) residual stresses ($\sigma_z, \sigma_x, \sigma_y, \sigma_{xy}$) against the location of ply (h) through thickness, where h ranges from -1 to 1.....	57
Figure 2.23: Contour plot showing residual stresses distribution along Z-axis on center and surface plies S1 and S2 of the laminated hat structure.....	58
Figure 2.24: (a) Force-displacement plot of three experimental trials (b) force-displacement plot for 3-point bend test comparing experimental response with numerical prediction.....	59
Figure 2.25: Deformation comparison between experimental trials and numerical simulations (a) deformation side view: close match with experimental trial 3 and (b) top view comparison with stress contour plot. Encircled are the damage initiation locations on structure.....	60
Figure 2.26: Dynamic impact test performance:(a) Force vs time plot showing three experimental trials and (b) front view of the experimental trials showing impactor position at initial contact, at maximum stroke and at loss of contact.	62
Figure 2.27: (a) Validation of dynamic impact test: Force vs time plot comparing experiment and simulation. (b) damage comparison of the experimental trials and numerical prediction.	62
Figure 2.28: Force vs displacement plot under impact loading comparing two cases of thickness variation with unmapped case.....	67
Figure 2.29: Progressive deformation of hat structure under impact loading showing the effect of thickness variation.	67
Figure 2.30: Fiber orientations for the three cases (a) unmapped, (b) D20 and (c) D35..	68
Figure 2.31: Force vs displacement plot comparing impact performance for the two fiber orientation cases.....	71

Figure 2.32: Unmapped vs D35: initial deformation of hat structure under impact loading and von-mises contour plot at time $t = 1$ ms.	72
Figure 2.33: Free body diagram showing the fiber tows direction and respective loading direction during (a) initial impact on top of the hat and (b) impact before compressive failure along the shorter edge of the hat.....	72
Figure 2.34: Unmapped vs D35: progressive deformation of hat structure under impact loading.....	73
Figure 2.35: Von Mises residual stresses contour plot for the two cooling rate cases.	74
Figure 2.36: Force vs displacement plot showing impact performance for various cooling rate cases.	77
Figure 2.37: Progressive deformation of hat structure under impact loading showing the effect of cooling rate.	77
Figure 3.1: (a) Solar sail supported with composite booms along diagonals, (b) Rolled coil of composite boom structure, and (c) different cross sections of booms [77].....	81
Figure 3.2: (a) Rigid female composite boom upper and lower tools used to form the Composite Boom structure, b) cured composite boom with male silicone plug inserted between the boom halves [77]	84
Figure 3.3: a) Pressure applied to the inside walls of the composite boom structure by the silicone plug, b) a typical cure profile for CFRP composites,	85
Figure 3.4: Composite Boom Self-heating Tool showing its materials and general construction.....	85
Figure 3.5: MTR pathway for thermoset based CFRP composite structures	87
Figure 3.6: Illustration of convection boundary condition in a heat transfer problem	89
Figure 3.7: Cross-section of Composite Boom tool showing the model setup. HS refers to Heat Spreader.....	91
Figure 3.8: Representative Graphite Flat plate with Heater bonded on one (Hot) side and thermocouples attached on the opposite (Cold) side	93
Figure 3.9: Arrangement of materials to make the Flat plate samples	94
Figure 3.10: 3D Model setup for Flat plate heat transfer analysis.....	96
Figure 3.11: Seven temperature measurement locations on cold side of plate mesh	97

Figure 3.12: Thermocouple measured cure profile on the heater surface. Total time = 20160 sec	99
Figure 3.13: Model setup for cure analysis.....	101
Figure 3.14: Thermal characteristics of CFOAM at specific locations on cold side of plate at t = 140 min	110
Figure 3.15: Thermal characteristics of CFOAM + 0.25mm SS400 at specific locations on cold side of plate at t = 236 min.....	111
Figure 3.16: Thermal characteristics of CFOAM + 0.25mm SS400 + BMI laminate 12 plys at specific locations on cold side of plate at t = 269 min	112
Figure 3.17: Thermal characteristics of graphite plate at specific locations on cold side of plate at t = 240 min	113
Figure 3.18: DOE: A study of design space	115
Figure 3.19: Model configurations for concepts C1 – C9	117
Figure 3.20: Point 1: Tool surface center, Point 2: Tool flat land center, temperature at Points 1 and 2 are used for calculating Temperature uniformity. Dotted line passing through point 1 is the line of symmetry of the tool.....	119
Figure 3.21: Temperature uniformity and drop in Concept C6 at steady state.....	121
Figure 3.22: Temperature uniformity and drop in Concept C9 at steady state.....	121
Figure 3.23: Temperature evolution contours in C1 concept at t = 1min, 10 min, 100 min and 400 min.....	123
Figure 3.24: Temperature contour plots for (a) C1 and (b) C10.....	124
Figure 3.25: Temperature evolution contours of concepts C2,C3 and C4 at t=1 min, 10 min, 50 min and 100 min	125
Figure 3.26: Temperature evolution contour of concept C5 at t=1 min, 10 min, 100 min and 300 min.....	126
Figure 3.27: Laminate locations used for plotting cure profiles and degree of cure	129
Figure 3.28: (a) Cure profiles, (b) Degree of cure curves at Laminate center and Laminate top flat locations.....	130
Figure 3.29: Resin volume fraction obtained at the end of Flow-compaction analysis..	131

Figure 3.30: Process-induced deformation observed at the end of the stress-deformation analysis. Deformation scale factor: 5..... 132

Figure 3.31: (a) Cure profiles, (b) Degree of cure curves at laminate center and laminate top flat locations for thin-ply laminate..... 133

Figure 3.32: Process-induced deformation observed at the end of Stress-deformation analysis for thin-ply laminate..... 134

CHAPTER 1 : INTRODUCTION

1.1 Introduction to Composites

Composite materials typically consist of two or more constituents combined together in an effort to achieve properties better than that of the individual constituents. There are two phases in a composite material, one is the reinforcement phase while the other is a continuous phase also known as the matrix phase. The earliest example of a composite material is a brick made of clay and straw. Wood and bones are some of the composite materials found in nature. The reinforcement in a composite could be in the form of flakes, particles, or fibers. The matrix phase could be categorized as metallic, ceramic or polymer based [1].

1.2 Fiber reinforced Polymer Composites

Fiber reinforced Polymer composites (FRPs) have polymer as the matrix phase and fibers as the reinforcement phase. The polymer could be either thermosetting or thermoplastic. Thermosetting polymers demonstrate a unique behavior termed curing. During curing process, the polymer chains undergo a chemical process termed crosslinking making the polymer stronger and harder. Upon further increase in temperature the thermosetting polymers undergo degradation and hence cannot be reshaped. In contrast, thermoplastic polymers do not undergo crosslinking. They soften on heating and can be reshaped [2].

FRPs generally have high specific modulus, high specific strength, and low density as compared to metals. Their properties depend on the size and alignment of the fibers in the polymer matrix. Some of the commercially used reinforcements include glass, carbon

and aramid fibers. Accordingly, application specific or tailored properties can be achieved by customizing the size, alignment and type of fiber used for a particular FRP. It can be inferred that it is advantageous to use FRPs for applications demanding high strength and stiffness to weight ratios [3]–[6].

1.3 Continuous and Discontinuous Fiber reinforced polymer composites

Continuous Fiber Reinforced polymer composites (CoFRPs) have fibers running along the entire length of the sheet. Discontinuous Fiber reinforced polymers (DicoFRPs) on the other hand are short and dispersed in the matrix. These may be aligned along a particular direction or randomly oriented. The abovementioned types of FRPs are shown in Figure 1.1. Multiple unidirectional laminae can be stacked up in different orientations (e.g. 0° , 45° , 90° , etc.) to form a laminate shown in Figure 1.1(b). The CoFRPs have better direction specific properties such as specific strength and stiffness as compared to DicoFRPs. Consequently, DicoFRPs have found several applications as aesthetic and secondary structures [7]–[9]. Whereas, CoFRPs are primarily used as primary/load bearing structures in aerospace industry and are gaining enormous popularity in the automotive and other industries [10]–[15].

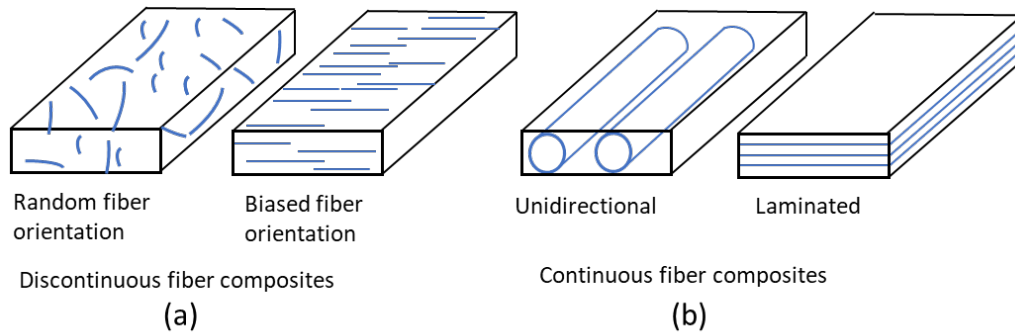


Figure 1.1: (a) Random and aligned/biased orientation of discontinuous fiber reinforced polymer composites (DicoFRPs), (b) Unidirectional and laminated continuous fiber reinforced polymer composites (CoFRPs)

1.4 Continuous Carbon Fiber Reinforced Polymer composites (continuous CFRPs)

Continuous Carbon Fiber reinforced polymer composites consist of carbon fibers as the continuous reinforcement in either thermoset or thermoplastic polymer matrix. Continuous CFRPs have very high specific stiffness to weight ratio. However, these have significant costs associated with their processing. Continuous CFRPs are commercially available as laminates/tapes in unidirectional or woven configurations (Figure 1.2). These laminates may have more than one lamina (single ply) stacked together and consolidated under pressure [16]. These laminates are called composite prepregs. Continuous CFRPs have substantial light weighting potential and properties can be tailored to suit a particular application [14], [17], [18].

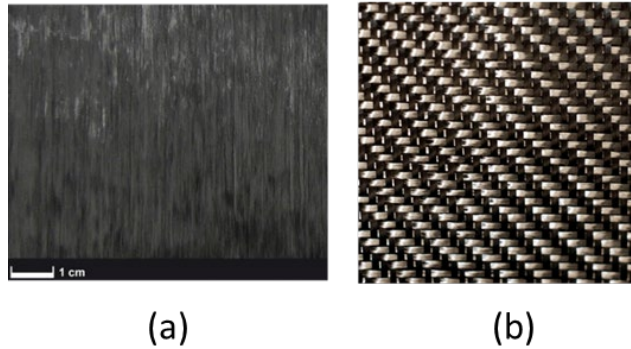


Figure 1.2: (a) Unidirectional carbon fiber prepreg, (b) Woven (2*2 Twill) carbon fiber prepreg

1.5 Manufacturing Processes of continuous CFRPs

A number of manufacturing processes have been developed for the processing of continuous CFRPs. Some of these processes include autoclave/ vacuum bag molding [19], out-of-autoclave molding using self-heated tools [20], thermoforming [21], automated tape laying [22]. In the present study, we focus on two manufacturing processes: a thermoforming process for thermoplastic continuous CFRP prepregs and an out-of-autoclave molding process for thermoset continuous CFRP prepregs.

1.5.1 Thermoforming

Figure 1.3 shows the steps involved in the thermoforming of a composite part [21]. First, the thermoplastic composite prepreg is heated above the melting point of the polymer. Second, the heated prepreg is transported to the forming tool generally through a conveyor system. Some temperature loss is expected during the transport as shown in the temperature-time plot. Third, the prepreg is formed using matched-die tool. In this step, there is temperature drop due to conduction between the prepreg and the tool and

convection losses to the surroundings. Next is the consolidation step where the formed part is allowed to cool in the closed tool. Finally, the part is released.

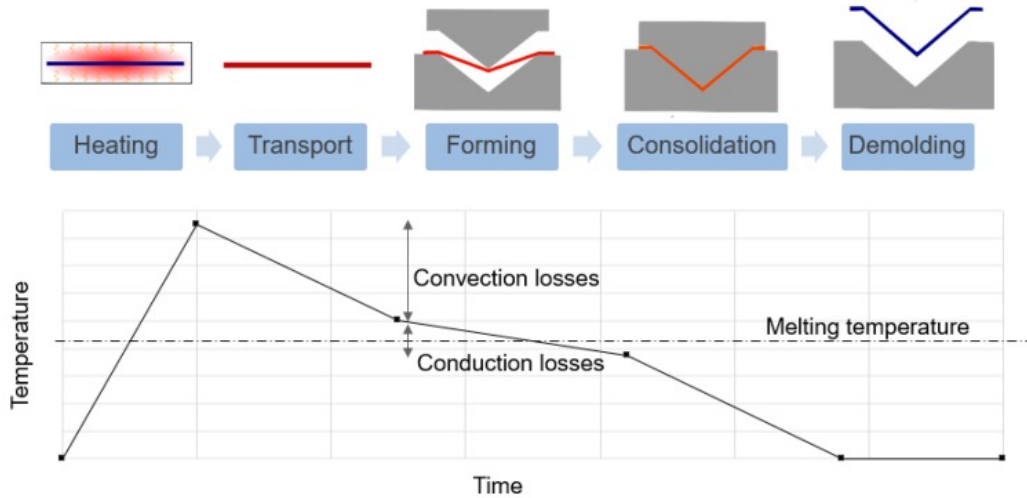


Figure 1.3: Thermoforming process steps of thermoplastic FRPs [21]

1.5.2 Out-of-autoclave molding using self-heated tool

Out-of-autoclave molding (OOA) using self-heated tool is a modification of the traditional autoclave and oven molding processes. A comparison of the three processes provides a better understanding of their similarities and differences. Figure 1.4 shows a comparison of the autoclave, oven and self-heated tool molding [23]. In the autoclave molding process, the composite part is confined in a pressure vessel with internal heat and pressure generation. The entire pressure vessel is applied vacuum pressure and the composite prepreg is cured through air/environment heating. In the oven, the composite part cures similarly through air heating. However, vacuum pressure is applied only to the composite prepreg through vacuum bagging. In contrast to that, the self-heated tool consists of heating elements embedded inside the tool. Pressure is applied to the composite prepreps through vacuum bagging. As a result, the tool is heated first and brought to the

desired curing temperature. Subsequently, the composite part cures on the heated tool surface. Since this process does not require the use of a confined space like the autoclave and the oven, this technology is called out-of-autoclave (OOA) molding. This technology is especially suitable for large composite structures.

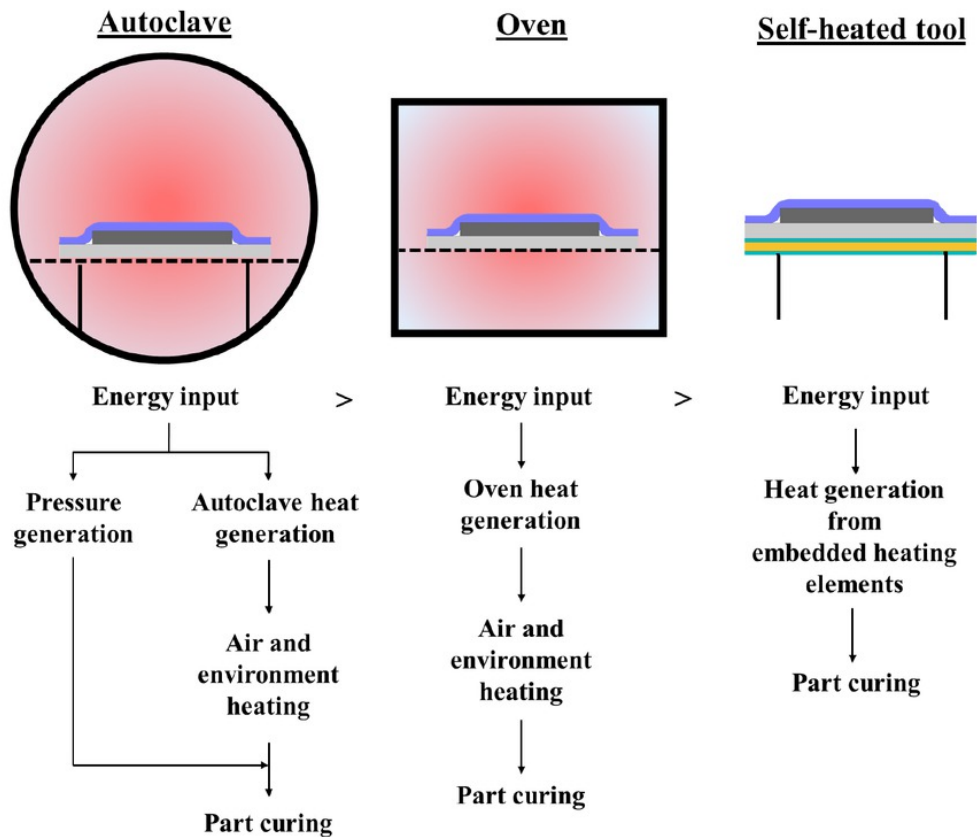


Figure 1.4: A comparison between autoclave, oven and self-heated tool molding processes [23]

1.6 Development of composite structures for load-bearing applications

Figure 1.5 shows the conventional procedure for development of structures for load-bearing composite structures. First step in the procedure is target definition (e.g. weight-reduction, cost-saving, etc). This is followed by concept development and design

process. Next, prototypes are manufactured and tested. If the targets are met in the prototype phase, the structure moves into the production phase otherwise the procedure is repeated. This traditional approach is both tedious and time-consuming. The development process of metal structures is quite streamlined due to years of experience. However, development of composite structures still present considerable challenges in terms of design and manufacturing. For example, alignment of CFRPs in specific directions to meet structural targets and drapability check of the material to form into the desired shape require numerous iterations. Further, CFRPs need to be processed at elevated temperatures. For that purpose, an optimum manufacturing window needs to be identified which again requires several trials. Consequently, the conventional development approach proves to be inefficient. An effectual way forward necessitates integration of computational modeling with the traditional development method.

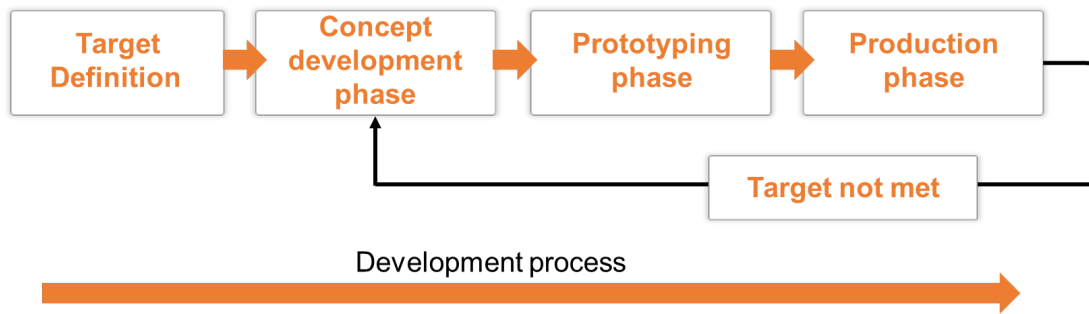


Figure 1.5: Conventional development process of structures/components for load-bearing composite structures

1.7 Literature review on development of composite structures

As the development of continuous carbon fiber reinforced (CFRP) composite structures or structural components can be accelerated by using computational engineering approaches, design optimization [18], [24] or manufacturing optimization [25], [26] studies

have been conducted on CFRP composites. It was shown that optimal strength and impact performance or optimum processing window for parameters such as stamping pressure, velocity, temperature, and degree of crystallinity can be achieved. Nevertheless, while these analyses and optimizations are useful for their specific purposes, they are largely isolated and disconnected from each other. Such compartmentalized approaches have a fundamental drawback in the design and optimization of CFRP structures. This is due to the fact that the material properties and mechanical behavior of CFRP is intrinsically coupled with the manufacturing process, leading to inhomogeneous fiber orientations, thickness variations, and residual stresses in the formed CFRP structures. Figure 1.6 shows fiber orientation variations in a hemispherical dome [27], thickness variations in a hat structure [28] and residual stress induced warpage in an L-shaped structure [29].

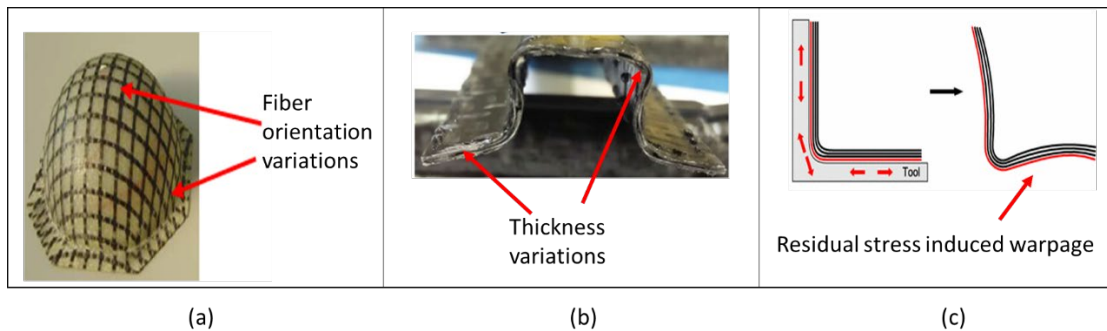


Figure 1.6: (a) Fiber orientation variations in a hemispherical dome [27], (b) thickness variations in a hat structure [28], and (c) residual stress induced warpage in an L-shaped structure [29].

These process induced effects can have significant influence on CFRP composite structures' mechanical response [27], [30]–[33]. For example, fiber reorientations and the resulting changes in material properties have shown a considerable impact on static structural performance [27], [30], [31]. In another study, cooling rate which directly

influences the magnitude of residual stresses generated in the formed part was shown to have effect on the mechanical performance [32]. In yet other study, cure process induced residual stresses were shown to have significant effect on the tensile stiffness of the matrix material [33]. Therefore, in order to develop high performance, high quality CFRP composite structural components, an integrated design and manufacturing optimization approach is required.

1.8 Virtual process chains for development of CFRP structures

Such an integrated approach can be achieved by first establishing a relationship between the manufacturing process and mechanical response of the structure, and successively, optimizing the manufacturing process parameters to achieve the desired targets. This requires the development of a pathway (or CAE chain) comprising of computational models for all the process steps which are validated with experiments at coupon and structural level. To this end, a few attempts have been made to connect the design, manufacturing and structural simulation steps in series, by developing virtual process chains (CAE chains) and mapping methods [31], [34], [35]. However, the recent publications implementing these methods are missing some of the relevant effects or steps of the manufacturing process. For example, Kärger et al. [35] developed a comprehensive CAE chain shown in Figure 1.7 for the RTM process of thermoset based composites which involves draping, molding, curing and structural analysis steps. However, the curing simulation was not included in their current study which is a vital part of modeling the physics of the RTM process. It is important to note that a complete CAE chain would

involve curing simulation in case of thermoset processing and cooling simulation in case of thermoplastic processing.

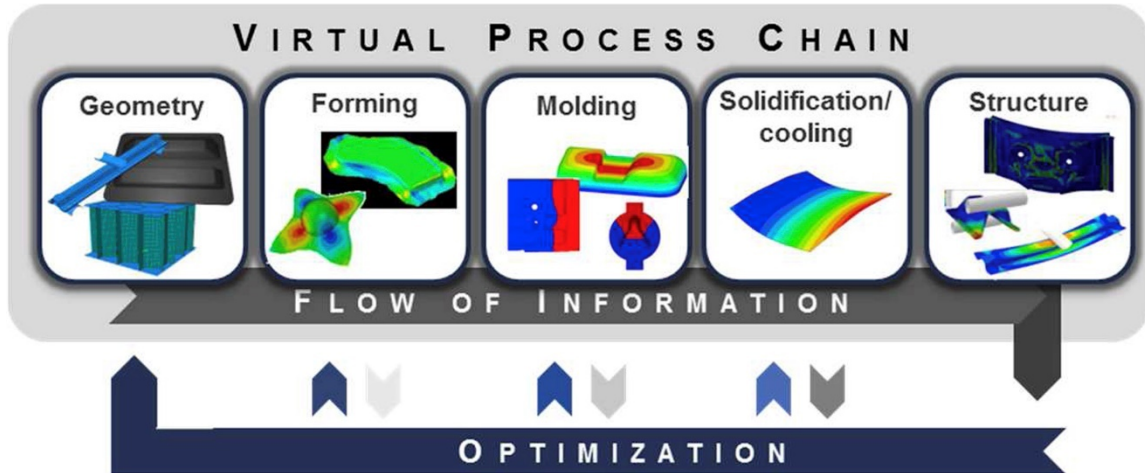


Figure 1.7: Virtual process chain developed for Resin transfer molding (RTM) process [35].

In a separate study, Hsiao et al. [36] developed a FE model to determine the effect of both forming and cooling process on CFRTP. While the process induced effects such as thickness distribution, fiber orientation and residual stress development are presented for various part shapes, they did not investigate the effects of these results on the structural response. A notable contribution has been made by Jayasree et al. [28] employing extensive simulation and experimental methods to study a hybrid (forming + injection molding) molding process. Their model involves FE analysis, experimentation, and validation at each level i.e. coupon level, structural level and system level based on the “Building block approach”. Figure 1.8 shows the “Building block approach” developed by NASA [37] which was implemented in their study. At structural level, process induced effects are included to determine the structural response. However, in their work, cooling

induced residual stresses are not incorporated which can significantly affect the response of the thermoformed structure under static and dynamic loading.

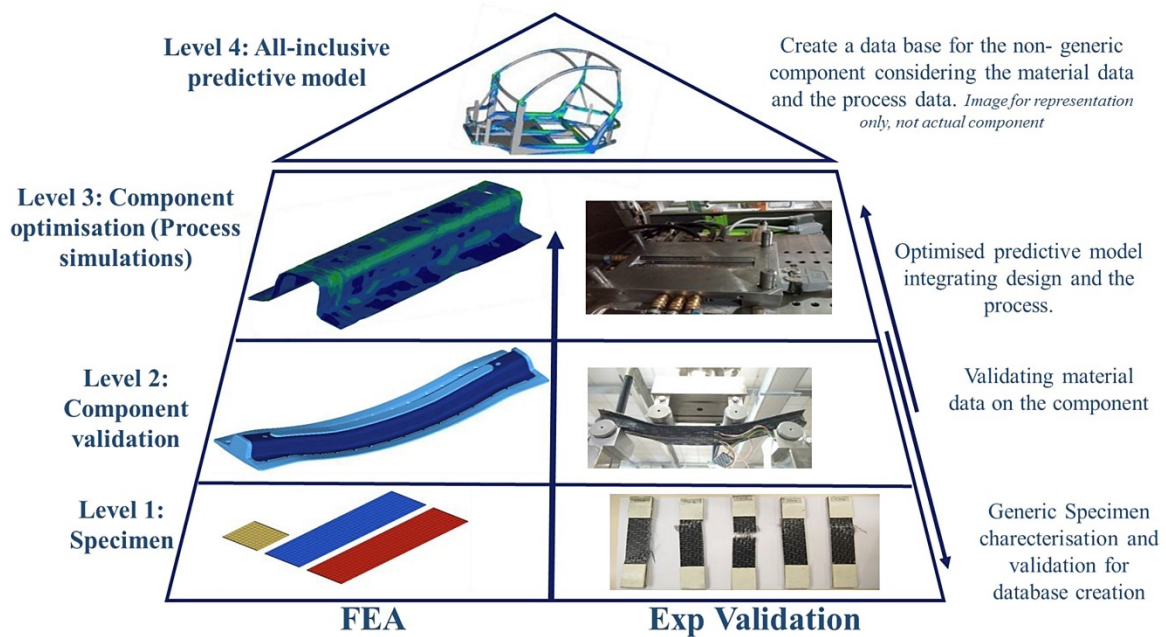


Figure 1.8: “Building-block approach” implemented for development of thermoplastic CFRP component [28].

From literature, it is realized that specifically for the thermoforming process of thermoplastic CFRPs and OOA molding process using self-heated tool of thermoset CFRPs, a pathway that considers all the relevant process steps is not yet developed. The present work establishes complete manufacturing-to-response (MTR) pathways for end-to-end analysis of continuous CFRP structures manufactured through the two abovementioned routes. As case studies, the MTR pathway was implemented for 1. thermoplastic based CFRP composite Hat structure manufactured by thermoforming process and 2. thermoset based CFRP composite Boom structure manufactured by the

OOA molding process using self-heated tool. This pathway broadly comprises of numerical simulation of manufacturing process of CFRP composites and their experimental validation from coupon to structural level. The MTR pathway contributes towards building confidence in process simulations which will reduce product development time of CFRP based structures and lead to their widespread adoption in the future.

1.9 Thesis Organization

The thesis document is organized as follows. Chapter 2 first provides an introduction and motivation for the implementation of the MTR pathway for a composite hat structure manufactured by thermoforming process. Second, framework of the MTR pathway is described in detail. Next, each step of the pathway including the experimental and numerical methods are explained. After that, validation results as well as numerical study results are discussed. Finally, conclusions for Chapter 2 are provided. Likewise, Chapter 3 begins with introduction and motivation for implementation of MTR pathway for a composite boom structure processed by OOA molding process using self-heated tool. Next, a detailed description is provided for the steps performed in the scope of the present study. Thenceforth, validation and other results including optimization and curing simulation results are presented and discussed. In the last section, conclusions and future work for Chapter 3 are provided. Finally, Chapter 4 offers conclusions of the two case studies considered for the current research effort.

CHAPTER 2 : MTR PATHWAY FOR THERMOFORMED THERMOPLASTIC COMPOSITE HAT STRUCTURE

2.1 Introduction and motivation

The key motivation for development of composite structures for automotive applications is weight reduction which leads to increased fuel efficiency. In the past, approaches such as topology optimization [38] or lighter material substitution [39] have been used to achieve weight reduction primarily for the body-in-white of the vehicle. The door systems also contribute to about 35-50% of the vehicle weight. However, light-weighting of door systems still present a considerable challenge due to their stringent crashworthiness requirements. This requires ability of the structural components of the door systems to absorb impact energy and prevent occupant injuries [40]. The US department of energy (DOE) put forth a challenging task of light-weighting the driver side front door by 42.5%, allowing a maximum cost-increase of \$5 for every lb. of weight saved. Static and dynamic load cases were defined which were required to be satisfied by the developed light-weight door. The baseline door of an OEM's standard mid-sized SUV shown in Figure 2.1 was selected for this purpose.



Figure 2.1: Driver side front door of an OEM’s mid-size luxury crossover selected for light-weighting

Accordingly, the structural parts of the baseline door were consolidated to design two primary load-bearing thermoplastic based CFRP components along with some carryover sheet metal parts from the baseline design. The structural components of the light-weight door are shown in Figure 2.2. The two thermoplastic CFRP components are namely the inner frame and the beltline stiffener.

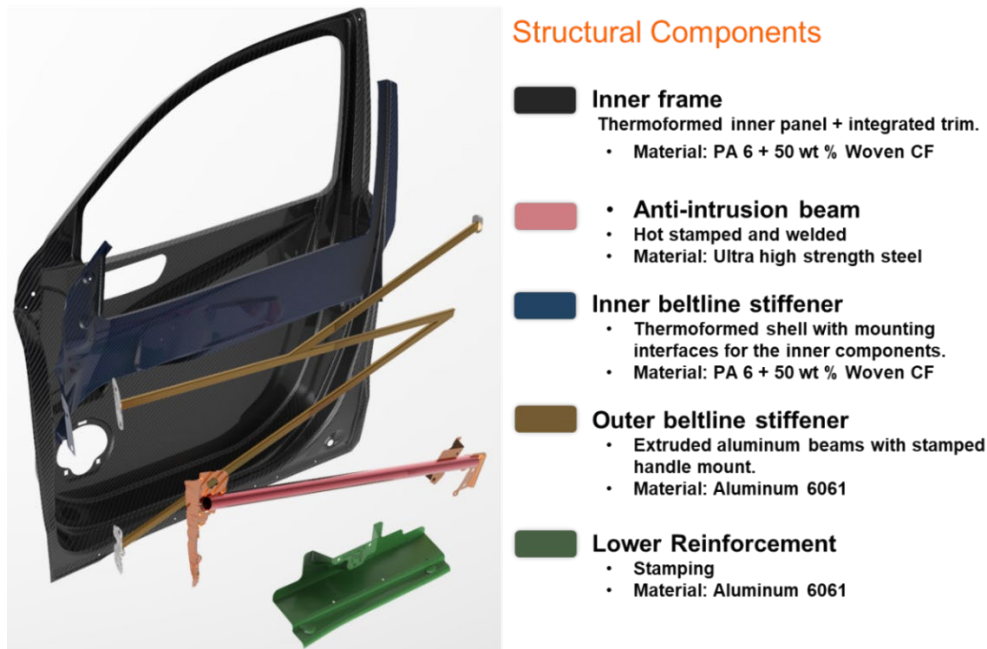


Figure 2.2: Structural components of the ultralightweight door

Both these components are to be manufactured by the matched-die thermoforming process described in section 1.5.1. The thermoforming process when applied to thermoplastic based CFRPs inevitably introduces some undesirable effects such as fiber orientation variations, thickness variations and residual stresses. It was realized that the thermoforming process would have impact on the structural performance of the door. As a result, it was deemed necessary to study the thermoforming process effects on the structural performance of the door. However, the door structural components are very large to conduct such a comprehensive study. Therefore, a hat section from the sash region of the inner frame was selected to perform a sub-component level investigation. The hat section location on the inner frame of the door is shown in Figure 2.3. Accordingly, the MTR pathway was implemented for the thermoplastic based composite hat structure to study the thermoforming process effects on the structural performance.

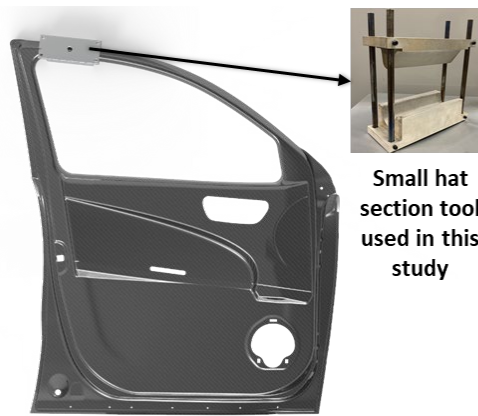


Figure 2.3: Location of the hat section on the inner frame of the light-weight door used to implement the MTR pathway

2.2 Manufacturing-to-response pathway

Figure 2.4 shows the general framework of the MTR pathway which consists primarily of five process steps as follows: 1) material characterization at coupon level and material card (MAT card) generation for thermoforming simulation and mechanical analysis, 2) thermoforming simulation and experimental validation at structural level, 3) experimental and numerical cooling analysis followed by residual (skin/core) stresses analysis, 4) mapping of process induced effects and 5) mechanical performance evaluation and experimental validation at structural level. The detailed steps of the MTR pathway are described here.

In the first step, material properties at the coupon level are experimentally characterized. These properties are used to generate material cards for performing numerical simulations such as thermoforming and cooling simulation, residual stresses

analysis and mechanical analysis. Typically, thermoforming process is carried out at a temperature above the melting point of the resin. Thus, material testing at coupon level is conducted above the melt temperature of PA6 ($>220^{\circ}\text{C}$) to determine tensile and shear mechanical properties. The thermal characteristics of the material such as thermal conductivity and coefficient of thermal expansion are determined for cooling analysis and residual stresses calculation. Finally, room temperature tensile and compression tests are carried out to obtain the mechanical properties to perform static and dynamic mechanical analysis.

The second step of the pathway comprises of thermoforming experiments and simulations. The thermoforming experiments are conducted at near isothermal conditions. Thermoforming simulations are performed using the material card developed in Step 1. The changes in fiber orientations and thickness variations obtained from the simulations are validated with the experimental results in this step. The third step consists of quench cooling experiment, FE cooling analysis and calculation of cooling induced residual stresses. In this step, the thermoformed structure is first quench cooled to room temperature by using forced flow cooling and the temperature evolution of tools during cooling is recorded. These cooling curves are used as an input boundary condition to carry out the transient cooling FE analysis. The spatial temperature distribution and evolution are obtained for the thermoformed composite structure from the FE cooling analysis, which is then used as an input, to compute the cooling induced residual stresses.

In the fourth step, the predicted residual stresses, thickness variations and fiber reorientations are incorporated into the static and dynamic FE setup, by using a mapping

procedure. The last step of the MTR pathway involves numerical evaluation of the mechanical response under the static and dynamic loading conditions which is validated by the experimental tests. In this study, a quasi-static three-point bend test is considered to validate the process induced effects on the mechanical response by comparing the deformation, stresses, and failure characteristics.

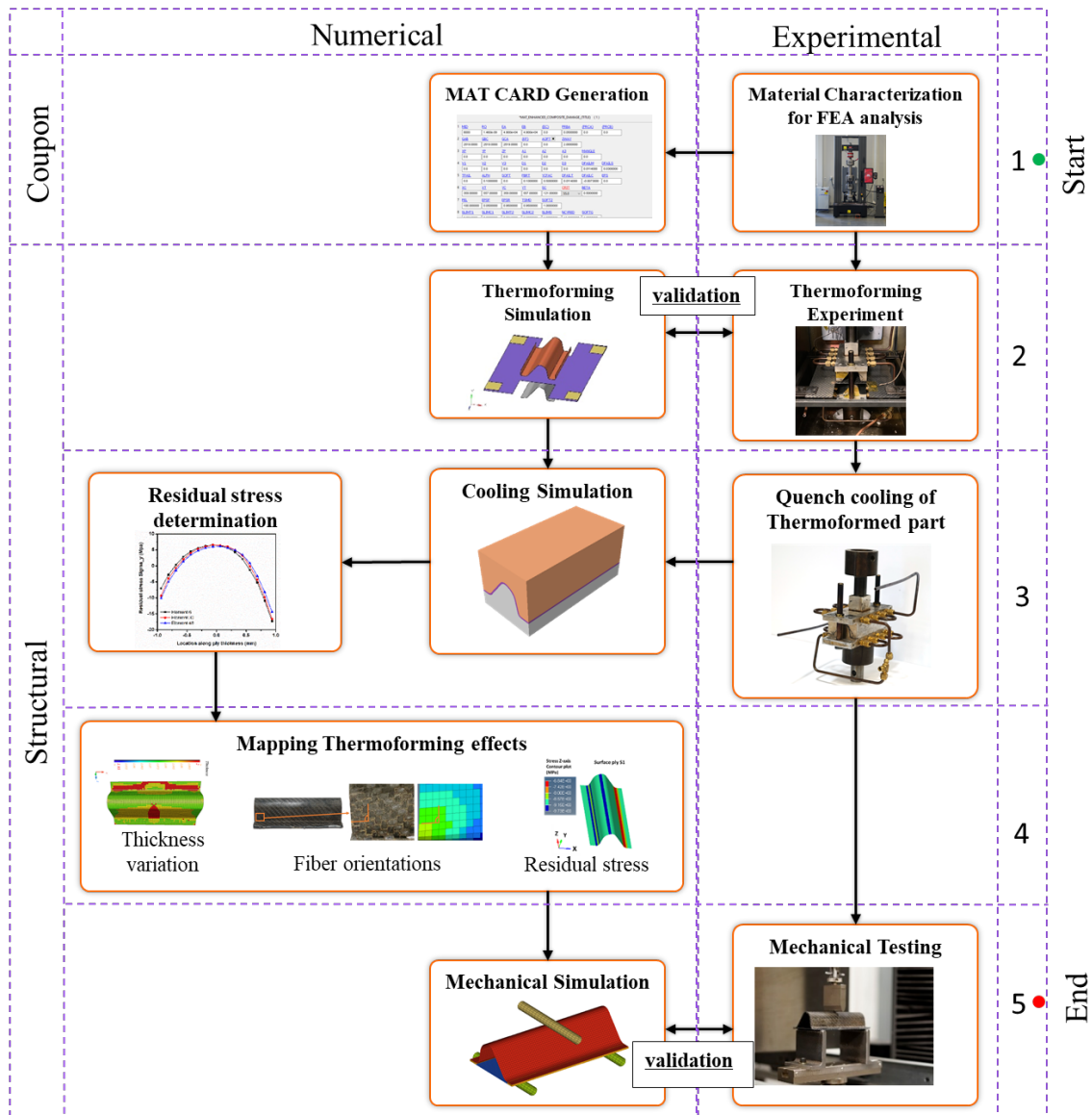


Figure 2.4: Manufacturing-to-response (MTR) pathway.

2.3 Experimental setup for material characterization and model validation

The material considered for the present work is a 1.97 mm thick consolidated sheet, comprising of 2/2 twill carbon fabric polyamide 6 (PA6) composite, supplied by Bond Laminates, a subsidiary of Lanxess. The fiber content by volume is 50 wt. %. Considering the balanced weave of the material, in-plane properties are assumed to be equivalent in the warp and weft directions.

2.3.1 Material characterization for thermoforming analysis

High temperature ($>220^{\circ}\text{C}$) tests are conducted in 0/90 and +45/-45 orientations for which samples are waterjet from the pre-consolidated sheets received from the supplier. Test samples in 0/90 orientation measure 180 mm in length, 25 mm in width and 1.97 mm in thickness, while samples in +45/-45 orientation measure 250 mm in length, 25 mm in width and 1.97 mm in thickness. The furnace is allowed to equilibrate at 264°C , samples are placed in with a thermocouple and tests are carried out once the sample reaches 264°C . As per ASTM D 3039, a crosshead speed of 5 mm/min is used on at least 5 samples.

The method used for tensile testing of the +45/-45 orientation samples at high temperature is termed as bias-extension test. A normal force vs displacement plot is obtained from the bias-extension test (see Appendix A), which is converted to shear stress vs shear angle plot. The process is illustrated herein. Consider the specimen under a bias-extension test, with three zones of deformation as shown in Figure 2.5. The zone A largely remains undeformed during the test while the zone B undergoes both tensile and shear deformation. The zone C undergoes pure shear deformation which is used for determination of shear characteristics of the composite material. The angle $\theta_o = 45^{\circ}$ is the

initial configuration of zone C while θ defines the deformed angle. The shear angle γ in zone C can be expressed as [41]:

$$\gamma = 90^\circ - 2\theta = 90^\circ - 2 \cos^{-1} \left(\frac{L_{eff}}{\sqrt{2}L_0} \right) = 90^\circ - 2 \cos^{-1} \left(\frac{L_0 + \delta}{\sqrt{2}L_0} \right) \quad (2.1)$$

where $L_0 = H - W$, H is the initial height and W is the initial width of the specimen, δ is the displacement recorded during test. The normal force obtained from the bias-extension test is converted to normalized shear force by applying a normalization technique proposed by Harrison et al. [42] for rate-dependent materials. The normalized shear force as a function of shear angle is given as [41]:

$$F_{sh}(\gamma) = \frac{\left(\frac{H}{W} - 1 \right)}{\left(2 \frac{H}{W} - 3 + 2X \right)} \frac{F}{\frac{\sqrt{2}W}{2}} \quad (2.2)$$

where $X = \frac{1}{4} \left\{ \frac{\cos^2(\gamma)(1+3\sin^2(\gamma/2))}{\cos^2(\gamma/2)(1+3\sin^2(\gamma))} \right\}$. The shear force calculated using Equation (2.2)

is divided by the thickness (1.97mm) of the specimen to give the shear stress. The high temperature (HT) shear modulus given in Table 2.1 is thus calculated from the shear stress-shear angle plot.

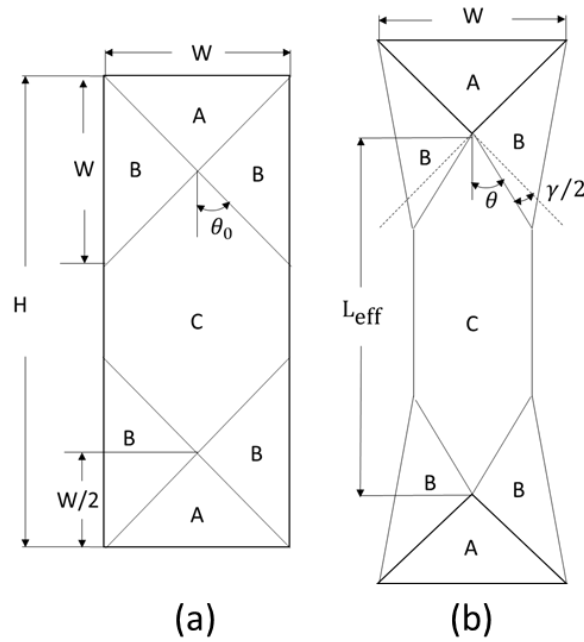


Figure 2.5: Composite specimen under the bias-extension test (a) undeformed and (b) deformed configurations (after Lebrun et al. [43]).

2.3.2 Material characterization for cooling analysis and residual stresses

calculation

The thermal properties including thermal conductivity, specific heat capacity and coefficient of thermal expansion (CTE), are experimentally determined for the carbon/PA6 composite material under investigation. Thermal conductivity of composite samples is measured as per ASTM D 7984 using a Therm TCi TH91-13-00703 instrument. Three tests are performed on the samples having dimensions 8 mm (length) \times 8 mm (width) \times 1.97 mm (thickness). Specific heat capacity is determined in accordance with ASTM, E 1269 on three circular composite samples (6 mm diameter and 1.97 mm thickness). The tests are performed on a DSC Q 20 (TA instruments). Sapphire standard, empty pans and composite samples are tested from 20 °C to 60 °C at a ramp rate

of 10 °C/min under nitrogen atmosphere and an average result of three samples are reported in Table 2.1. CTE is determined by conducting the probe expansion measurement on a TMA Q 400 (TA instruments). Measurements are performed on samples having a size of 8 mm (length) × 8 mm (width) × 1.97 mm (thickness). Three samples are tested from -30 °C to 60 °C at a ramp rate of 10 °C/min under nitrogen atmosphere. An average CTE value in both the warp and weft directions is determined to be 6.85e-6 /°C. The thermal properties experimentally obtained are listed in Table 2.1. It is important to note that viscoelastic effects are dominant above glass transition temperature of PA6 (T_g = 60°C). These effects are not considered in the present work. As a result, the thermal properties such as specific heat and CTE are measured up to 60 °C.

Table 2.1: Material properties for cooling analysis

Property		Carbon/PA6	6061-T6 Aluminum [44]
Density [<i>kg/m³</i>]		1430	2700
Specific Heat [<i>J/kg K</i>]	@ 25°C	1206.65 ± 24.57	896
	@ 45°C	1304.96 ± 21.36	
	@ 60°C	1364.76 ± 18.64	
Thermal conductivity [<i>W/m K</i>] @ 25°C		0.682 ± 0.001	167

2.3.3 Material characterization for mechanical analysis

Material characterization is conducted in tension, compression and shear using appropriate standards. Tensile tests for the 0/90 are performed in accordance with ASTM D 3039. Compression tests are carried out for the 0/90 and +45/-45 samples in accordance with ASTM D 6641. Samples with the following dimensions: 140 mm (length), 13 mm (width) and 1.97 mm (thickness) for 0/90 and 150 mm (length), 25 mm (width) and 1.97mm (thickness) for +45/-45 orientation are waterjet. A uniaxial strain gauge is bonded on each side of the sample in order to measure the strain on both sides to ensure there is no buckling. All compression tests are performed on a combined loading compression (CLC) fixture on an Instron 5985 universal testing machine with a 250 kN 2580 series static load cell using a crosshead speed on 1 mm/min. The material properties obtained from the tests are listed in Table 2.2.

Table 2.2: Average mechanical properties for investigated woven Carbon/PA6 composite

Property	Young's Modulus (GPa)		Shear Modulus (GPa)	Stress at Failure (MPa)	Strain at Failure (%)	
	RT (25°C)	HT (264°C)				
Tension 0/90°	55.1 ± 2.05	20.15 ± 1.72	NA	532.3 ± 36.31	0.836 ± 0.06	
	50.08 ± 13.23		NA	303.0 ± 16.04	0.631 ± 0.01	
Compression 0/90°	NA		RT (25°C) 1.783 ± 0.09	HT (264°C) 4.39e-6 ± 1.01e-6	131.48 ± 6.68	45.47 ± 2.85
Compression 45°	NA		1.4 ± 0.18		70.4 ± 2.04	31.93 ± 1.22

2.3.4 Experimental tests for model validation

The MTR pathway presented in this study is validated by first fabricating a composite hat structure using the thermoforming process and then by performing

mechanical tests. The experimental measurements are then compared with the numerical results. The experimental tests are discussed here.

2.3.4.1 Hat section fabrication (thermoforming setup)

The thermoforming setup consists of two forming tools (punch and die) and the blank holder apparatus accommodated in a thermal chamber shown in Figure 2.6(a). A rigid steel frame is constructed to hold the composite sheet (blank) with the help of binder tabs of size 70 mm × 38 mm at four locations. The sheet is held in place with an initial blank holder force of 70 N. All forming tests are carried out on Instron 5985 universal testing machine with a 250 kN 2580 series static load cell. Tests are carried out using a crosshead speed of 5 kN/min speed till the pre-set load of 22 kN is reached. The entire setup including the frame, blank and forming tools is placed in the furnace. Thermocouples are placed on the punch, die, blank and the furnace is heated to 264 °C. The thermocouple readings for the tools and the blank recorded using an e-DAQ during heating phase are shown in Figure 2.7. The blank is thermoformed to a hat structure at close to isothermal conditions within the narrow forming window (Figure 2.7).

After the thermoforming process, the entire set up is then cooled via forced convection till the hat structure reaches 100 °C. Subsequently, liquid nitrogen is injected through copper cooling channels in the tool in order to quench cool the formed structure to room temperature. The thermocouple readings for punch, die and hat structure during cooling phase are shown in Figure 2.7. The intent of quench cooling is to demonstrate the effect of cooling rate of the tools on the formation of residual stresses in the structure. Since

the thermocouple measuring hat structure temperature is not placed between the punch and die, its cooling data does not provide accurate temperature evolution in the formed hat structure. As a result, the hat structure cooling data cannot be used directly for residual stress determination.

Nevertheless, the thermocouple measurement serves as a useful reference to initiate and stop the thermoforming process when the desired temperature values are reached. The cooling channels (see Figure 2.6(b)) are constructed in such a way that the hat structure does not come in contact with the liquid nitrogen, any cooling seen on the material is due to conduction from the punch and die tools. The fabricated hat structure has a width of 75 mm and length of 145 mm, the hat cross section view and side view is shown in Figure 2.6(b). To the best of the authors' knowledge this work is the first that uses in-mold liquid nitrogen for controlled quench cooling of composite part after forming.

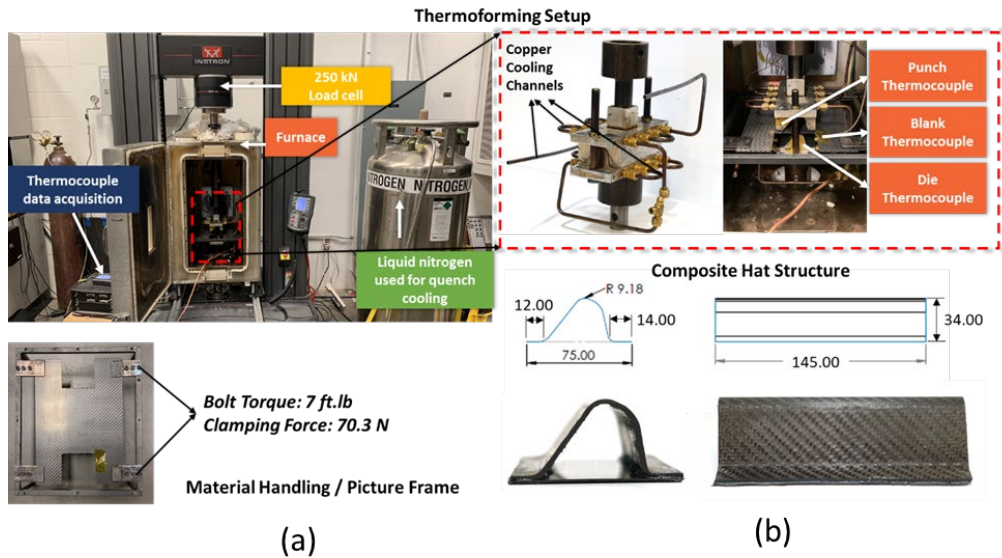


Figure 2.6: (a) Thermal chamber equipped with thermocouple data acquisition system and liquid nitrogen cooling for thermoforming tests, material handling system with binder tabs holding the blank. (b) thermoforming setup showing copper cooling channels, thermocouple locations and thermoformed hat structure in cross section view and side view.

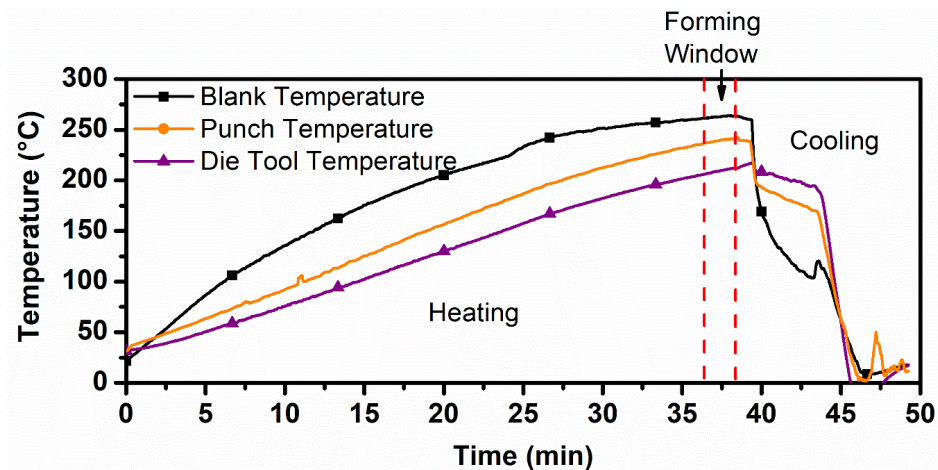


Figure 2.7: Thermocouple data for punch, die and blank during thermoforming process showing heating, forming and cooling phases

2.3.4.2 Three-point bend test

The hat structure samples are adhesively bonded to a 0.5 mm thick woven carbon/PA 6 composite sheet using the Plexus MA 530 adhesive material as shown in Figure 2.8(a). The experimental setup for the quasi-static three-point bending test with the bonded hat structure is shown in Figure 2.8(b) which consists of two supports with the span of 119.3 mm and a punch. The tests are carried out on Instron 5985 universal testing machine with a 10 kN 2580 series static load cell using a modified 2810 series flexure fixture from Instron. The three-point bend tests are conducted on three samples with the crosshead speed of 1 mm/min.

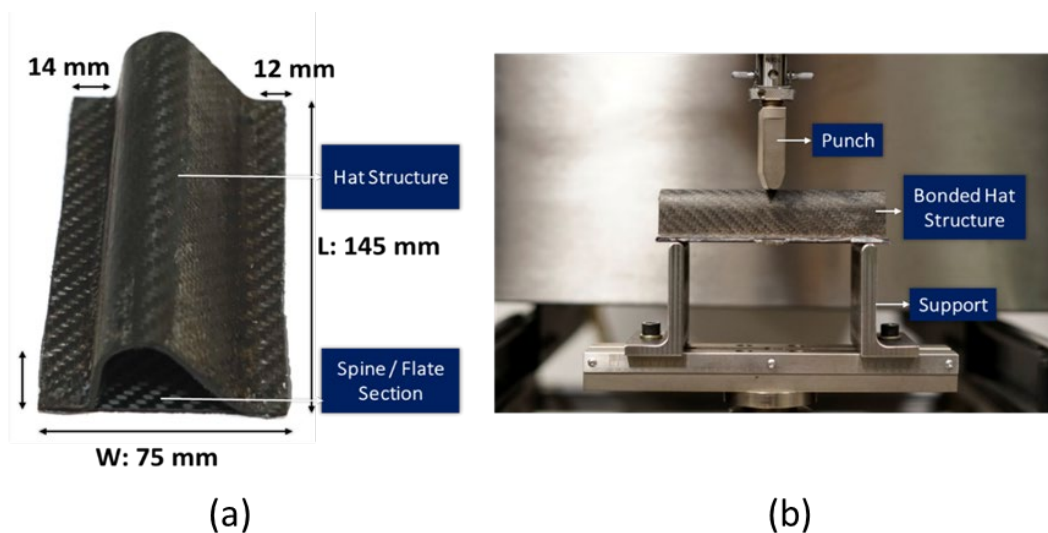


Figure 2.8: (a) Dimensions of bonded hat structure (b) Experimental setup for 3-point bend test showing the bonded hat structure, supports and punch.

2.3.4.3 Dynamic Tests

The formed hat structures are secured in an aluminum enclosure as shown in Figure 2.9 using aluminum constraints. The experimental setup for these dynamic tests consists of two constraints that are 20 mm long and a 1-inch diameter punch having an overall weight of 3.1 kg. The tests were carried out on a Lansmont Corporation cushion testing machine equipped with a 2000 g PCB accelerometer TP3 data analysis software, Olympus i-Speed 3 high speed camera. The dynamic tests are conducted on three samples with an average drop speed 4.3 m/s.

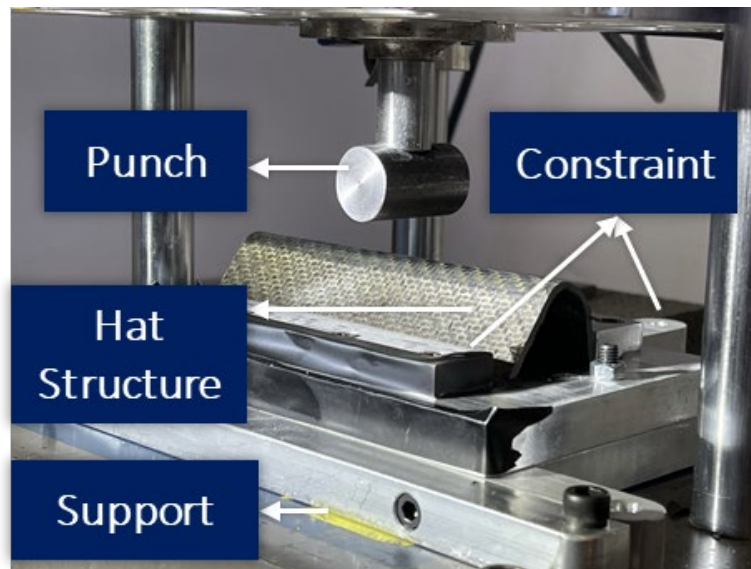


Figure 2.9: Experimental setup for dynamic tests showing the constrained hat structure, support, constraints and punch.

2.4 Modeling pathway

The FE model for thermoforming process is developed to reproduce the experimental setup. The thermoforming simulation process is broken down into two steps.

In the first step, thermoforming simulations are performed using material properties for the blank at forming temperature (264 °C). In the second step, the cooling analysis is performed in closed mold till room temperature condition is reached. The heat transfer analysis through the hat structure and development of thermal residual stresses during the cooling process is modeled and simulated as two stages of the cooling step.

2.4.1 Thermoforming simulation

The FE setup to perform thermoforming simulation is shown in Figure 2.10, which consists of punch, die and four binder tabs to hold blank similar to experiments. The hat structure has a length of 145 mm and the blank has a length of 297 mm as shown in Figure 2.10(a). As shown in Figure 2.10(b), the radius of curvature and the width of hat structure are 9.18 mm and 75 mm, respectively. The blank width is 210 mm. The punch, die and binder tabs are modeled as rigid bodies using thin shell elements. The blank is oriented in 0/90 configuration with respect to the punch and die. Four pairs of binder tabs are used to support the blank of which four tabs below the blank are fixed. Each binder tab above the blank (visible in Figure 2.10(a)) applies a constant load of 70 N on the blank (along Y-axis) to hold it in place during forming. To form the blank, the punch travels towards the die till the mold closes completely. The interface between the tools and the blank is modeled as a penalty-based friction contact [45]. The coefficient of friction of 0.2 is selected from a narrow range of values reported previously for forming simulations [46], [47].

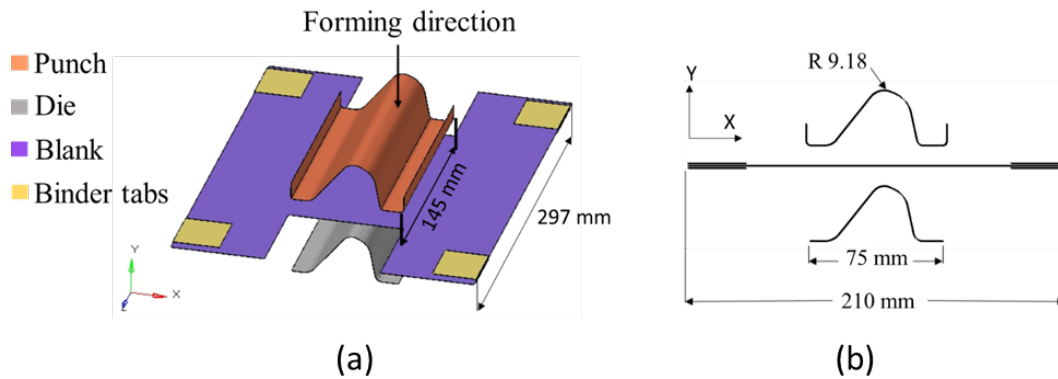


Figure 2.10: (a) Finite element model for forming simulations showing components namely punch, die, blank, binder tabs and forming direction, (b) dimensions and arrangement of components in cross-section view

The thermoforming simulations are performed in HyperForm using RADIOSS, a finite element solver developed by Altair Engineering. The composite blank material behavior is modeled with MAT LAW 58 which is an anisotropic hyperelastic fabric material model. The material model was used previously by Jayasree et al. [28] for forming simulation. In the forming analysis, it is assumed that the strain energy is consumed in the blank deformation only during loading (travel of punch towards die), and the un-loading effect is not considered [48]. In addition, some hypoelastic models [49]–[51] developed for fabrics are based on similar assumptions. Accordingly, the unloading of the blank is not considered in the scope of this work. The thickness of the blank is defined to be 1.97 mm and modeled with fully integrated QBAT shell elements with mesh size of 2 mm. The MAT LAW 58 model employs two local axes oriented in the two fiber directions (warp and weft) and accounts for the interaction between the warp and weft woven tows (shown in Figure 2.11).

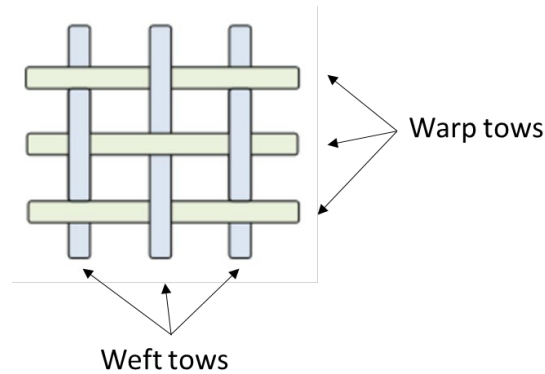


Figure 2.11: Warp and weft tows of the continuous fiber reinforced composite sheet

The local axes follow the rotations of the fibers during element deformation, which enables the in-plane shear behavior. Tensile and shear moduli used as inputs to MAT LAW 58 are listed in Table 2.2 and are calculated from high temperature material characterization data. A bending factor of 0.0015 is defined to relax the tensile stiffness of the fibers in compression mode. It should be noted that the anisotropic hyperelastic fabric material model MAT LAW 58 is employed in this study because the forming is under close to isothermal condition, which means there is no need to consider the thermomechanical effect in this simulation step. The development of thermal stresses during the cooling process is modeled and simulated in a separate step. In addition, the accuracy of the MAT 58 model is ensured as the shear and tensile properties used in the model are obtained by characterizing the composite specimen itself at the forming temperature. Our results show that the model is capable of predicting shear angles and potential sites of wrinkling, which are important for the simulations down the road.

2.4.2 Cooling analysis

During the thermoforming process, internal residual stresses are induced when the formed part, which is still held in position by the punch and die, is cooled to the service temperature. A comprehensive review of residual stresses formation in thermoplastic composites can be found in [52]–[54], and a brief literature review is discussed here. Typically, process induced residual stresses on CFRTP are presented at different length scales of the composite architecture, namely the micromechanical, macromechanical and “global” level [55]. At micromechanical level or fiber/matrix interaction level, these stresses are primarily influenced by the difference in properties of fiber and matrix, such as CTE and Young’s modulus mismatch, and the fiber/matrix interfacial bond strength. While the residual stresses at micromechanical level can be determined using both numerical techniques such as mean field homogenization techniques [36] and experimental techniques such as Raman microscopy and photoelasticity presented in [56], [57], for the material system under consideration, their effect at the laminate level is insignificant. At macromechanical or ply/ply interaction level, the residual stresses mostly arise due to anisotropic shrinkage of lamina during cooling phase which majorly affects unbalanced laminate structure [55], [58]–[60]. However, since a balanced composite layup is investigated here therefore, macromechanical stresses arising in an unbalanced layup are also neglected. At the “global” level, i.e. in case of a thick laminated structure, thermal skin-core stresses are developed along the thickness of the laminate, during the cooling phase [61], [62]. These stresses are primarily developed due to the difference in cooling rate between center and surface plies, resulting in a thermal gradient through thickness. In

the present study, the thermal skin/core stresses at “global” level are considered, which occur due to the development of through-thickness thermal gradient during cooling phase. These stresses are evaluated in two steps. In the first step, a heat transfer analysis is performed to determine the through thickness temperature evolution in the blank, during the cooling phase.

In the second step, the residual skin-core stresses are calculated by incorporating the through thickness temperature evolution data and implementing classical laminate theory-based thermomechanical analysis presented by [62], [63]. The thermoforming process is carried out at the temperature (T) above the melting point of PA6 matrix i.e. at $T > 220$ °C. At this elevated temperature, the structure is assumed to be in a ‘stress-free’ state and the stresses developed during forming is assumed to reduce to zero in the closed mold while cooling from melt temperature ($T_m = 220$ °C) till the glass transition temperature ($T_g = 60$ °C), the PA6 matrix undergoes viscoelastic phase. Below T_g , the PA6 matrix can be assumed to behave elastically till room temperature [2]. Viscoelastic effects have been reported to cause stress relaxation during cooling [62], [64] however, these are neglected in the present work and is planned to be included in future work . Accordingly, the hat structure is assumed to behave elastically while cooling from T_g to room temperature and the residual stresses start to build up, once the temperature drops below T_g .

2.4.2.1 Heat transfer analysis

The transient heat transfer analysis is performed to identify through-thickness thermal gradient in the laminated hat structure. The model setup in the global coordinate

system (x, y, z) is shown in Figure 2.12(a), where the laminated composite hat structure is constrained by the punch and die (closed mold) during the cooling process. The surfaces of blank and the tools are assumed to be in uniform contact thereby, a uniform temperature distribution, along the length of the hat structure (along z -axis) is assumed. Consequently, the three-dimensional heat transfer analysis can be simplified for computational efficiency, into a two-dimensional (x, y) analysis, as shown in Figure 2.12(b). The analysis is carried out using FEM. The punch and die are discretized with a mesh size of 2 mm. The laminated hat structure is discretized with an average mesh size of 0.123 mm in the through-thickness direction and 2 mm along the hat cross-section profile. The FE discretization of the laminated hat structure is illustrated in Figure 2.12(c). A section of the discretized laminate is shown, which is comprised of a stack of 16 thin shell elements of 0.123 mm thickness, each representing a ply. The residual stresses analysis is carried out at each discretized laminate level which will be discussed in the following subsection.

The temperature data of the punch and die is recorded during the cooling phase of thermoforming experiment as mentioned in Section 2.3.4.1. The temperature data of punch and die between 100 °C and room temperature is utilized which is shown in Figure 2.13. The die has a higher rate of cooling as compared to punch, due to relatively lower volume of material. The cooling period of the punch and die is 80s and 40s respectively, beyond which a constant room temperature is observed. These cooling curves are input as boundary conditions to perform the transient thermal analysis. The implicit FE analysis is carried out for the total cooling simulation time, $t = 400$ s. The material properties used for this analysis are listed in Table 2.1. The adjacent plies of the laminate are expected to have micro voids

and defects at the contact interface which may develop thermal contact resistance resulting in increased thermal gradient. This is accounted for by defining a gap conductance of 0.1 mW/mm²K [65]. The through thickness temperature evolution of the hat structure is determined from the transient heat transfer analysis. The temperature data is recorded in an ASCII format which is further used in a MATLAB script to calculate the residual stresses evolution through laminate thickness.

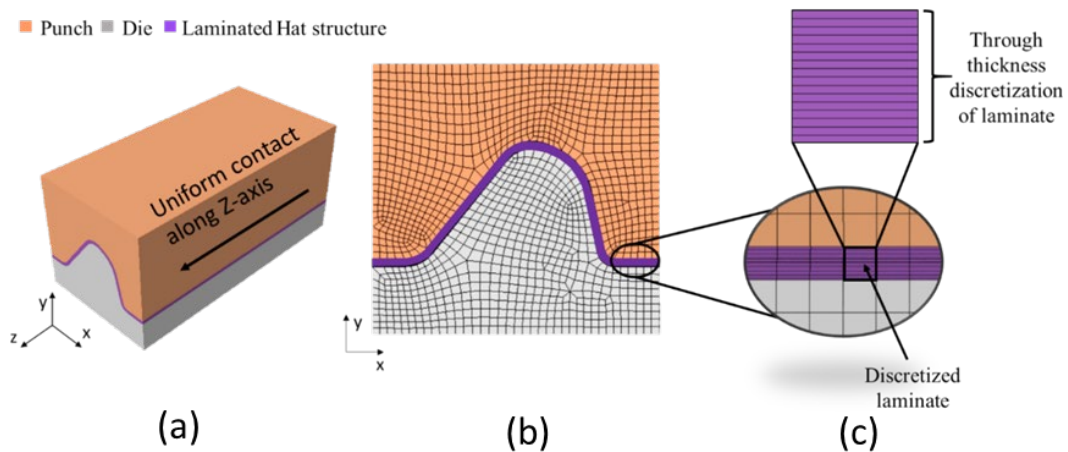


Figure 2.12: (a) Finite element 3D model setup in global coordinate system (x,y,z), (b) simplified 2D (x,y) model setup for transient heat transfer simulation (c) FE discretization of the laminated hat structure

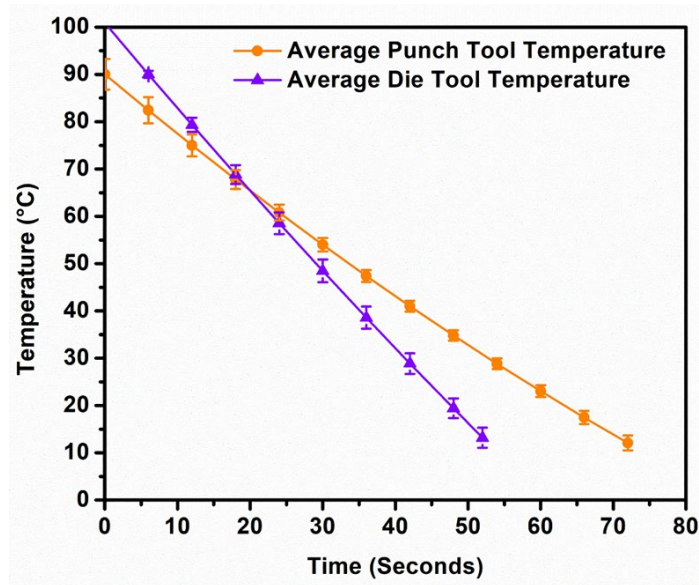


Figure 2.13: Cooling curves defined for Punch and Die obtained as average from 3 experimental trials. Punch has an initial cooling rate of $-1.3\text{ }^{\circ}\text{C/s}$, Die has a cooling rate of $-1.8\text{ }^{\circ}\text{C/s}$

2.4.2.1 Determination of residual stresses

The residual stresses due to through thickness thermal gradient in a laminated composite structure can be determined by following the incremental classical laminate theory based thermomechanical analysis as discussed by [62], [63]. According to this, the cooling process is discretized into n time steps and the residual stresses at ply level (incremental ply stresses) are determined at each time step. Since the elastic constitutive model is used herein, the residual stresses at the end of cooling process for any given ply, can now be calculated by taking a cumulative sum of these incremental ply stresses. This analysis is carried out by implementing FE approach using a MATLAB script. The same discretization strategy as discussed for transient heat transfer analysis is utilized herein. To explain the analysis, consider a laminate structure comprised of 16 plies, oriented at an angle (θ) w. r. t. global coordinate system (x, y, z) as shown in Figure 2.14(a). Also shown,

is the laminate local coordinate system or the analysis system (x_1, x_2, x_3) , where x_2 is laminate thickness direction.

Figure 2.14(b) shows the arbitrarily selected k -th ply having thickness e_k , and the distance from laminate midplane to ply midplane is h_k . Since the analysis is done at each discretized laminate level, the following discussion is presented in the analysis system (x_1, x_2, x_3) . The thickness of the ply (x_2) is considered very small as compared to in-plane (x_1, x_3) dimensions of a ply. Therefore, a 2D plane stress analysis is carried out, where in-plane residual stresses are developed due to thermal gradient along x_2 . These residual stresses are primarily driven by the volumetric shrinkage effect during the cooling process. The temperature evolution data obtained from the transient thermal analysis is used to first deduce the ‘stress free’ incremental thermal strains for the k -th ply at a given time step t . The mean temperature of each ply at a particular time instance is determined by taking an average of the 4 corner nodal temperatures. The ‘stress free’ herein, refers to the thermal strains developed in a ply, when it is free to deform without any constraint, which can be calculated by:

$$\begin{bmatrix} (\Delta \varepsilon_{x_1}^T) \\ (\Delta \varepsilon_{x_3}^T) \\ (\Delta \varepsilon_{x_1 x_3}^T) \end{bmatrix}_k = \begin{bmatrix} (\varepsilon_{x_1}^T)_t - (\varepsilon_{x_1}^T)_{t-1} \\ (\varepsilon_{x_3}^T)_t - (\varepsilon_{x_3}^T)_{t-1} \\ (\varepsilon_{x_1 x_3}^T)_t - (\varepsilon_{x_1 x_3}^T)_{t-1} \end{bmatrix}_k = \begin{bmatrix} \alpha_{x_1} \\ \alpha_{x_3} \\ \alpha_{x_1 x_3} \end{bmatrix} (\Delta T)_k \quad (2.3)$$

where, $\alpha_{x_1}, \alpha_{x_3}$ and $\alpha_{x_1 x_3}$ are the in-plane thermal expansion coefficients and $(\Delta T)_k = (T_t - T_{t-1})_k$ is the temperature change for a timestep, ε is the strain, subscript $x_1, x_3, x_1 x_3$ denotes the direction of strain, superscript T refers to thermal strain and subscript t denotes the time step. The net deformation of any given k -th ply in a laminate

is dictated by the thermal and mechanical properties of all the plies in that laminate. In other words, an individual ply strain is affected by the average laminate strain. This difference between the average laminate strain and the ‘stress free’ ply strains (from Equation (2.3)) causes the residual stresses to develop in the ply. This is illustrated in the Figure 2.14(c), where a laminate structure comprised of two plies is shown. In an unconstrained state, ply 1 and ply 2, undergo ‘stress free’ strains ϵ_1 and ϵ_2 respectively. However, in the laminate setup both plies undergo average laminate strain ϵ_m . Therefore, the stresses in ply 1 are proportional to $\epsilon_1 - \epsilon_m$ and that in ply 2 are proportional to $\epsilon_2 - \epsilon_m$.

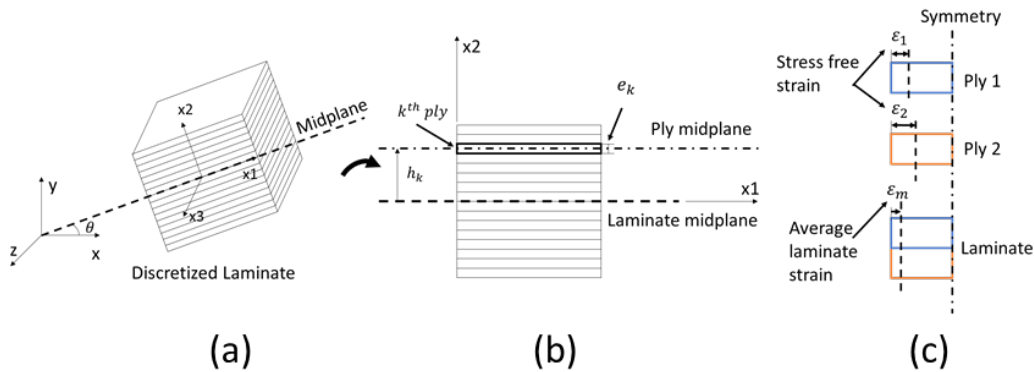


Figure 2.14: Illustration of (a) a discretized laminate orientated at an angle (θ) w.r.t. global coordinate system (x,y,z). (b) k-th ply at a distance h_k from laminate midplane, and (c) stress free strains vs average laminate strain

Typically, the average laminate strains are represented by the strains occurring in the laminate midplane due to introduction of thermal loading on the laminated structure. The thermal loading herein, can be defined by the resultant forces and moments that act on the laminated structure, and is expressed as the cumulative sum of thermal forces on all plies. The resultant forces on the laminate are calculated at each time step t , i.e. incremental

resultant forces (N). Since, the cooling process takes place in a closed mold where the laminate is constrained in all directions therefore, out-of-plane deformations within the plies do not exist. Consequently, the curvatures and moments are neglected, and the incremental resultant forces are expressed in simplified form as [66]:

$$\begin{bmatrix} \Delta N_{x1}^T \\ \Delta N_{x3}^T \\ \Delta N_{x1x3}^T \end{bmatrix} = \begin{bmatrix} (N_{x1}^T)_t - (N_{x1}^T)_{t-1} \\ (N_{x3}^T)_t - (N_{x3}^T)_{t-1} \\ (N_{x1x3}^T)_t - (N_{x1x3}^T)_{t-1} \end{bmatrix} = \sum_{k=1}^{nn} \left\{ \begin{bmatrix} \bar{Q}_{11} & \bar{Q}_{12} & \bar{Q}_{16} \\ \bar{Q}_{12} & \bar{Q}_{22} & \bar{Q}_{26} \\ \bar{Q}_{16} & \bar{Q}_{26} & \bar{Q}_{66} \end{bmatrix}_k \begin{bmatrix} \Delta \varepsilon_{x1}^T \\ \Delta \varepsilon_{x3}^T \\ \Delta \varepsilon_{x1x3}^T \end{bmatrix} \int_{h_{k-1}}^{h_k} dx \right\} \quad (2.4)$$

Where, $\bar{Q}_{ij} = \bar{Q}_{ij}(T)$, $\{i, j = 1, 2, 6\}$ is transformed plane stress stiffness matrix which is defined [67] in terms of the engineering properties. Now the incremental laminate strain or the laminate mid-plane strain can be calculated at time step t , by following the laminate constitutive relationship as [66]:

$$\begin{bmatrix} \Delta \varepsilon_{x1}^0 \\ \Delta \varepsilon_{x3}^0 \\ \Delta \varepsilon_{x1x3}^0 \end{bmatrix} = \begin{bmatrix} (\varepsilon_{x1}^0)_t - (\varepsilon_{x1}^0)_{t-1} \\ (\varepsilon_{x3}^0)_t - (\varepsilon_{x3}^0)_{t-1} \\ (\varepsilon_{x1x3}^0)_t - (\varepsilon_{x1x3}^0)_{t-1} \end{bmatrix} = [\mathbf{A}]^{-1} \begin{bmatrix} \Delta N_{x1}^T \\ \Delta N_{x3}^T \\ \Delta N_{x1x3}^T \end{bmatrix} \quad (2.5)$$

where, $\Delta \varepsilon^0$ represents increments in laminate midplane strain from the previous time step. The matrix \mathbf{A} is the 3-by-3 in-plane stiffness matrix for the laminate. It is worthwhile to note that, the coupling factor in the stiffness matrix is neglected herein, since a balanced layup is considered. The coefficient of the \mathbf{A} matrix is given by, $A_{ij} = \sum_{k=1}^{nn} (\bar{Q}_{ij})_k e_k$. The thermoelastic constitutive equation for the k^{th} ply can now be obtained

in the incremental form by incorporating the incremental ‘stress free’ ply strains from Equation (2.3) and laminate strains from Equation (2.5) respectively, into the Duhamel-Neumann form of Hooke’s law [68]. The resulting incremental stresses in k^{th} ply is expressed as:

$$\begin{bmatrix} \Delta\sigma_{x1} \\ \Delta\sigma_{x3} \\ \Delta\sigma_{x1x3} \end{bmatrix}_k = \begin{bmatrix} (\sigma_{x1})_t - (\sigma_{x1})_{t-1} \\ (\sigma_{x3})_t - (\sigma_{x3})_{t-1} \\ (\sigma_{x1x3})_t - (\sigma_{x1x3})_{t-1} \end{bmatrix}_k = [\bar{Q}_{ij}]_k \left(\begin{bmatrix} \Delta\varepsilon_{x1}^0 \\ \Delta\varepsilon_{x3}^0 \\ \Delta\varepsilon_{x1x3}^0 \end{bmatrix} - \begin{bmatrix} \Delta\varepsilon_{x1}^T \\ \Delta\varepsilon_{x3}^T \\ \Delta\varepsilon_{x1x3}^T \end{bmatrix}_k \right) \quad (2.6)$$

where, $\Delta\sigma$ is incremental residual stresses for a ply. The residual stresses at the end of cooling process can be obtained by taking cumulative sum of the incremental stresses computed using Equation (2.6). This can be expressed for k -th ply as:

$$\begin{bmatrix} \sigma_{x1} \\ \sigma_{x3} \\ \sigma_{x1x3} \end{bmatrix}_k = \sum_{t=1}^n \begin{bmatrix} \Delta\sigma_{x1} \\ \Delta\sigma_{x3} \\ \Delta\sigma_{x1x3} \end{bmatrix}_k \quad (2.7)$$

The final step before mapping the residual stresses to a FE solver is to transform the ply stresses from analysis system to the global coordinate system using the transformation matrix. This is done for each ply and the stress transformation can be expressed for k -th ply as:

$$\begin{bmatrix} \sigma_x \\ \sigma_y \\ \sigma_z \\ \sigma_{yz} \\ \sigma_{xz} \\ \sigma_{xy} \end{bmatrix}_k = \begin{bmatrix} c^2 & s^2 & 0 & 0 & 0 & -2sc \\ s^2 & c^2 & 0 & 0 & 0 & 2sc \\ 0 & 0 & 1 & 0 & 0 & 0 \\ 0 & 0 & 0 & c & s & 0 \\ 0 & 0 & 0 & -s & c & 0 \\ sc & -sc & 0 & 0 & 0 & c^2 - s^2 \end{bmatrix} \begin{bmatrix} \sigma_{x1} \\ 0 \\ \sigma_{x3} \\ 0 \\ \sigma_{x1x3} \\ 0 \end{bmatrix}_k \quad (2.8)$$

Where, c denotes $\cos(\theta)$ and s denotes $\sin(\theta)$. This analysis was repeated for all other discretized laminates along the cross-section profile since the through-thickness temperature gradient could be different at different locations. The global residual stresses are extracted and saved in ASCII format for each discretized laminate. The data is further used in stress mapping code discussed in following section. The material properties required for this analysis are listed in Table 2.1 and Table 2.2.

2.4.3 Mapping of numerical results

A mapping procedure is generally employed to continue analysis either in the same or different solver by transferring the results obtained from one simulation to the next. For example, in large deformation problems, the elements are often distorted to such an extent that they cannot be used for further analysis. Mapping of results to a new mesh becomes necessary. In some other cases, the analysis needs to be continued in a different solver, which requires the results from the previous analysis to be transferred to the new solver. In the current study, the process induced effects such as thickness variations, fiber reorientations and residual stresses are mapped on a new mesh of the hat structure suitable for mechanical analysis. For the thermoforming results, the ‘‘Result Mapper’’ tool within the Altair Hyperworks software is used for performing the result mapping procedure. For

the residual stresses, a MATLAB script is developed for the mapping. In both cases, mapping of results is based on an algorithm that approximates the result data locally using polynomial functions and in turn uses the functions to calculate the result values on a different mesh or at different locations on the mesh.

2.4.4 Mechanical performance validation

The last step of the MTR pathway is to evaluate the mechanical response of the hat structure, with the process induced effects included. In the current study, a quasi-static three-point bend test and a dynamic impact test is carried out to validate the MTR pathway. The FE analysis is carried out by using the LS-DYNA solver.

2.4.4.1 Quasi-static three-point bend test

The composite material behavior is modeled using LS-DYNA material law MAT 58 (MAT_Laminated_Composite_fabric) which models the anisotropic behavior of composite and implements the damage mechanics using the Matzenmiller-Lubliner-Taylor model [69]. The material model utilizes the Hashin failure criterion [70] with thin shell elements to model composite laminates and woven fabrics. The material model also incorporates the nonlinear portion of the shear stress-strain curve. More description can be found in [71]. The MAT 58 card is calibrated for the PA6 laminate by carrying out the experiments discussed in Section 2.3.3. Figure 2.15 shows the FE model setup consisting of the thermoformed composite part, a rigid impactor and two rigid cylindrical supports of 10 mm diameter. The bottom of the thermoformed hat section is joined with a 0.5 mm flat composite spine section using an adhesive layer. The 1.97 mm thick adhesive layer has

width of 10 mm on both sides of hat section which is modeled using solid cohesive elements which act like springs in through-thickness direction. The cohesive mixed mode material model [72] is used to model adhesives which follows purely elastic behavior with bilinear traction separation failure law.

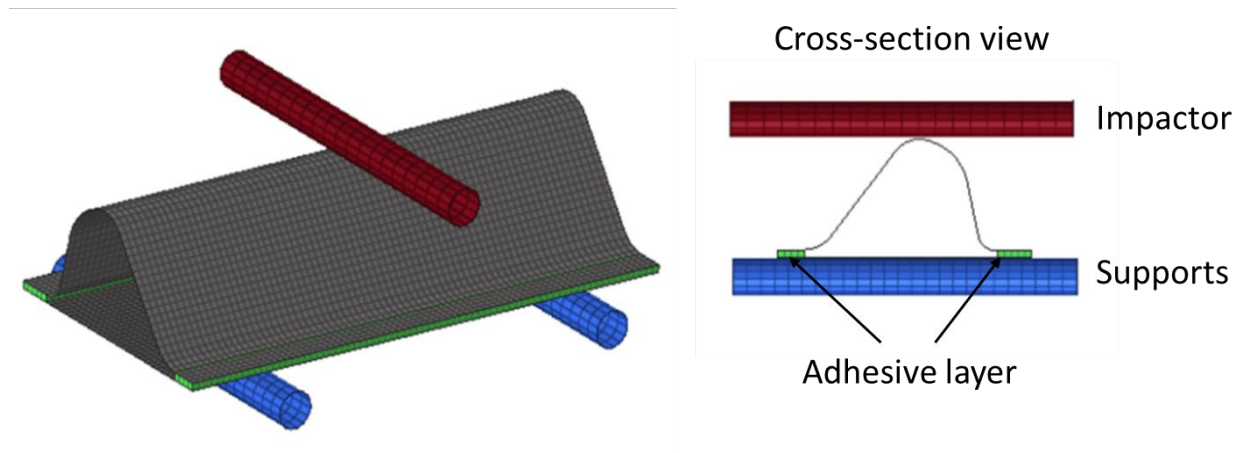


Figure 2.15: FE model setup for mechanical tests showing thermoformed hat structure adhesively bonded with spine along with rigid impactor and supports.

2.4.4.2 Dynamic impact test

An impact test with 28.75J impact energy is simulated in LSDYNA by striking a 3.1kg rigid cylinder to the hat structure with the impact velocity of 4.3m/s. The model setup and boundary conditions are applied such that it replicates the experiments. Figure 2.16 shows the FE model setup for impact tests where a hat structure is placed over a rigid fixture. The clamp conditions on flat edges of hat structure as described in the experiment section are simulated by applying SPC boundary conditions on the nodes constraining all six degrees of freedom. To model composite material, enhanced composite damage

material model, MAT54 is used. The material card utilizes Chang-Chang failure criterion [73] where matrix failure (tension) is given by:

$$\left(\frac{\sigma_2}{Y_t}\right)^2 + \bar{\tau} = 1 \quad (2.9)$$

and matrix failure (compression) is given by:

$$\left(\frac{\sigma_2}{2S}\right)^2 + \left[\left(\frac{Y_c}{2S}\right)^2 - 1\right] \frac{\sigma_2}{Y_c} + \bar{\tau} = 1 \quad (2.10)$$

fiber tensile failure:

$$\left(\frac{\sigma_1}{X_t}\right)^2 + \beta \bar{\tau} = 1 \quad (2.11)$$

and fiber compressive mode failure is given by:

$$\left(\frac{\sigma_1}{X_c}\right)^2 = 1 \quad (2.12)$$

Where, X_t , X_c , Y_t , Y_c and S are longitudinal tensile strength, longitudinal compressive strength, transverse tensile strength, transverse compressive strength, and shear strength respectively, which are obtained from material strength measurement. The principal stresses in directions 1 and 2 are represented by σ_1 and σ_2 respectively. The shear stress is denoted by symbol $\bar{\tau}$ and β represents weighting factor for shear term in tensile fiber mode, which lies between 0 and 1. A thin shell element approach is implemented wherein the laminate layup is defined by a single integration point for each single ply consisting of respective fiber orientation and thickness. The failure modes described in

Equation (2.9)-(2.12) reduces the ply stresses to a limiting value which is greater than zero. These limiting stress values depend upon the SLMX parameters which are empirically fitted in the MAT54 card and are typically between 0 and 1. The ply stresses reduce to zero by defining five critical strain failure values viz. strain to failure in fiber tension (DFAILT) and compression (DFAILC), strain to failure in matrix (DFAILM), strain to failure in shear direction (DFAILS) and effective failure strain (EFS) [71]. Once, the failure criteria are satisfied for all the plies, then whole element is eroded. The nearby elements become “crashfront” elements and their strength can be reduced based on the SOFT parameter. A fully integrated shell element formulation (ELFORM =16) is used to eliminate hourglass modes and laminate shell theory is invoked by setting LAMSHT=1 in *CONTROL_SHELL. This option removes the usual assumption of uniform shear strain through the thickness of the shell which is important for sandwich composites with soft cores [71]. MAT 54 card is sensitive to mesh size, contact formulation and non-physical crashfront softening parameter SOFT.

For instance, it is possible to obtain two combinations of MAT54 parameters at two different mesh sizes that shows a reasonable correlation to experiments. It is also observed that a MAT54 calibrated for coarser mesh if transferred upon a finer mesh model, the element erosion may progress faster and could show numerical instabilities [74]–[76]. An optimal mesh selection approach for MAT54 card requires trade-off between accuracy and computational time and it should also closely replicate the physical damage behavior. After careful calibration with the experimental data, in the current study a mesh size of 2 mm × 2 mm is used and which is kept consistent throughout the MTR pathway. The LS-Dyna

keyword *PART_COMPOSITE is used to define individual composite layers along with their thickness and offset angle (BETA).

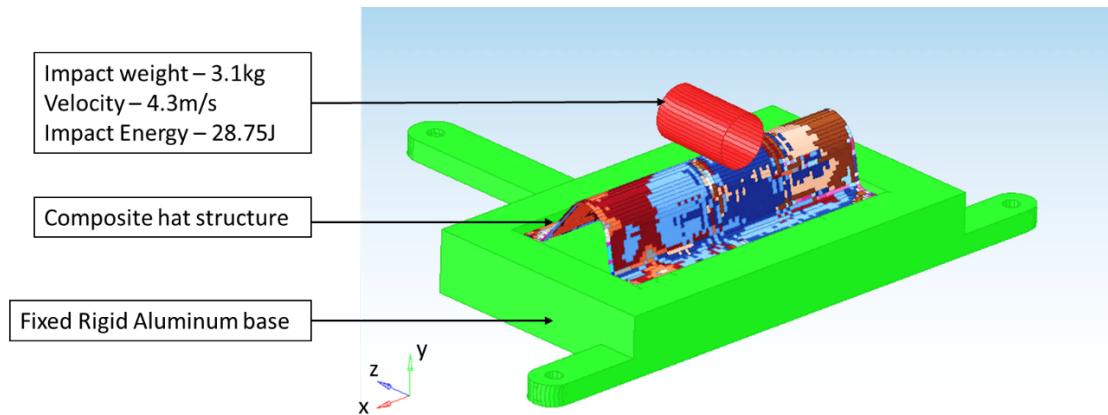


Figure 2.16: FE model setup for impact test showing thermoformed hat structure with rigid impactor and fixed support. Each colored zone on hat represents LSDYNA part composite that embodies a unique set of stack up order of composite laminate

2.4.5 Numerical parametric study: Static and dynamic analysis

The thermoforming process may result in variations in thickness distribution, fiber orientation and residual stresses distribution due to factors such as complex geometry, thermoforming tool clearance and surface finish. In this study, for the purpose of demonstrating the MTR pathway, a thermoforming tool with high surface finish is used to form a hat section structure with relatively simple and smooth geometric shape. As a result, no large variations in thickness and fiber orientations are produced. To understand the effect of large variations in thickness and fiber orientation on the structural response under static and dynamic loading. In our numerical studies, we artificially increase the range of

thickness and fiber orientation variations on the same hat section geometry. The different variations in residual stresses are obtained by carrying out cooling analysis discussed in Section 2.4.2 for various cooling rates. The computational model is setup to carry out static and dynamic analysis with the inclusion of these variations. The results are obtained for several cases and compared with the response of the hat structure without considering thickness and fiber orientation variations and residual stresses.

2.4.5.1 Static analysis

The static test is first carried out to evaluate the overall stiffness of the hat structure. This is done by setting up six static load cases as illustrated in Figure 2.17 which are (a) longitudinal compression, (b) longitudinal shear, (c) longitudinal bending, (d) transverse compression, (e) transverse shear and (f) transverse bending. An implicit FE analysis to solve the linear static problem is setup in LS_DYNA. To model the composite behavior MAT 58 discussed previously is used. The static problem can be written in discretized form as:

$$\mathbf{K}\mathbf{u} = \mathbf{f}_{ext} \quad (2.13)$$

where, \mathbf{K} is stiffness matrix, \mathbf{u} represents the displacement vector and \mathbf{f}_{ext} is the external forces vector. A force of 4 N is applied to each node of the loading edge which results into an external force of 220 N for the three longitudinal load cases while a force of 304 N for the three transverse load cases. The corresponding deflection is measured and compared for all the cases.

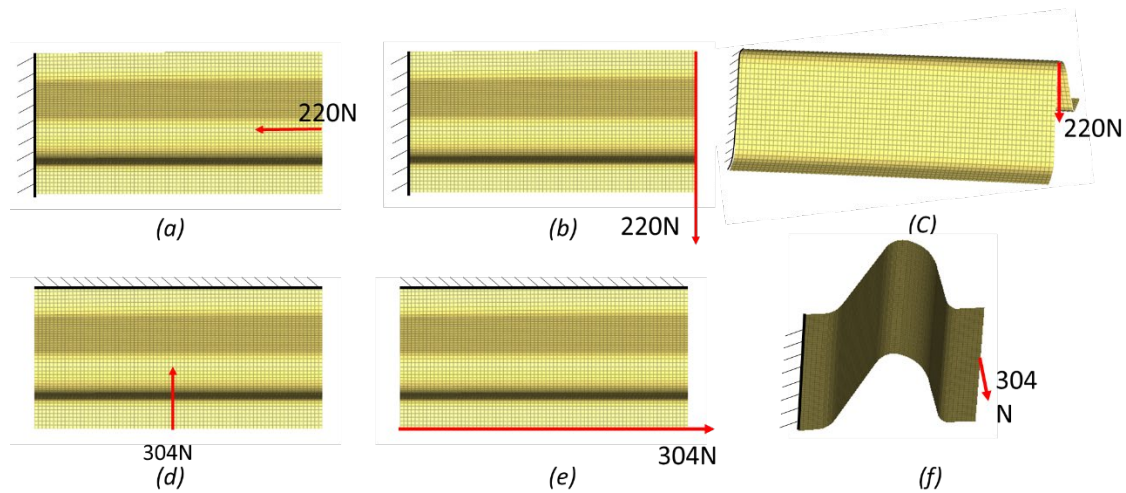


Figure 2.17: A schematic diagram of six static load cases representing (a) longitudinal compression, (b) longitudinal shear, (c) longitudinal bending, (d) transverse compression, (e) transverse shear and (f) transverse bending.

2.4.5.2 Dynamic analysis

The dynamic impact test is simulated on the thermoformed hat structure in LSDYNA using the modeling strategy as described earlier. However, for the purpose of parametric study a higher energy impact 57.5 J is simulated. Further, a cylindrical impactor results in localized deformation in the hat structure and may not give the complete picture of various process induced effects. Therefore, a large contact area impact test using a rigid plate impactor is performed for the parametric study as shown in the Figure 2.18. The edges of the hat section are kept fixed while a rigid support at the bottom of the structure is placed to hat structure to collapse.

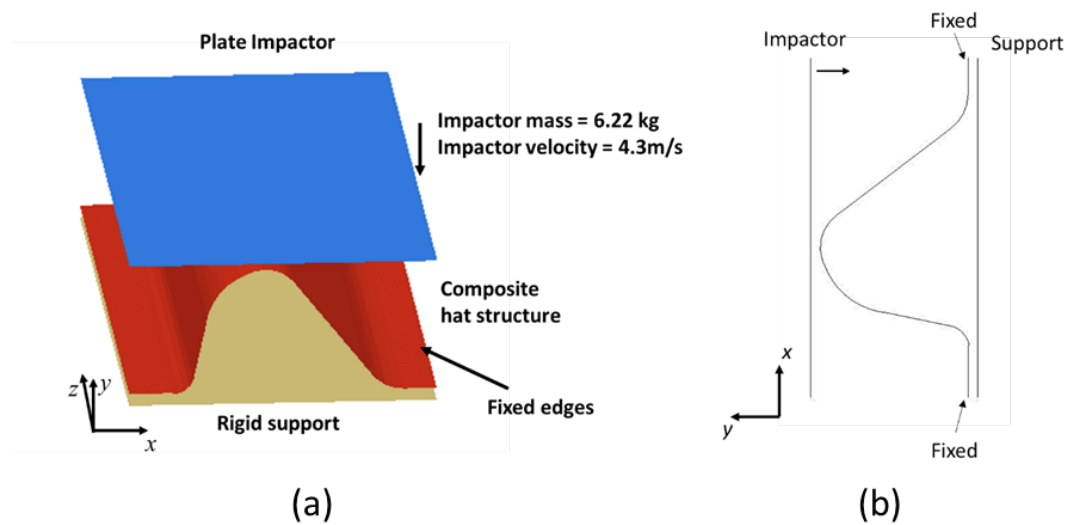


Figure 2.18: FE model setup of the impact test showing composite hat structure with fixed edges impacted by a rigid plate (a) front view and (b) 2D cross sectional view.

2.5 Results and discussion

2.5.1 Model validation (Experimental vs numerical)

The MTR pathway developed in this study is validated at two steps i.e. first at the manufacturing stage which is followed by the mechanical testing stage. At the manufacturing stage, thickness variations and fiber reorientations are validated at structure level. At the mechanical testing stage, the combined effect of residual stresses, thickness variations and fiber reorientations on the structural response is validated with the experiments.

2.5.1.1 Thermoforming results: Thickness variation and Fiber Orientations

The thickness variation and fiber orientations are experimentally measured after performing the thermoforming experiments and is compared with the numerical results. The thickness is measured at six different locations along the hat profile (or three locations

each side) and the average thickness from the three experimental trials is presented in Figure 2.19. The maximum thickness of 2.01 mm is observed at location 5 with the standard deviation of 0.008 mm, while the minimum thickness of 1.97 mm is observed along the flatter edges locations 1 and 3 with the standard deviation of 0.01 mm. Figure 2.19 also presents the numerically predicted thickness contour along the two sides of hat structure. The numerical thickness variation is predicted using the draping tool of Altair Hyperworks. A comparison between the measured thickness and the predicted thickness shows good agreement.

Further, the warp and weft tows of the composite sheet are referred here as fibers in directions 1 and 2 initially 90° apart. These fibers of the composite sheet undergo reorientation as the sheet deforms to take the shape of the mold. Figure 2.20 shows a comparison of fiber orientations obtained from the experiments and simulation, where the change in angle between the two fiber directions is measured. On the fabricated hat structure, four locations are identified (highlighted square in the Figure 2.20) so as to capture fiber orientations at different geometric curvatures of hat structure. To compare with the numerical results, a closer view of these locations is shown in Figure 2.20 along with the numerically obtained contour plot of fiber orientations at the four specified locations. The maximum fiber angle of 103° can be observed from the contour plot near location 4, which means a fiber reorientation of 13° . The average fiber orientations from the three experimental trials are determined and compared with the numerical prediction. The comparison is listed in Table 2.3 for the four locations which shows good agreement.

Note that both the thickness variations and fiber orientations need to be mapped to the hat structure before mechanical validation.

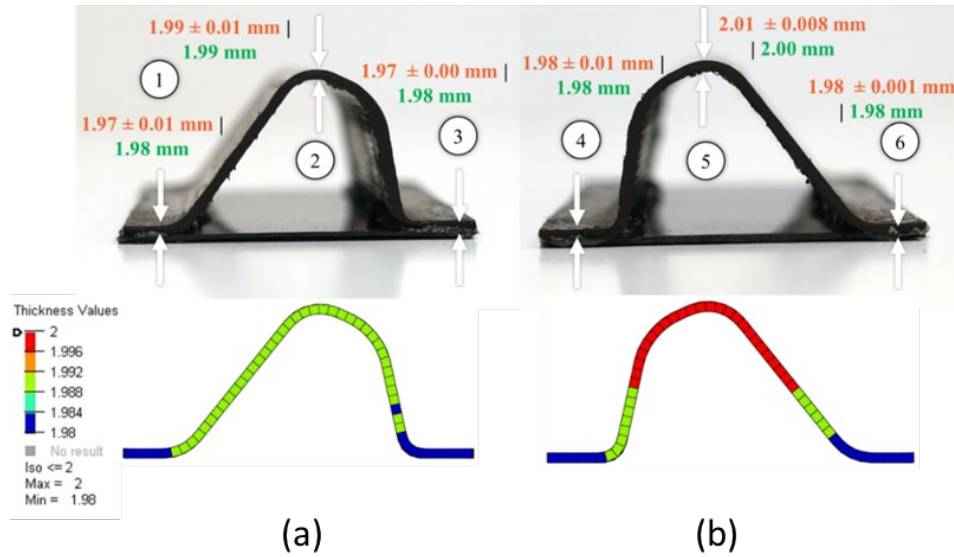


Figure 2.19: Thickness variation in the hat structure: (a) Side 1, (b) Side 2 represented as (upper) measured average thickness \pm standard deviation and (lower) predicted thickness variation.

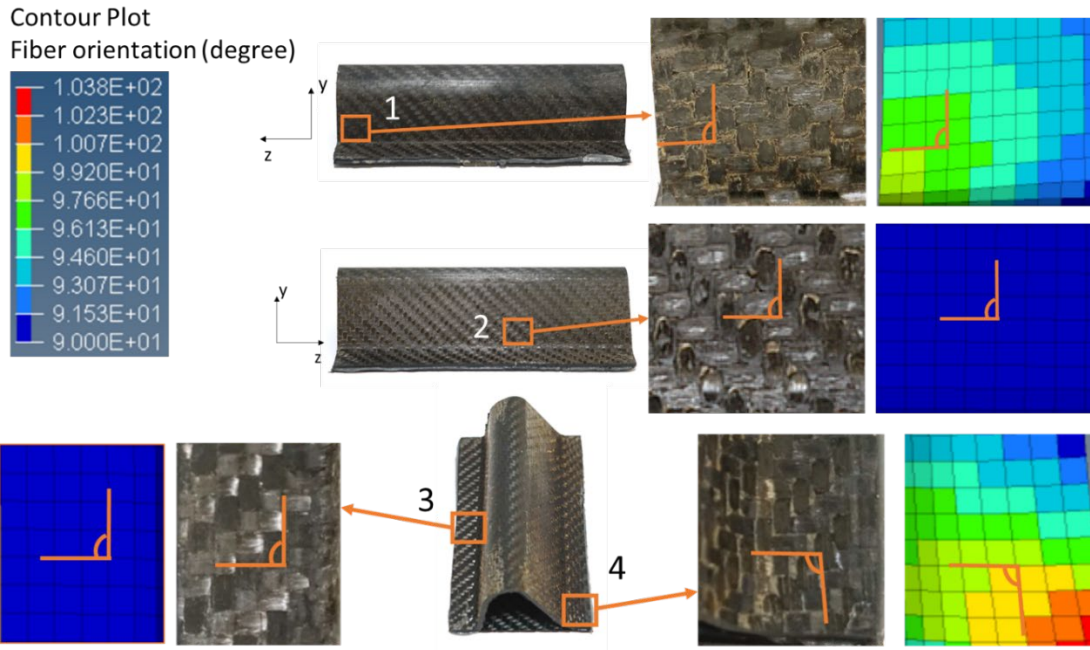


Figure 2.20: Fiber orientation in degree as observed in thermoforming trials and simulation at marked locations of the hat structure

Table 2.3: Fiber orientations in degree from experiments and simulation at four locations on the hat structure

Location	Experimental Average	Std.	Simulation	%Difference
1	96.76	1.42	95.77	1.02
2	91.90	3.19	90.18	1.87
3	90.93	0.81	90.00	1.03
4	100.08	5.17	96.72	3.36

2.5.1.2 Residual stresses: validation and results

The residual stress model described in Section 2.4.2.1 is implemented for APC-2 composite laminates to validate the residual stress calculation procedure with prediction results reported by Chapman et al. [62]. The laminate consists of 40 unidirectional APC-2 sheets amounting to a total thickness of 5 mm. The temperature evolution data through the laminate thickness and cooling curve reported in [62] are used as input. Residual stresses evolution in the transverse direction (perpendicular to the fiber direction) for surface and center plies is reported in the paper and used for comparison with this work as shown in Figure 2.21(a). Furthermore, the distribution of transverse residual stresses through the laminate thickness at $t = 60$ sec is compared with the predicted results for an initial cooling rate of $35\text{ }^{\circ}\text{C/s}$ as shown in Figure 2.21(b). It is important to note that a curve is fit through the data points obtained in this work for Figure 2.21(b). It is shown that the results obtained from the residual stresses model compare reasonably well with the model prediction data from [62]. The discrepancy in results can be attributed to the fact that the effect of degree of crystallinity on the material properties is not considered in the residual stresses model here.

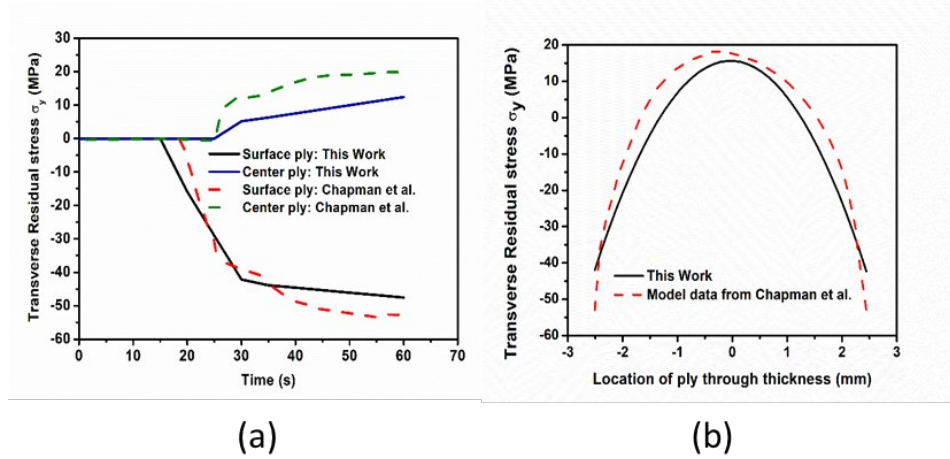


Figure 2.21: Validation of Residual stresses code with model prediction data from Chapman et al. [62] (a) Comparison of transverse residual stresses σ_y evolution for surface and center plies, (b) comparison of transverse residual stresses σ_y distribution through the laminate thickness at $t = 60$ sec

To illustrate the residual stresses evolution, consider a discretized laminate as shown in Figure 2.22(a). This laminate is oriented at an angle ($\theta = 19.2^\circ$) w. r. t. global coordinate system (x, y, z). As discussed earlier, the die has a higher rate of cooling than the punch therefore, the ply immediately in contact with the die (S1) cools faster than the ply in contact with the punch (S2). Consequently, higher compressive stresses are developed in S1 as compared to S2 resulting in an asymmetric stress profile along the thickness of the laminate. This asymmetry can be observed in the Figure 2.22(c), where residual stresses ($\sigma_z, \sigma_x, \sigma_y, \sigma_{xy}$) are plotted against the location of ply (h) through thickness, where h ranges from -1 to 1. These stresses are according to Eq. (8) in Section 2.4.2.1. Tensile stresses are observed towards the center ply ($h = 0$) while compressive stresses are observed going from center towards the two surface plies at $h = +1$ and $h = -1$. The magnitude of residual stresses observed in $\sigma_z, \sigma_x, \sigma_y, \sigma_{xy}$ in Figure 2.22(c) at the center

ply $h = 0$ and at two surface plies at $h = +1$ and $h = -1$ are tabulated in Table 2.4. The residual stresses (σ_z) evolution during simulation time, $t = 400$ s, is presented for center and surface plies S1 and S2 in Figure 2.22(b).

As mentioned earlier, the residual stresses buildup starts once any ply in the laminated hat structure reaches T_g ($=60$ °C) of PA6 matrix. Owing to the difference in cooling rates of punch and die, surface ply S1 reaches T_g earlier than S2 and starts developing residual compressive stresses. As a result of the temperature gradient between the S1 and S2 surface plies, the initial tensile stresses are induced in S2. These tensile stresses are relieved once the temperature gradient reduces over time and compressive stresses start emerging as seen in Figure 2.22(b). The residual stresses are mapped on the hat structure for each discretized laminate to carry out the mechanical tests. Figure 2.23 shows the contour plot of residual stresses (σ_z) distribution on the center and surface plies S1 and S2, for the 3D laminated hat structure. Recall that a uniform contact along the z-axis of the hat profile is assumed during the heat transfer analysis. As a result, the residual stresses magnitude along z-axis for each discretized laminate is uniform as seen in Figure 2.23.

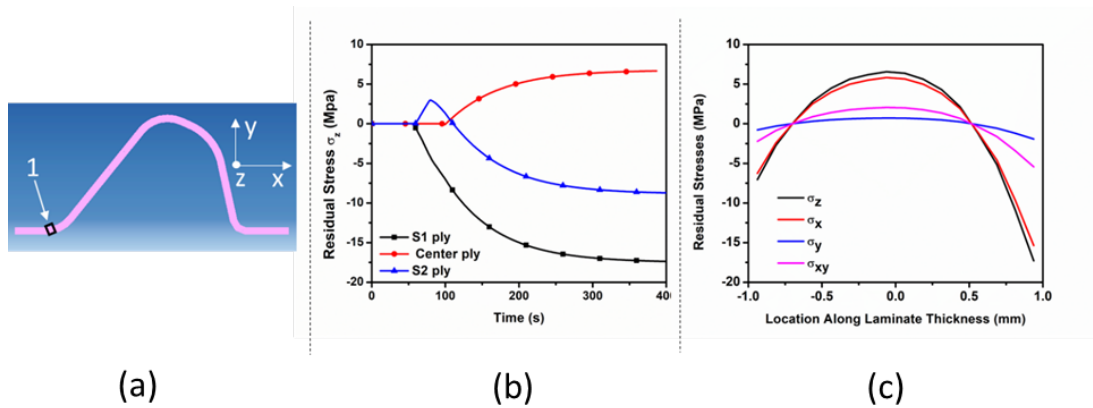


Figure 2.22: (a) A discretized laminate considered from the hat structure, (b) evolution of residual stresses (σ_z) in surface plies S1, S2 and center ply through $t = 400$ s, (c) residual stresses ($\sigma_z, \sigma_x, \sigma_y, \sigma_{xy}$) against the location of ply (h) through thickness, where h ranges from -1 to 1.

Table 2.4: Magnitude of residual stresses ($\sigma_z, \sigma_x, \sigma_y, \sigma_{xy}$) at Surface, $h = \pm 1$ and center, $h = 0$ plies

Residual stress (MPa)	σ_z	σ_x	σ_y	σ_{xy}
Center, $h = 0$	6.56	5.82	0.72	2.06
Surface, $h = +1$	-17.3	-15.36	-1.92	-5.43
Surface, $h = -1$	-7.03	-6.24	-0.78	-2.2

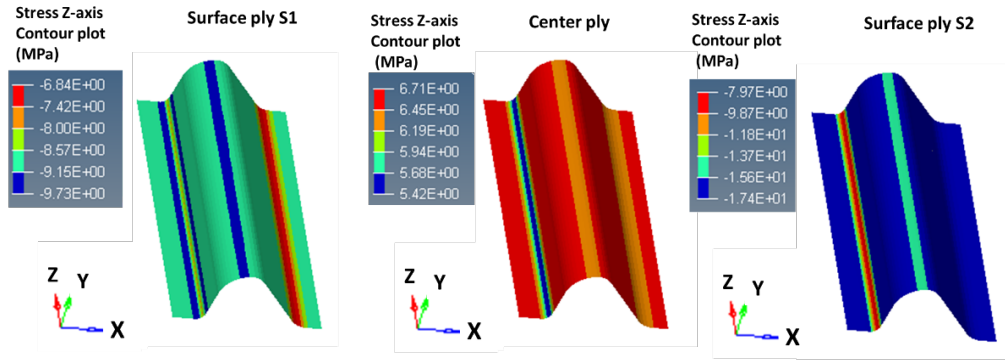


Figure 2.23: Contour plot showing residual stresses distribution along Z-axis on center and surface plies S1 and S2 of the laminated hat structure.

2.5.2 Mechanical performance validation

2.5.2.1 Quasi static test validation

The experimental and numerical performance of thermoformed hat structure under quasi-static 3-point bending test is presented here. The force vs displacement plot is compared in Figure 2.24 and the damage behavior is presented in Figure 2.25. Figure 2.24(a) presents the force vs displacement plot of the three experimental trials. It can be observed that all three trials show a consistent and repeatable linear stiffness zone. The three trials also show consistent failure initiation at approximately 6 mm deflection across all samples. Additionally, the location, time, and displacement at which crack initiation occur is very consistent across 3 samples as shown in Figure 2.25(a). The trials do show a slightly varied force displacement response post 7 mm deflection with trial one exhibiting a peak load of ~ 5877 MPa at 10 mm deflection while trial 2 and trial 3 show loads around 5272 MPa and 4652 MPa, respectively, at the same deflection. The final shape and deflection of the crack vary slightly across the three samples with trial 1 showing the least damage in terms of crack diameter and deflection and trial 3 showing the most damage.

The numerical 3-point bend test under quasi-static loading condition is carried out using LS-DYNA after mapping the thermoforming effects. The force-displacement response is compared with the mean experimental results in Figure 2.24(b), which show a very good agreement till damage onset. The large deformation is observed at impact location of hat structure and the numerical damage prediction is compared with the three experimental trials as shown in Figure 2.25(a). It is observed that numerical prediction of deformation closely matches trial 3. Figure 2.25(b) presents top view of hat structure along with von-Mises stress contour and the encircled regions (in red) show damaged locations. The damage behavior is consistent with the experimental results. However, it should be noted that delamination failure and damage propagation which requires detailed damage modeling strategy are not considered in the study.

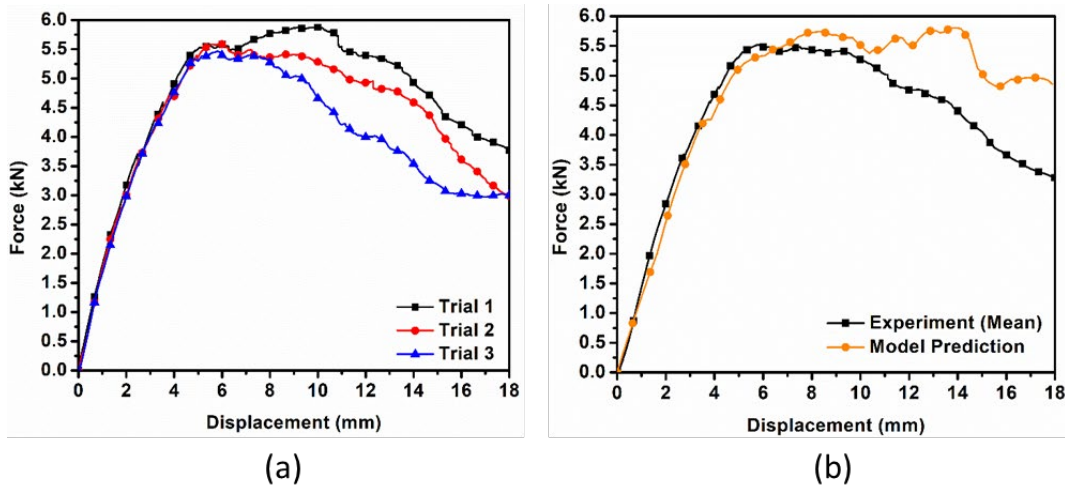


Figure 2.24: (a) Force-displacement plot of three experimental trials (b) force-displacement plot for 3-point bend test comparing experimental response with numerical prediction.

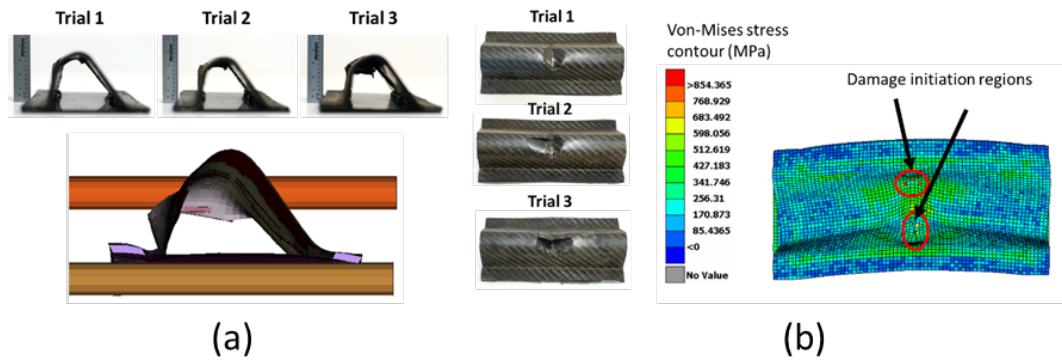


Figure 2.25: Deformation comparison between experimental trials and numerical simulations (a) deformation side view: close match with experimental trial 3 and (b) top view comparison with stress contour plot. Encircled are the damage initiation locations on structure.

2.5.2.2 Dynamic impact test validation

The experimental and numerical performance of hat structure under dynamic impact test is discussed here. The dynamic performance is evaluated by plotting a force vs time curve which gives the crush stiffness and peak crush resistance force for the studied impact. The force vs time plot of the three experimental trials is shown in Figure 2.26(a) where, the highlighted red arrows indicate the crush force at three locations i. e. at initial impactor contact, at maximum impactor stroke and when impactor finally losses contact with the hat structure. In Figure 2.26(b), front view of the three experimental trials is presented which shows the impactor position for the three corresponding locations. It is observed that a maximum stroke of 6.9 mm, 7.3 mm and 7.2 mm is obtained for the three trials (mean experiment maximum stroke = 7.1 mm). The experiments show a consistent and repeatable performance in terms of crush stiffness (linear slope), peak crush force and integral (area under the curve).

To validate the MTR pathway, the mean experimental performance is compared with the numerical response of the hat structure under dynamic impact test. A force vs time response plot is presented in Figure 2.27(a). A reasonable correlation is observed between the two curves, where the peak mean experimental force is 5.3 kN while peak numerical force is obtained as 4.5 kN. Further, the experimental damage occurred in the hat structure is compared with the numerical predictions in Figure 2.27(b). Encircled region shows the locations of the damage which is observed for both experiment and simulation. A Von-Mises stress contour plot is also presented in the Figure 2.27(b) at the maximum impactor stroke which shows the stress distribution is highest at the vicinity of impact. The maximum impactor stroke of 7.35 mm is obtained from the simulation which is very close to the mean experiment maximum stroke. Table 2.5 presents the peak force and integral value (area under the curve of the force time plot) for both experiment and numerical dynamic impact test. The integral value indicates the impactor kinetic energy absorbed by the hat structure during the test. It can be observed that mean experimental integral value is 1681 N-ms which is close to numerically predicted integral value of 1639 N-ms.

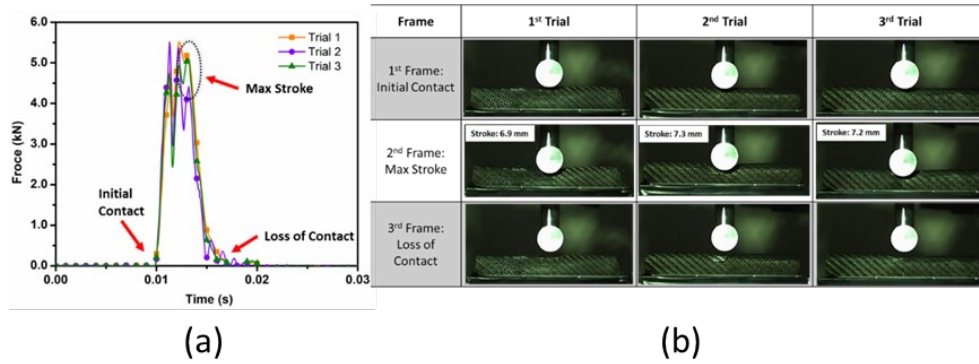


Figure 2.26: Dynamic impact test performance:(a) Force vs time plot showing three experimental trials and (b) front view of the experimental trials showing impactor position at initial contact, at maximum stroke and at loss of contact.

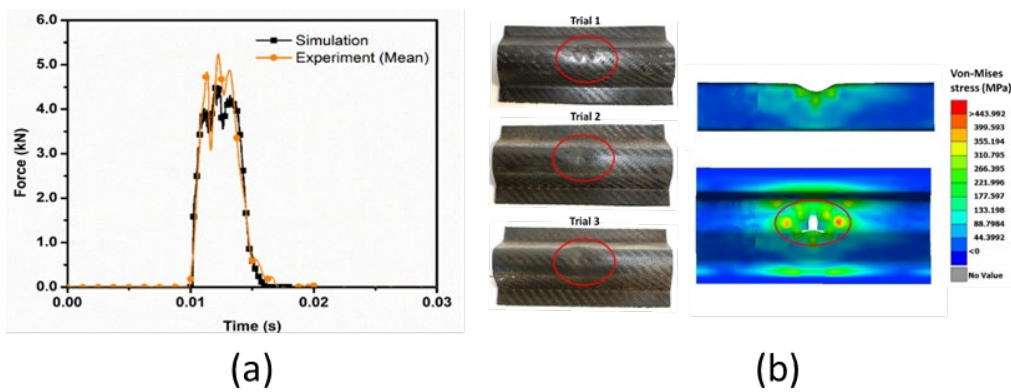


Figure 2.27: (a) Validation of dynamic impact test: Force vs time plot comparing experiment and simulation. (b) damage comparison of the experimental trials and numerical prediction.

Table 2.5: Dynamic impact test comparing experiment and numerical performance

Dynamic impact test	Peak Force (N)	Integral (N-ms)
Experiment trial 1	5515	1791
Experiment trial 2	5513	1593
Experiment trial 3	5107	1661
Mean (Standard deviation)	5378 (235)	1681 (100)
Numerical simulation	4545	1639

2.5.3 Numerical parametric study: manufacturing process effects on static and dynamic response

2.5.3.1 Thickness variation

In an ideal scenario, the hat structure has a uniform thickness of 2 mm with no variation (unmapped case). However, during processing stage several factors such as a non-uniform tool gap, depth-to-width ratio of the thermoforming tool and thermoplastic flow characteristics at high temperature may affect the final thickness distribution in the hat structure. Consequently, two cases are considered here, with 1% (T01) and 3% (T03) variation in thickness from the ideal thickness of 2 mm. The thickness distribution obtained from the MTR pathway is multiplied by a constant factor such that the difference between maximum to minimum thickness is 1% and 3% respectively for T01 and T03. The maximum thickness is kept constant as 2mm. The mechanical responses are determined under static and dynamic loading and results are compared with no thickness variation

(unmapped) case. The static responses for the six static load cases are presented in Table 2.6. It is seen that the static deflection increases with increase in thickness variation for all load cases. The thickness variation changes the material volume which affects the static stiffness.

Table 2.6: Static performance: effects of variation in thickness distribution

S No	Load Cases	Force (N)	Deflection (mm)			%Change	
			Unmapped	T01	T03	T01	T03
A	Longitudinal Compression	220	0.0027	0.0027	0.0028	1.06%	5.36%
B	Longitudinal Shear	220	1.6752	1.6982	1.7905	1.37%	6.88%
C	Longitudinal Bending	220	0.3356	0.3400	0.3581	1.33%	6.71%
D	Transverse Compression	304	1.7453	1.8011	2.0372	3.20%	16.73%
E	Transverse Shear	304	1.8988	1.9585	2.2107	3.14%	16.43%
F	Transverse Bending	304	9.7700	10.0841	11.4114	3.21%	16.80%

Next the impact performance is evaluated for the two thickness variations and the force-displacement curves of the impact load cases are shown in Figure 2.28. Note that the area under each curve gives the kinetic energy absorbed during the impact. It is shown that each curve forms a closed loop after reaching maximum displacement, which represents the rebound of the impactor from the hat structure. The curves attain a peak force value at approximately 2 mm displacement and then drops down as the displacement proceeds. To understand the force-displacement plot, the progressive deformation of hat structure from $t = 0$ to 10 ms is presented for both unmapped and T03 case in Figure 2.29. The red arrow

indicates the direction of impactor at the corresponding time. The impactor displacement is also mentioned for each time instant. Consider unmapped case of uniform thickness, as the deformation progresses from $t = 0$ ms to $t = 1$ ms, both the longer and shorter edges of the hat structure undergo compression during which the maximum peak force of 12 kN is attained. At this highest peak force point, compressive failure occurs along the bend region of the shorter edge. This results in flattening of the top of the hat structure and thereby increases the contact area between the impactor and hat. The failure is explained further in the next subsection. At $t = 2$ ms the impactor displacement is 6.17 mm and the impactor continues to push forward the hat structure over a larger contact area. At $t = 4$ ms the impactor displacement is 9.61 mm, the part of the structure corresponding to the longer edge undergoes a snap-through to reach another stable configuration as shown in the Figure 2.29, resulting in reduced contact area. At $t = 6$ ms, the impactor continues to push further the shorter edge of hat structure over a smaller contact area till all the impactor energy is absorbed.

The maximum impactor displacement of 11.44 mm is reached for the unmapped case at $t = 6.6$ ms beyond which the impactor rebounds due to the spring back effect. This effect can also be observed in the force vs displacement plot in Figure 2.28, where force increases to a higher value before rebound. At $t = 8$ ms, the impactor direction is reversed, and the net impactor displacement reduces to 11.01 mm. At the termination time, $t = 10$ ms the net impactor displacement reduces to 9.77 mm. Since, the thickness variation results in material volume change which is directly related to the material stiffness and strength and therefore a slight variation may affect the response significantly. It is observed as the

thickness variation is increased (the average thickness is reduced), the initial slope of the curve which represents the initial crush stiffness reduces. Further the compressive failure in the shorter edge occurs earlier than the unmapped case resulting in the drop in the peak force to 11.7 kN and 11.3 kN for T01 and T03, respectively. On comparing the progressive deformation of unmapped and T03 cases in Figure 2.29 it can be observed that at any given time $t < 6$ ms, the impactor displacement is higher for T03 than unmapped case due to overall reduced strength of the structure and early failure. At $t = 6$ ms, a higher snap through effect can be observed for T03 and the maximum impactor displacement of 12.05 mm is obtained at $t = 6.4$ ms. Due to this larger impactor displacement or larger pushing of the hat structure, a higher spring back force is affected. It can also be observed in the force vs displacement plot in Figure 2.28, that T03 reaches a larger peak of 6.5 kN before rebound as compared to unmapped case where force reaches a maximum of 3.5 kN before rebound. As a result, at $t = 10$ ms, the net impactor displacement is 9.57 mm, which is lower than the unmapped case.

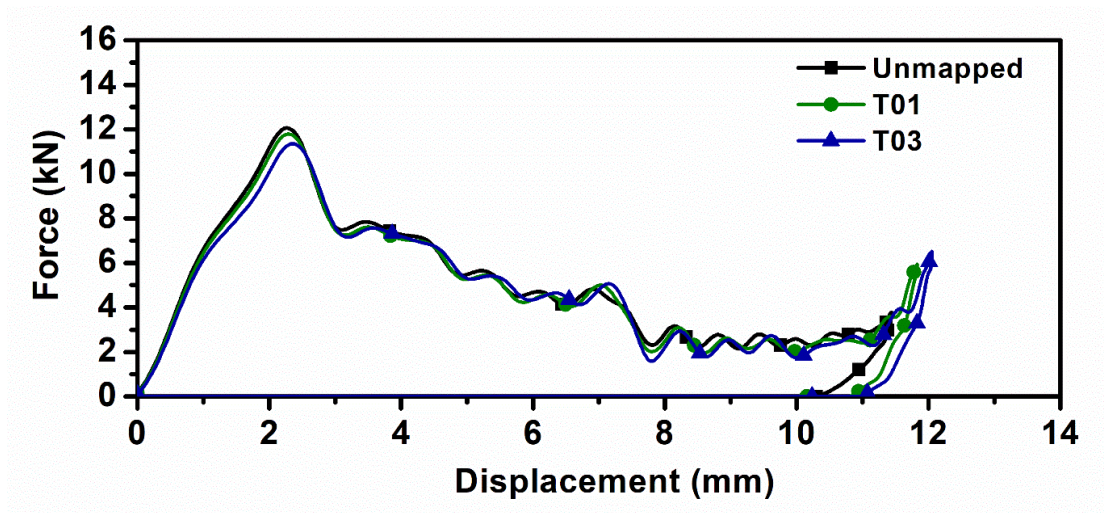


Figure 2.28: Force vs displacement plot under impact loading comparing two cases of thickness variation with unmapped case.

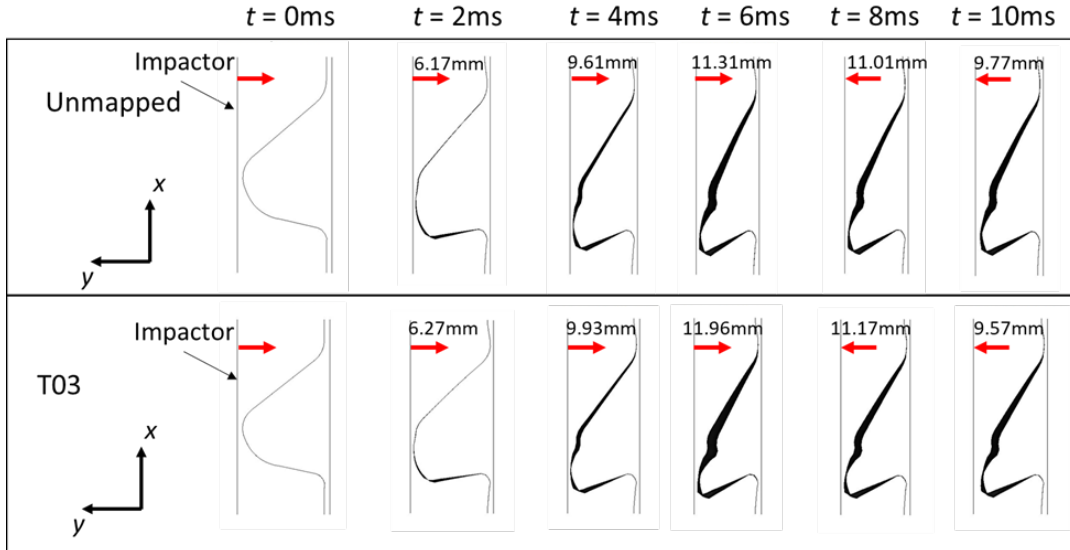


Figure 2.29: Progressive deformation of hat structure under impact loading showing the effect of thickness variation.

2.5.3.2 Fiber orientations variation

Thermoforming a component with complex geometry can lead to large variation in fiber orientation over the formed component. For the numerical analysis in this section, two different fiber orientation variations are generated and compared with original 0/90 configuration (unmapped case). This is done by multiplying the shear angles obtained from the actual thermoforming result of the hat structure by a constant factor. The two cases are D20 with a maximum shear angle of 20° and D35 with a maximum shear angle of 35° . The fiber orientation distributions for the three cases are shown in Figure 2.30.

The numerical tests are carried out first for the six static load cases and the responses are presented in Table 2.7 and a comparison is made with unmapped configuration. With

increase in shear angle, the stiffness under longitudinal compression, transverse compression and bending is largely improved. The static performance under longitudinal shear and bending loads is reverse for the two cases D20 and D35. The longitudinal bending stiffness is increased as shear angle is increased from 0° to 20° by almost 20% and then reduces as shear angle is further increased to 35° . This is mainly due to the nonsymmetrical cross-section of the hat structure which results in a higher cumulative nodal force distribution on the longer side. Due to this a pure bending or shear test is not simulated, and instead additional twist is added to the structure, thereby changing the line of action of resultant force. The configuration with fibers orientated along the line of action would give maximum stiffness, which here is observed for D20 case. To further confirm the observation, more fiber orientation variations between 0° and 40° are simulated. It is found that there is an optimal fiber orientation configuration which gives the maximum stiffness in the longitudinal bending case (results are not presented here). A similar result is obtained for the longitudinal bending test case.

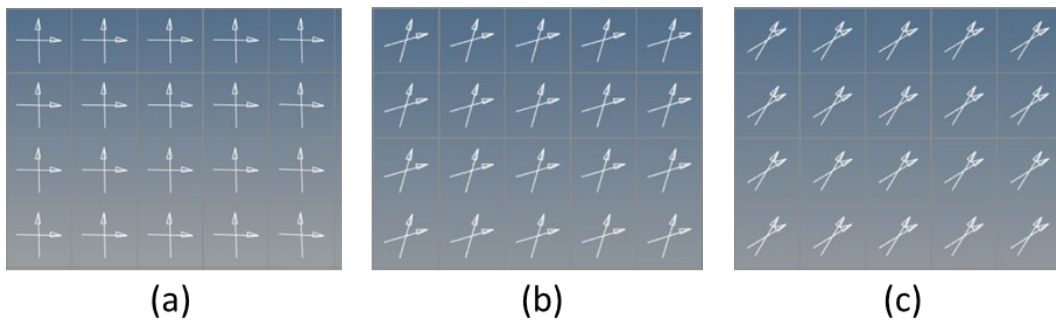


Figure 2.30: Fiber orientations for the three cases (a) unmapped, (b) D20 and (c) D35.

Table 2.7: Static performance for the two orientation variants

S No	Load Cases	Force (N)	Deflection			%Change	
			Unmapped	D20	D35	D20	D35
A	Longitudinal Compression	220	0.0027	0.0031	0.0059	14.3%	118.3%
B	Longitudinal Shear	220	1.6752	1.5796	2.0472	-5.7%	22.2%
C	Longitudinal Bending	220	0.3356	0.2703	0.4158	-19.5%	23.9%
D	Transverse Compression	304	1.7453	1.9869	2.7002	13.8%	54.7%
E	Transverse Shear	304	1.8988	1.5629	1.4130	-17.7%	-25.6%
F	Transverse Bending	304	9.7700	11.2838	15.4205	15.5%	57.8%

Next, the effect of fiber orientation variation is evaluated. The force displacement results for all three cases are plotted in Figure 2.31. It is found that the initial stiffness of unmapped case is higher than the D20 and D35 cases, whereas the peak force is maximum for D35 case as 14.9 kN while for D20 it is 12.2 kN, slightly higher than unmapped case. To understand the initial impact response, the progressive deformation of hat structure for the unmapped and D35 cases is presented in Figure 2.32 or the simulation time from $t = 0$ to 1 ms. From the simulation time $t = 0$ to 0.5 ms, as the impactor pushes the hat structure over a small contact area, the flanges of hat structure rests on the fixed support. A localized deformation occurs in the vicinity of impactor contact, where the impactor flattens the curved hat top profile, increasing the contact area. To explain the effect of fiber orientation during this initial local contact, the fiber tow and loading direction is plotted for unmapped and D35 configuration in Figure 2.33(a). The red lines represent the directions of in-plane

loading. Since for the unmapped configuration, the direction of loading is aligned along the two fiber tows direction, therefore a higher resultant stiffness is observed. On the contrary, for the D35 configuration, the loading direction is not aligned towards the fiber tows and therefore lower stiffness is observed. .

Now, as the impactor pushes further, both sides of the hat structure undergo compression. Due to the non-symmetrical structure the shorter side (also steeper) experiences larger compressive force than the longer side. The line of action of these compressive forces are now along the vertical direction of the shorter side. In other words, the direction of loading is at an angle approximately 45-degree to the tow direction as shown in Figure 2.33(b). The resultant compressive strength along the direction of loading is much higher for D35 as compared to unmapped. As a result, for the unmapped case at $t = 1$ ms, compressive failure occurs at the bend of the shorter edge (see encircled region for unmapped case in Figure 2.32) and a lower peak force is reached. However, for the D35 case, shorter edge is more resistant to failure as both fiber tows are along the line of action. Therefore, as the impactor pushes further, the longer edge undergoes out of plane bending (as encircled region for D35 case in Figure 2.32) while absorbing more energy and thereby, higher peak force. This explains the difference between peak forces for the two cases in the Figure 2.31. The von-mises stress contour plot (top view of hat structure) is also presented at $t = 1$ ms comparing both unmapped and D35 cases. It can be observed that a significantly higher stresses are present along the longer edge for D35 case as compared to unmapped case where early compressive failure is observed along the shorter edge. Further, the progressive deformation plot for the total simulation time, $t = 10$ ms is

presented in Figure 2.34. As the deformation progresses after $t > 2$ ms, the impact occurs over a much larger contact area for D35 than unmapped case. This results in much quicker energy absorption for the D35 case wherein, the maximum impactor displacement reaches 7 mm at $t = 3.3$ ms and beyond which rebound occurs. Towards the end of simulation, the net impactor displacement for D35 is 0.38 mm while for unmapped it is 9.77 mm. This shows that both static and dynamic performance is highly sensitive to fiber orientations since the material strength and modulus are directly dependent on them.

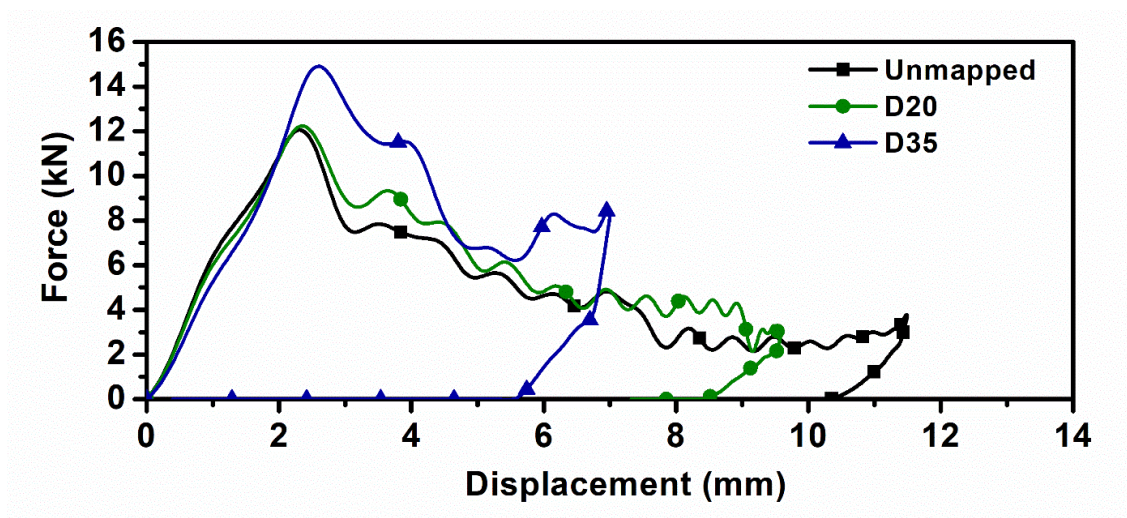


Figure 2.31: Force vs displacement plot comparing impact performance for the two fiber orientation cases

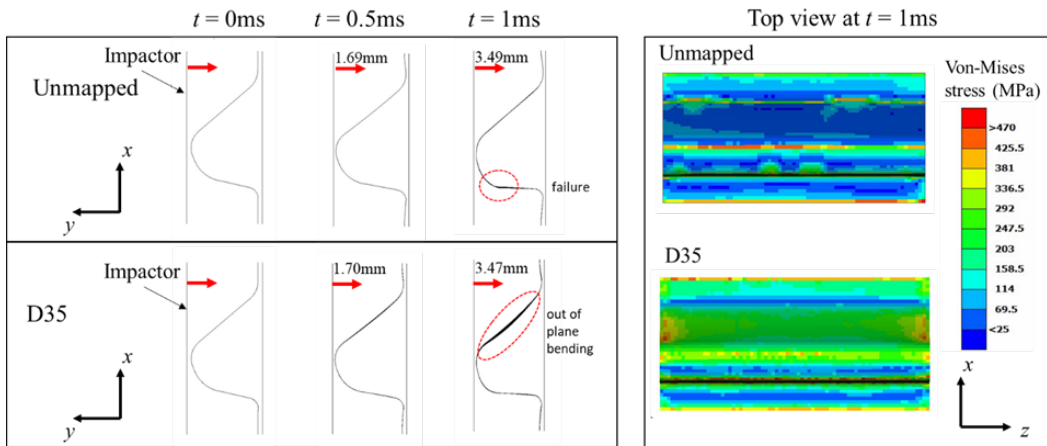


Figure 2.32: Unmapped vs D35: initial deformation of hat structure under impact loading and von-mises contour plot at time $t = 1$ ms.

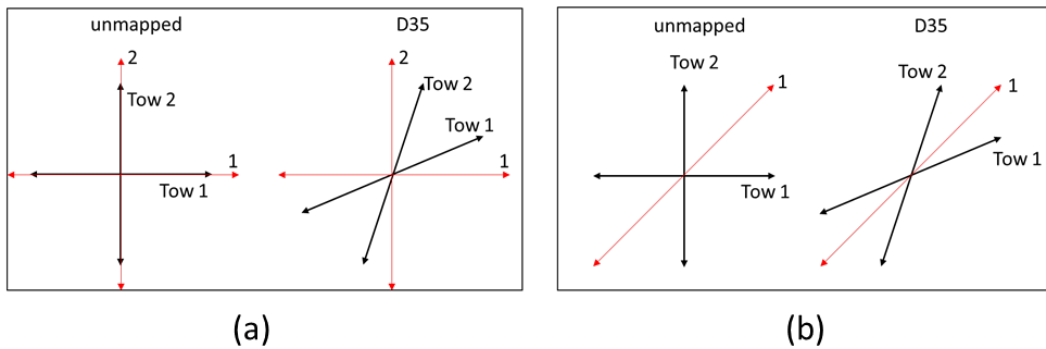


Figure 2.33: Free body diagram showing the fiber tows direction and respective loading direction during (a) initial impact on top of the hat and (b) impact before compressive failure along the shorter edge of the hat.

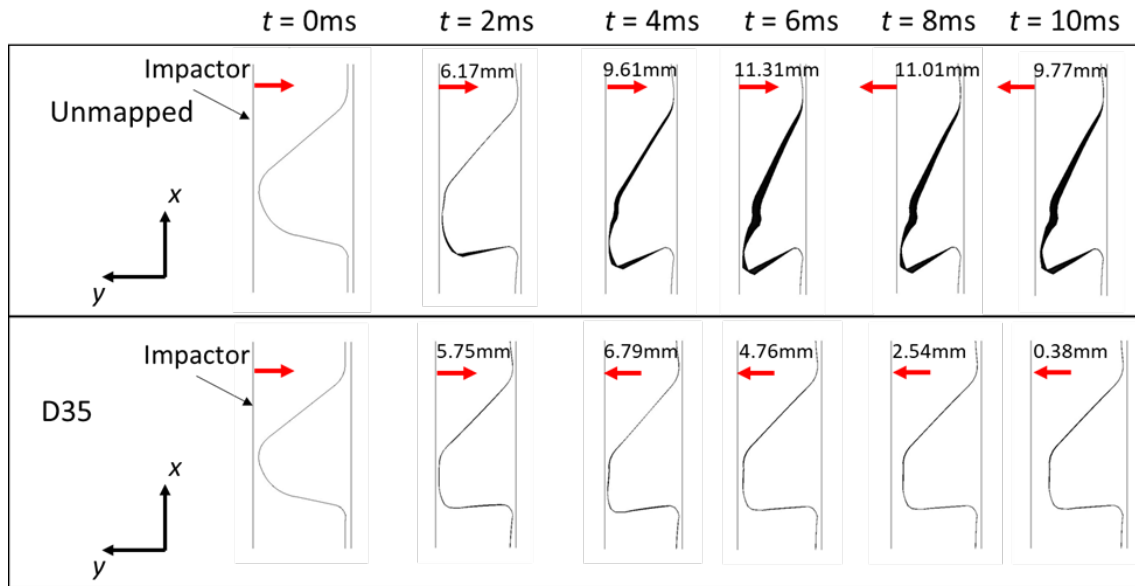


Figure 2.34: Unmapped vs D35: progressive deformation of hat structure under impact loading.

2.5.3.3 Cooling rate variation

While large-scale production of thermoformed composite structure requires faster cooling cycles, higher cooling rates can induce undesirable residual stresses as discussed earlier. The effects of change in cooling rate on static and dynamic performance are discussed here. For comparison, residual stresses are calculated for two cooling rates $5\text{ }^{\circ}\text{C/s}$ (case CR5) and $50\text{ }^{\circ}\text{C/s}$ (case CR50) applied to both punch and die. These stresses are then mapped to a new mesh of the hat structure for evaluation of the static and impact performance. The average von-Mises stress contour plot on hat structure is presented in Figure 2.35. A maximum stress of 21 MPa is obtained for CR5 and 26 MPa for CR50. The results for three cases are compared to the case without cooling rate effect (unmapped case). The static results are presented in Table 2.8 showing the deflection of the hat

structure in the six static load cases for various cooling rates. It is observed that there is no significant change in stiffness for longitudinal bending, transverse shear and transverse bending load cases. The longitudinal compression stiffness however significantly reduced as the cooling rate is increased from 0.5 to 50 °C/s. This can be understood by fact that the hat structure is already pre-stressed along the longitudinal direction with compressive residual stresses and since the direction of loading is in the same compressive direction therefore higher deflection (or lower stiffness) is observed. Further, the stiffness under longitudinal shear and transverse compression loads slightly increases as the cooling rate is increased.

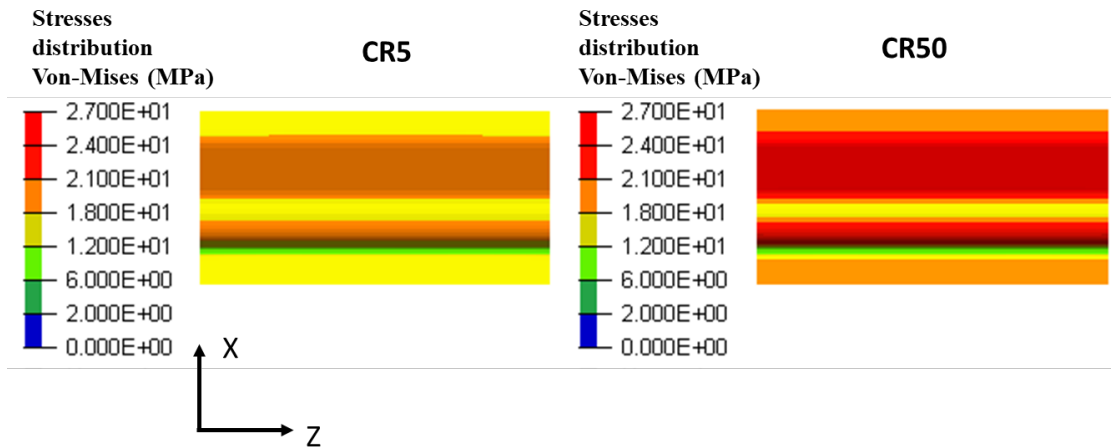


Figure 2.35: Von Mises residual stresses contour plot for the two cooling rate cases.

Table 2.8: Static performance at different cooling rates

S No	Load Cases	Force (N)	Deflection			% Change	
			Unmapped	CR5	CR50	CR5	CR50
A	Longitudinal Compression	220	0.0026	0.0030	0.0026	3.7%	13.1%
B	Longitudinal Shear	220	1.6739	1.6597	1.6739	-0.7%	-0.9%
C	Longitudinal Bending	220	0.3356	0.3355	0.3356	0.1%	0.0%
D	Transverse Compression	304	1.7408	1.7302	1.7408	-0.8%	-0.9%
E	Transverse Shear	304	1.8988	1.8992	1.8988	0.0%	0.0%
F	Transverse Bending	304	9.7704	9.7725	9.7704	0.0%	0.0%

Next, the impact performance is evaluated and the force-displacement plot for various cooling rate cases is presented in Figure 2.36. It is observed that the initial stiffness is similar for all the cases however peak force drops with higher cooling rate. As described earlier, both the longer and shorter edges of the hat structure undergo compression during $t = 0$ to 2 ms and compressive failure occurs at shorter edge for the unmapped case at $t = 1$ ms. With the introduction of compressive residual stresses in the hat structure for CR50 case, this compressive failure in the short edge is reached slightly earlier at $t < 1$ ms, resulting in lower peak force than the unmapped case. To illustrate further, the deformation of the hat structure as a function of time is examined for the unmapped and CR50 cases in Figure 2.37 for the simulation time $t = 0$ to 10 ms. At $t = 2$ ms, the impactor displacement

is little higher in CR50 case due to early failure. With time $t = 2$ ms to 6 ms, the impactor pushes and deforms the hat structure more for the CR50 case and a higher impactor displacement is observed in a shorter time as compared to unmapped case. The maximum impactor displacement of 12.02 mm is reached at 6.3ms for CR50 while it is 11.4 mm at $t = 6.7$ ms for the unmapped case as mentioned previously. At this point the kinetic energy of the impactor is absorbed completely and the spring back effect of hat structure follows, and a larger rebound is observed for CR50.

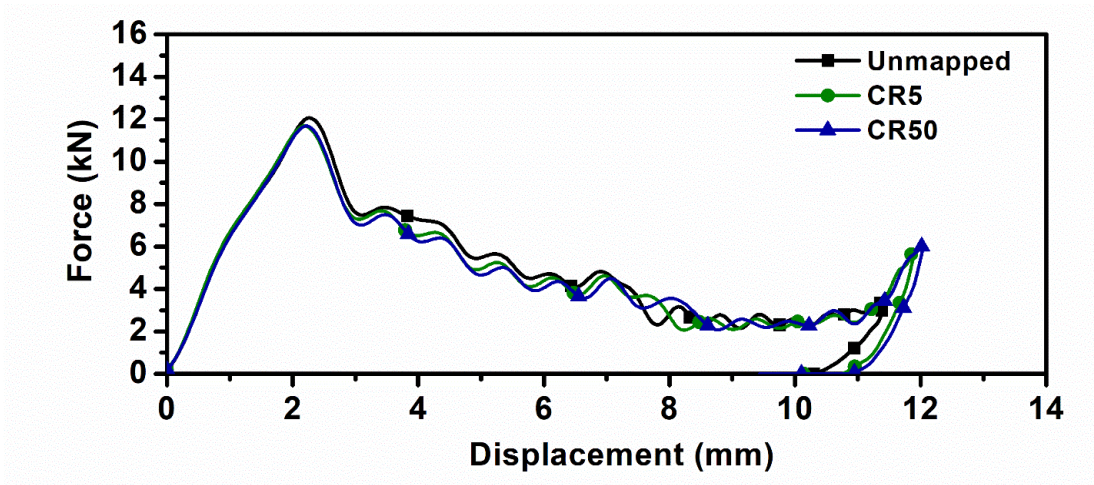


Figure 2.36: Force vs displacement plot showing impact performance for various cooling rate cases.

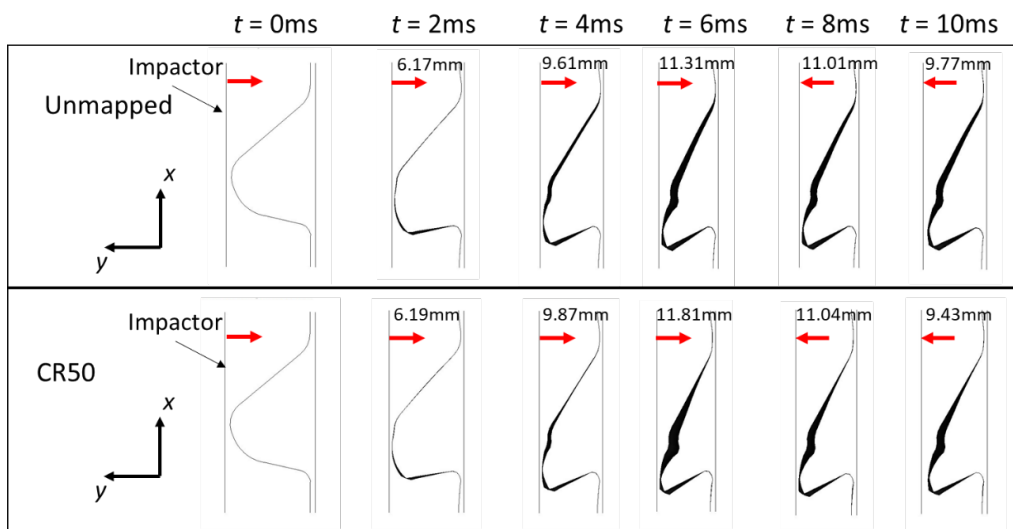


Figure 2.37: Progressive deformation of hat structure under impact loading showing the effect of cooling rate.

2.6 Conclusion

The MTR pathway is established in this study for a carbon fiber reinforced thermoplastic composite hat structure. The pathway consists of six steps: (a) material

characterization and modeling, (b) thermoforming simulation with experimental validation, (c) cooling simulation, (d) residual stresses determination, (e) mapping of thermoforming effects such as fiber orientations, thickness variations and residual stresses and (f) mechanical performance evaluation. The pathway meets the critical requirements of integrating the design and manufacturing of lightweight thermoplastic composite parts by directly linking the manufacturing process effects to the mechanical responses. The thermoforming simulations and mechanical performance are experimentally validated by first fabricating a 1.97 mm thick composite hat structure using thermoforming process and then performing a 3-point bend test. Appropriate apparatus is developed for holding the blank in place during forming and cooling the closed mold post forming ensuring repeatability and reliability. The change in fiber orientations and thickness distribution is compared and numerical results were found to be consistent with experimental observations. To validate the residual stresses owing to rapid cooling rate, a 3-point bend test is simulated under quasi-static loading conditions and compared with experiments. The initial stiffness and peak crush force are consistent for both studies.

Further, the effects of the large variations in the thermoforming process induced factors such as residual stresses, change in fiber orientations and thickness distribution are studied numerically. The static and dynamic performance is evaluated for different cases which are summarized as:

(a) The change in thickness distribution may result in significant reduction in static stiffness of the structure. The largest variation is observed under transverse compression load where

16% reduction is observed for T03 case. The impact performance also varies with thickness variation and primarily affects the dynamic stiffness and strength of the structure.

(b) The two cases of fiber orientations with large shear angle variations are studied which showed significantly higher variations in the static and dynamic performance. The largest variation is observed for longitudinal compression at maximum shear angle of 35° . It is also observed that under mixed loading conditions there is an optimal fiber orientation configuration that could give the maximum structural stiffness. The high shear angles D20 and D35 showed 18-36% increased dynamic stiffness under the studied impact load case with a much larger rebound effect.

(c) The effect of cooling rate is observed by determining the residual stresses at two different cooling rates 5 and 50 °C/s. These stresses are then included in the mechanical performance evaluation. Under the static loading largely, no significant change in stiffness of the structure is observed with change in cooling rate, except, the longitudinal stiffness which is reduced significantly upon increase in cooling rate. The dynamic performance under study deteriorated for the high cooling rate cases as early compressive failure is observed due to induced compressive stresses.

CHAPTER 3 : MTR PATHWAY FOR OUT-OF-AUTOCLAVE MOLDED THERMOSET COMPOSITE BOOM STRUCTURE

3.1 Introduction to Composite Boom structures

Composite boom structures are being developed for application in solar sail system used for small Satellite missions. Solar sails are high-reflecting materials used as a means to propel spacecrafts. This propulsion is caused by radiation pressure exerted by sunlight on their mirror-like surface. The material used for such a solar sail is very thin and requires support structures. The use of thin-ply based composite booms as support structures for solar sails is a recent development [77]. Their adoption was driven by the light-weighting capabilities of CFRP structures over conventional metals. In satellite application, coils of these rolled booms (Figure 3.1(b)) along with compactly packed solar sail are stowed in the satellite equipment. Deployment mechanisms are employed in order to uncoil the booms along with the solar sail once the satellite is in orbit. The composite booms are typically 2 - 9 m in length [78]. Figure 3.1(a) shows the solar sail with the composite booms along diagonals. The booms can have different cross-sections, for example omega-shaped, shearless or triangular (see Figure 3.1(c)). In the present study, the omega-shaped boom is considered for composite boom tool development.

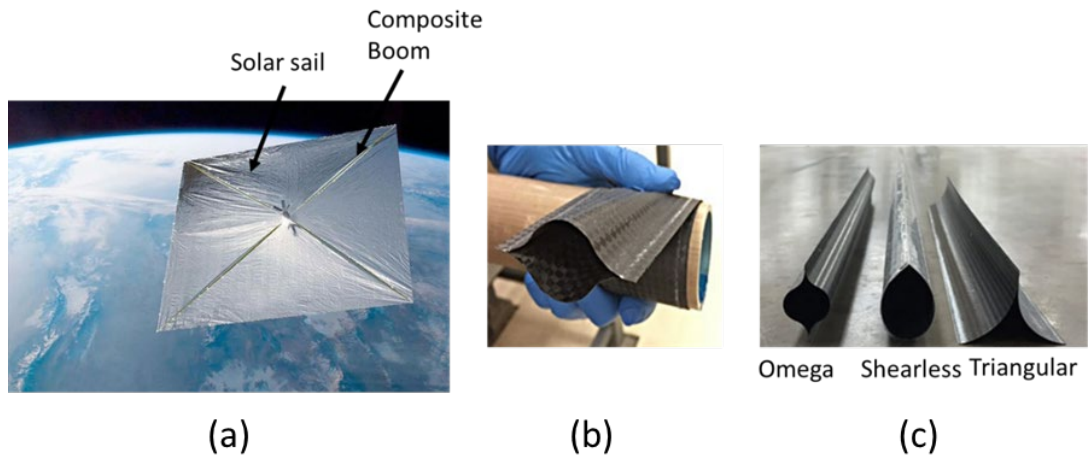


Figure 3.1: (a) Solar sail supported with composite booms along diagonals, (b) Rolled coil of composite boom structure, and (c) different cross sections of booms [77]

3.1.1. Self-heated Composite Boom Tool

Traditionally, autoclave technique was used to cure thermoset based CFRP composite sheets [79]. Autoclave is a pressure vessel used to process composite materials requiring exposure to temperature and pressure. The temperature required for curing the composite sheet is maintained in the autoclave and vacuum pressure is applied through vacuum bagging. The size of composite structures cured by this technique is however limited by the overall capacity of the autoclave. Manufacturing of the composite boom structures requires very long tools (upto 7 m in length). As a result, the autoclave technology is not suitable for the current application. In order to form and cure the composite boom structures, a novel out-of-autoclave technology was proposed by Touchstone Research Laboratory, Ltd. This technology makes use of self-heated tool with heater elements embedded within in to process thermoset based composites. Touchstone Research Laboratory in collaboration with Clemson University, is currently working on a

project for developing such a self-heated tool to cure thin-ply composite booms for application in solar sail systems [77]. This project is funded by National Aeronautics and Space Administration (NASA).

The tool was conceptualized to be built primarily using CFOAM® carbon foam material developed at Touchstone. CFOAM is a unique fire resistant, light-weight, impact absorbing material made out of coal. CFOAM® is especially suitable for making molds to form and cure CFRPs. This is because its thermal expansion and contraction properties are very similar to that of carbon fiber composites. The current project targets include design, development and prototyping of a self-heated tool capable of curing thin-ply (< 0.06 mm thick) CFRP composites to form approximately 7 m long composite booms. Accordingly, a tool design consisting of two female CFOAM molds and a male silicone plug was investigated. A forming and curing process strategy for the thin-ply composites with the self-heated tool was outlined and described here. Figure 3.2(b) shows the upper and lower female tools and the silicone plug assembly. The composite boom structure consists of upper and lower halves made of two thin-ply composite sheets adhesively bonded together at the ends. The two female molds will be fixed together using pins and bolts (see Figure 3.2(a)) and the male plug will be inserted in between such that the two composite sheets are sandwich between the tools and the plug. The self-heating female tools will be brought to the curing temperature of the composite sheet. The entire assembly will be vacuum bagged and vacuum pressure will be applied to the boom halves as shown in Figure 3.3(a). In this manner, the required temperature and pressure will be applied to form and cure the

composite boom structure. The molds will be then cooled down once curing process is completed. A typical curing cycle is shown in Figure 3.3(b).

Based on the process outline, a few candidate materials were selected, and their performance was evaluated. The general construction of the composite boom tool consists of a core, heat spreader, tool surface and heaters. Two core materials namely CFOAM and GFOAM (Graphitized CFOAM) which has higher thermal conductivity were investigated. The tool surface is a laminated composite facesheet consisting of 12 layers of carbon fiber reinforced BMI (Bismaleimide) matrix. The heat spreader is a graphite based material called SS400 and has very high in-plane thermal conductivity. The heater materials considered were namely Silicone, Mica or Polyimide. The material cured on the tool are thin-ply carbon fiber reinforced epoxy (epoxy based CFRP) sheets/laminates. The tool materials are shown in Figure 3.4. In order to form and cure the thin-ply composite sheets successfully, three research questions needed to be answered. First, how to achieve temperature uniformity on the upper tool surface in contact with the composite sheet? The temperature uniformity on the tool surface is vital to achieve uniform curing of the composite sheet. Second, what core material should be used in the construction of the tool? The choice between poor heat conducting CFOAM and high heat conducting GFOAM is critical for tool performance. Third, what should be the location(s) of the heater(s) in the tool? To answer these questions, the tool design should be tied to the curing simulation. Further, the curing process produces undesirable effects such as thickness variations, fiber reorientations and residual stresses. These process effects might warp the thin-ply composite which would in turn affect its structural performance. As mentioned in section

3.1, these composite booms are coiled to form a tape and stowed compactly in the solar-sail equipment. Excessive warpage in the composite boom would severely limit its torsional properties. In order to study the design and manufacturing effects on the structural performance, a Manufacturing-to-Response was established and implemented for the composite boom structure.

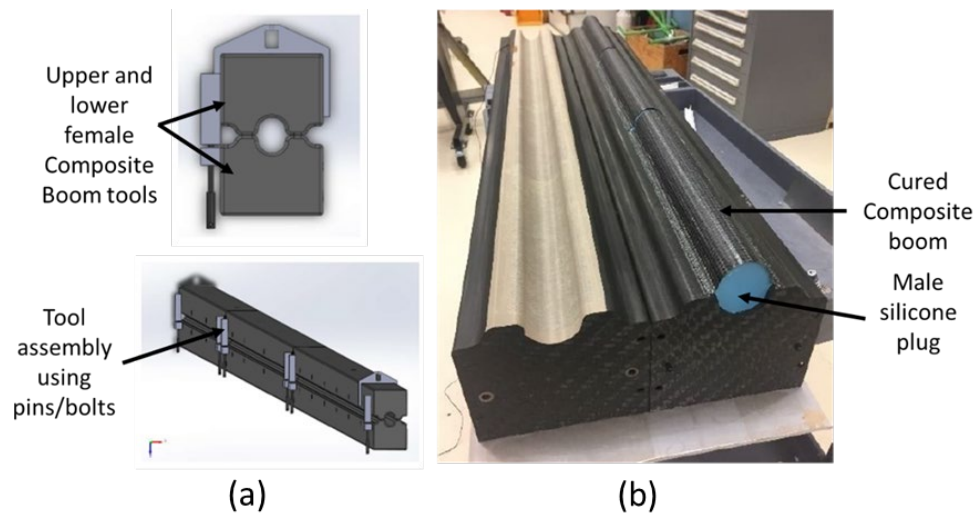


Figure 3.2: (a) Rigid female composite boom upper and lower tools used to form the Composite Boom structure, b) cured composite boom with male silicone plug inserted between the boom halves [77]

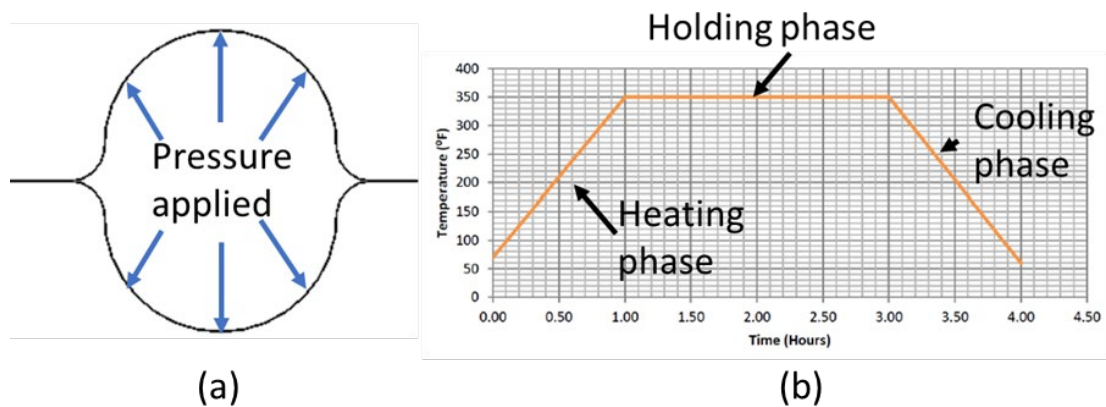


Figure 3.3: a) Pressure applied to the inside walls of the composite boom structure by the silicone plug, b) a typical cure profile for CFRP composites,

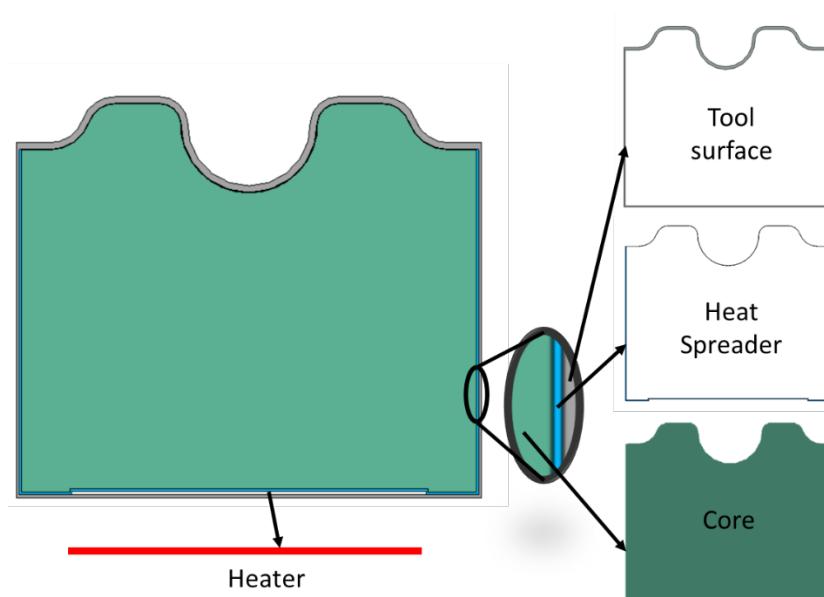


Figure 3.4: Composite Boom Self-heating Tool showing its materials and general construction

3.2 Manufacturing-to-Response Pathway

Figure 3.5 shows the framework of the MTR pathway which consists primarily of five process steps as follows: 1) Composite Boom Tool design by performing heat transfer analysis. 2) material characterization at coupon level and material card (MAT

card) generation for heat transfer and curing simulation, 3) curing analysis of the thermoset based carbon fiber composite, 4) mapping of process induced effects and 5) mechanical performance evaluation and experimental validation at structural level. The detailed steps of the MTR pathway are described here.

In the scope of the present study, analysis methods were employed to evaluate the first two steps of the pathway. In the first step, transient heat transfer analysis was performed for selection of tool materials and optimal thermal performance. The second step of the pathway was the curing simulation comprising of thermo-chemical analysis, flow-compact analysis and the stress mechanical analysis. The curing simulations were performed using the optimized tool design. The material properties of tool materials were obtained from Touchstone Research Laboratory. These properties were used to generate material cards for performing numerical simulations such as transient heat transfer analysis and curing simulation.

The last two steps will be conducted as a part of future work. In the fourth step, the predicted residual stresses, warpage and fiber distributions/orientations will be incorporated into the static and dynamic FE setup in ABAQUS and LS-DYNA, by using a mapping procedure. The last step, Step five of the MTR pathway will involve numerical evaluation of the mechanical response under the static and dynamic loading conditions which will be validated by experimental tests.

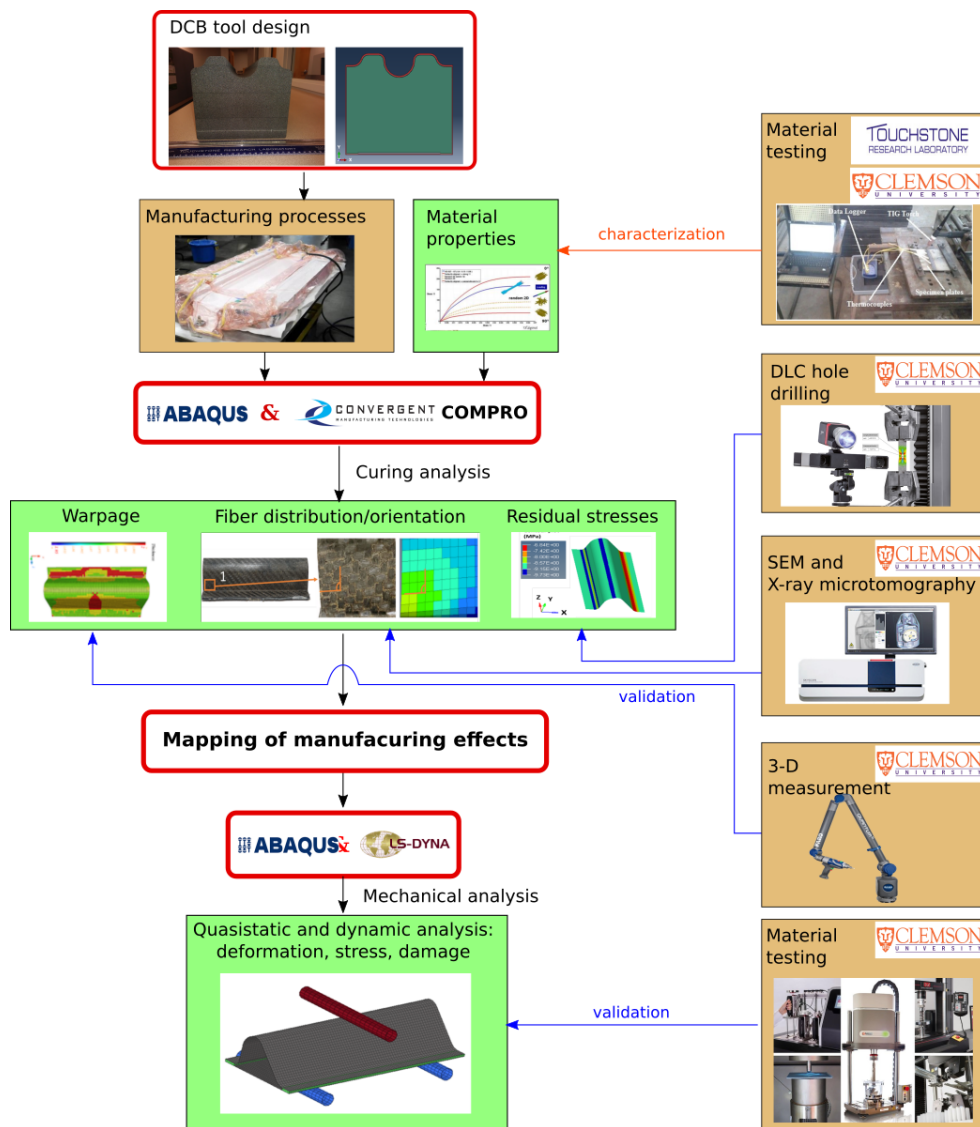


Figure 3.5: MTR pathway for thermoset based CFRP composite structures

3.3 Modeling Pathway

3.3.1 Heat transfer analysis

First step of the modeling pathway is heat transfer analysis for Composite Boom tool design. Computational models are developed for the Composite boom tool in order to study the heat transfer characteristics. The model setup of the Composite Boom tool is

described here. Primarily, three material properties were required for the transient heat transfer analysis namely mass density (g/cm^3), specific heat ($J/g \text{ } ^\circ C$) and thermal conductivity (W/mK). The properties for Carbon Foam (CFOAM), Graphitized CFOAM (GFOAM) and CFOAM with BMI laminate facesheet were obtained from Netzsch Instruments test lab. Fiber reinforced BMI laminate properties were determined based on rule of mixtures from the properties obtained from Netzsch. Graphite and graphite based heat spreader (SS400) properties were gained from technical datasheets as mentioned in Table 3.1. The governing equation for heat transfer inside an object derived from energy conservation and Fourier's law is as [80], [81]

$$\frac{\partial}{\partial x} \left(k_x \frac{\partial T}{\partial x} \right) + \frac{\partial}{\partial y} \left(k_y \frac{\partial T}{\partial y} \right) + \frac{\partial}{\partial z} \left(k_z \frac{\partial T}{\partial z} \right) - \rho c \frac{\partial T}{\partial t} + \dot{q} = 0 \quad (3.1)$$

Where k_x, k_y and k_z [$W \cdot m^{-1} \cdot K^{-1}$] are the thermal conductivity coefficients along the x, y and z-axes of the object, $\frac{\partial T}{\partial x}, \frac{\partial T}{\partial y}$ and $\frac{\partial T}{\partial z}$ [$K \cdot m^{-1}$] are the temperature gradients along x, y and z-axes respectively, ρ [$kg \cdot m^{-3}$] is the mass density and c [$J \cdot K^{-1} \cdot kg^{-1}$] is the specific heat of the object material, $\frac{\partial T}{\partial t}$ [$K \cdot s^{-1}$] is the rate of change of temperature with respect to time, \dot{q} [$J \cdot m^{-3} \cdot s^{-1}$] is the rate of heat generated per unit volume from an internal heat source.

Equation (3.1) is the heat conduction governing equation inside an object. However, heat transfer takes place on the surfaces of the object through convection or radiation. In the present problem, convection boundary condition also known as Newton Boundary condition was used. This boundary condition assumes that the heat conduction

at a surface is equal to the heat convection at the surface in the same direction (see Figure 3.6). This boundary condition is represented as

$$-k \frac{dT(0, t)}{dx} = h[T_{\infty,1} - T(0, t)] \quad (3.2)$$

where, dT/dx [$K \cdot m^{-1}$] is the temperature gradient at the surface, h [$W \cdot m^{-2} \cdot K$] is the convective heat transfer coefficient of the surrounding medium, $T_{\infty,1}$ [K] is the temperature of the surrounding medium and $T(0, t)$ [K] is the temperature at the surface.

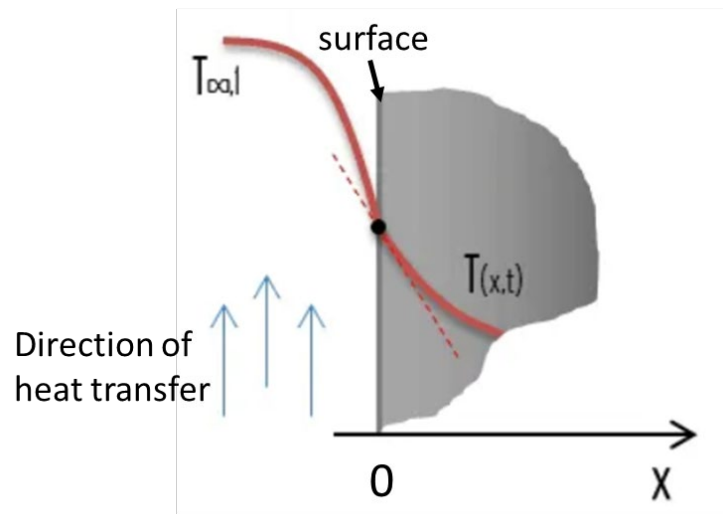


Figure 3.6: Illustration of convection boundary condition in a heat transfer problem

3.3.1.1 Composite Boom Tool Model setup

The problem involves analyzing the thermal behavior of a long (23 feet) Composite Boom tool. The Composite Boom tool has a uniform cross-section in its longitudinal direction and its size in the transverse directions is much less than its length. In the present study, it is assumed that the heater(s) are of rectangular shape and will run the entire length of the tool. Therefore, the 3D problem was reduced to a 2D problem neglecting the

temperature gradient at the two ends. The 2D Finite element model was setup using *AbaqusTM* as shown in Figure 3.7. The configuration of the tool consists of a core (CFOAM/GFOAM) enveloped by heat spreader and a layer of BMI laminate. The core, heat spreader and BMI laminate are modeled as 2D deformable shell parts. Solid homogeneous sections and material properties (refer Table 3.1) are assigned to each of these three parts. The heat spreader (SS400) material has high in-plane thermal conductivity as compared to through-thickness direction. As a result, an orthotropic material property is assigned to SS400. Accordingly, a local material orientation (1,2) is defined for the SS400 section where the 1-axis is along the in-plane direction and 2-axis is along the through-thickness direction. The heater location in the tool is highlighted with red edges in Figure 3.7. The heater is not modeled as a separate part. Instead, the red edges associated with heater location are assigned a uniform temperature boundary condition. The magnitude of the temperature boundary condition is defined equal to the maximum temperature output of the heater element. For example, for Silicon heater element, maximum temperature output is 450F.

Surface-to-surface interfaces are defined for the core-heat spreader and heat spreader-BMI laminate contact pairs. A thermal gap conductance of $2.63 \text{ W/cm}^2\text{°C}$ is defined for each of the two interfaces. An initial temperature of 25°C was defined for all three parts. Convection boundary condition with a coefficient of $1.5 \text{ W/m}^2\text{K}$ was defined to model heat loss to the surrounding air. The boundary condition was defined for all the exterior edges of the tool exposed to air. 2D heat transfer elements (DC2D4) were used for the analysis with fine mesh size of 1 mm. The individual parts were partitioned suitably in

order to create a uniform mesh. Refer to Appendix B Table B-2 for detailed steps of the model setup in *Abaqus*TM [82]. Transient heat transfer analysis was performed with this model setup. Such a transient analysis was necessary to study the temperature evolution in the different materials of the tool as a function of time.

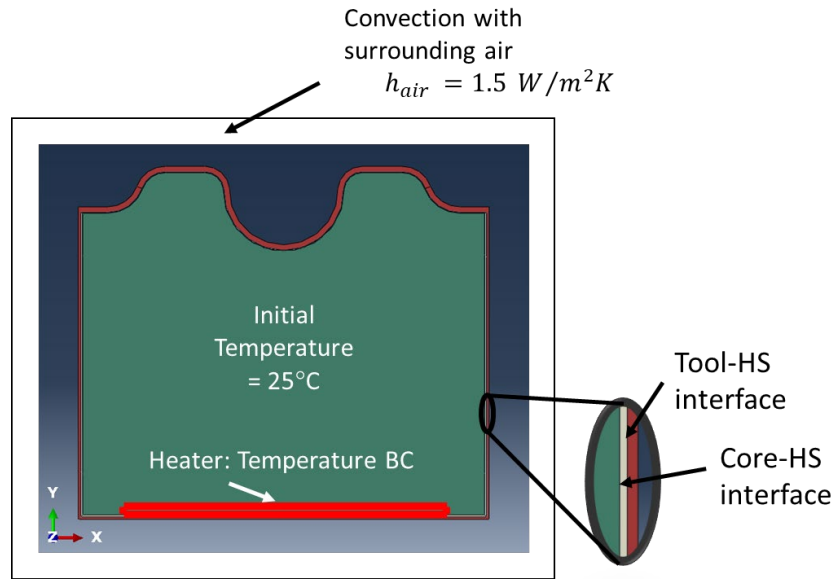


Figure 3.7: Cross-section of Composite Boom tool showing the model setup. HS refers to Heat Spreader

As described in Section 3.1.1, a few candidate materials are considered for the composite boom tool construction. The choice and combination of these materials will have an influence on the heat transfer characteristics. Also, multiple heaters will allow quick heating of the tool. Location of heaters is also an important consideration. Essentially, the parameters that influence the thermal behavior of the tool need to be identified. Subsequently, a sufficient number of design concepts that thoroughly study the influence of each identified parameter need to be modeled and analyzed. For that purpose, a Design

of Experiment (DOE) method was executed. However before analyzing the tool designs, model validation was performed using flat plate thermal profile data from experiments. The model setup for the flat plate heat transfer analysis is described in the next section.

3.3.1.2 Model validation: Experimental method and Computational models for Flat Plate cases

Flat plate samples were used to perform thermal profiling of aforementioned tool materials. The materials assembled for the flat plate samples were representative of the composite boom tool. In each case, a heater was bonded on one side of the plate which is referred to as the hot side. A thermocouple was mounted on the heater to record the temperature profile on the hot side. The side opposite to the heater is referred to as the cold side. Seven thermocouples each 1” apart were mounted along the cold side to capture the thermal profiles along the length of the plate. The heater material was ramped up to a definite temperature and held constant for a certain time period till steady state was reached. Steady state for a thermal analysis refers to an equilibrium state at which temperature remains constant over time. The thermal profiles obtained from the cold side thermocouples were then plotted along with the heater temperature profile on a temperature vs time plot. The thermal profiles provided information about temperature uniformity on the cold side of the plate. High temperature uniformity in the plate refers to close to equal temperature magnitudes at the thermocouple locations. However, based on the heat transfer characteristics and thermal-contact properties of materials, the temperature uniformity could vary considerably. Thus, temperature uniformity provides information about temperature variation on a particular surface under consideration. Figure 3.8 shows the hot

and cold sides of a flat plate with bonded heater and thermocouples. The whole setup was insulated with glass wool.

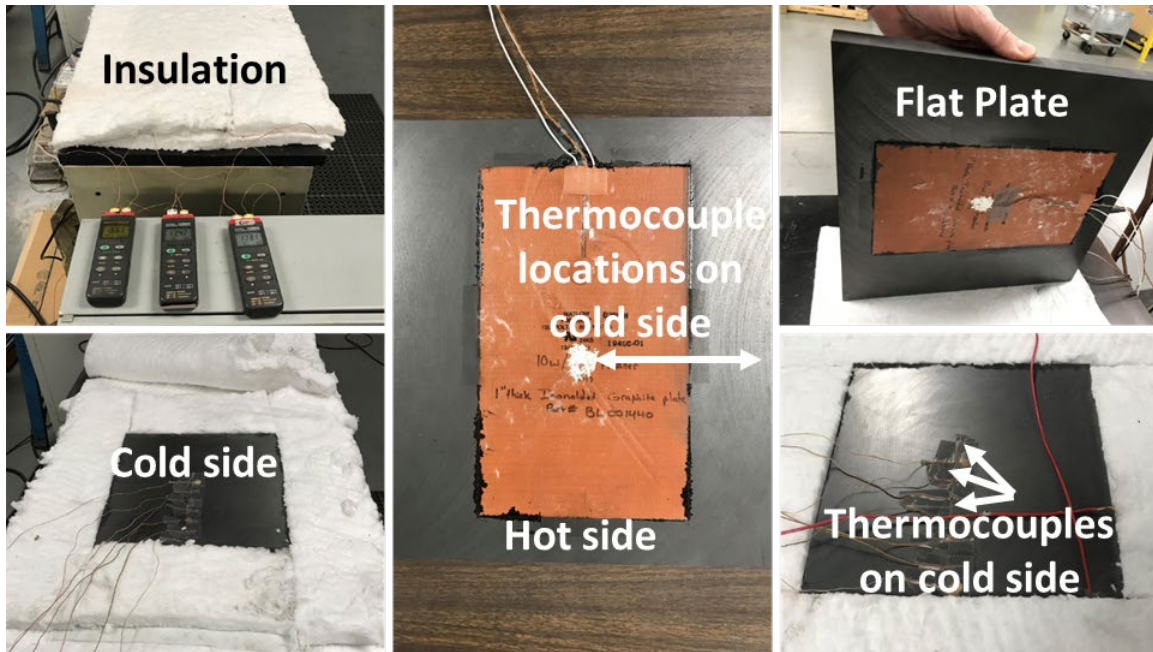


Figure 3.8: Representative Graphite Flat plate with Heater bonded on one (Hot) side and thermocouples attached on the opposite (Cold) side

Four flat plate samples were studied and are described here. First, thermal transport characteristics of a 1x12x12 inch CFOAM plate centrally bonded to a 6x10 in, 600 W, silicone type heater were determined. A thermocouple mounted directly to the heater was used as reference to the hot side temperature. Whereas, thermocouple probes each 1” apart, located on the opposing cold surface were used to record the thermal profiles along the length of the plate.

Second, a CFOAM plate (1x12x12 inch) was bonded with SS400 heat spreader (0.01x12x12 inch) material on cold side and the Silicone heater was bonded centrally on the hot side. Figure 3.9 shows the arrangement of materials that make up the flat plate.

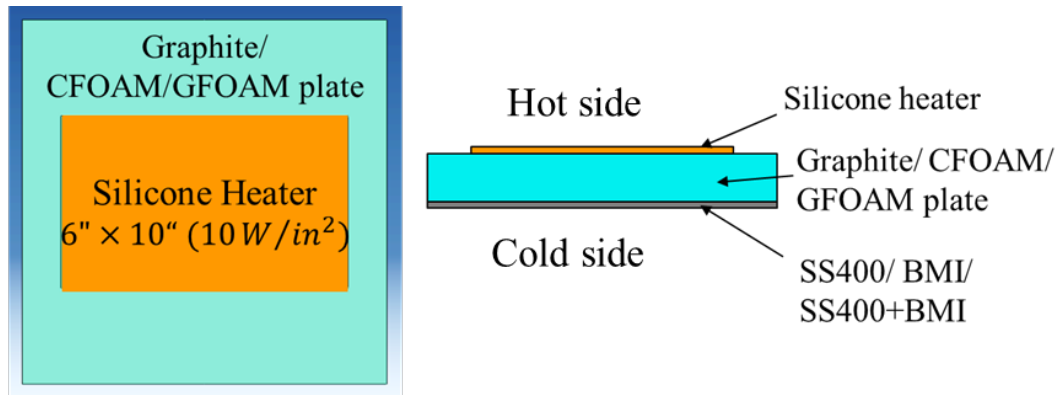


Figure 3.9: Arrangement of materials to make the Flat plate samples

Third, the BMI laminate (12 plies) was bonded to the heat spreader and the CFOAM core and thermal profiles were obtained by thermocouples on the BMI surface. Finally, a 1x12.7x12.7 inch thick graphite plate with Silicone heater was tested for temperature profiles. The thermal profiles obtained from the abovementioned experiments for these four cases were used to validate the computational heat transfer model for composite boom tool.

Next, Finite element (FE) models were developed for each of the four flat plate cases with the objective of validating the computational models. This was done by performing heat transfer simulations and comparing the thermal profiles obtained from

experiments and FE simulations. Note that, 3D FE models were set up for model validation cases, since the experimental setups led to 3D heat transfer scenarios.

The 3D FE model was setup using *Abaqus*TM (see Figure 3.10). The modeling procedure for the four flat plate samples is described here. In each case, the plate was modeled as a 3D deformable part. A solid homogeneous section was assigned to the plate. A single part was modeled, and a method of partitioning was used to define different materials to the same part. For example, for the CFOAM+Heat spreader(SS400) case, a 3D deformable part was created with thickness (1" + 0.25 mm) equal to the summation of thickness of CFOAM (1") and Heat spreader (0.25 mm). Next, the part was partitioned into two segments and a section was defined for each segment. Material properties from Table 3.1 were then assigned to each section. Similar procedure of partitioning was applied to the CFOAM+SS400+BMI case. However, this is not applicable to CFOAM and Graphite cases.

The next steps in the modeling are common to all cases. The heat spreader (SS400) material has high in-plane thermal conductivity as compared to through-thickness direction. As a result, an orthotropic material property is assigned to SS400. Accordingly, a local material orientation (1,2) was defined for the SS400 section as explained in Section 3.3.1.1. The heater was not modeled as a separate part. Instead, a rectangular edge was created on the hot side of the plate and assigned temperature boundary condition. The edge has dimensions equal to the heater element (6"*10"). The temperature boundary condition was defined with the heater-side thermal profile using an amplitude table. Figure C-6 in Appendix C provides the heater side temperature profiles for all four flat plate cases. All

the cases are defined temperature boundary conditions similarly. Convection boundary condition with a coefficient of $1.5\text{ W/m}^2\text{K}$ was defined to model heat loss to the surrounding air. An initial temperature of 25°C was assigned to the part. DC2D4 heat transfer elements were used for the model. A mesh size of $0.5''$ was chosen in order to coincide the nodes with the thermocouple locations (see Figure 3.11). This allowed capturing of thermal profiles at exact locations from the simulation and made comparison with the experiment consistent. A transient heat transfer analysis was performed for all four cases. Refer to Appendix B Table B-1 for detailed steps of the model setup in *Abaqus*TM.

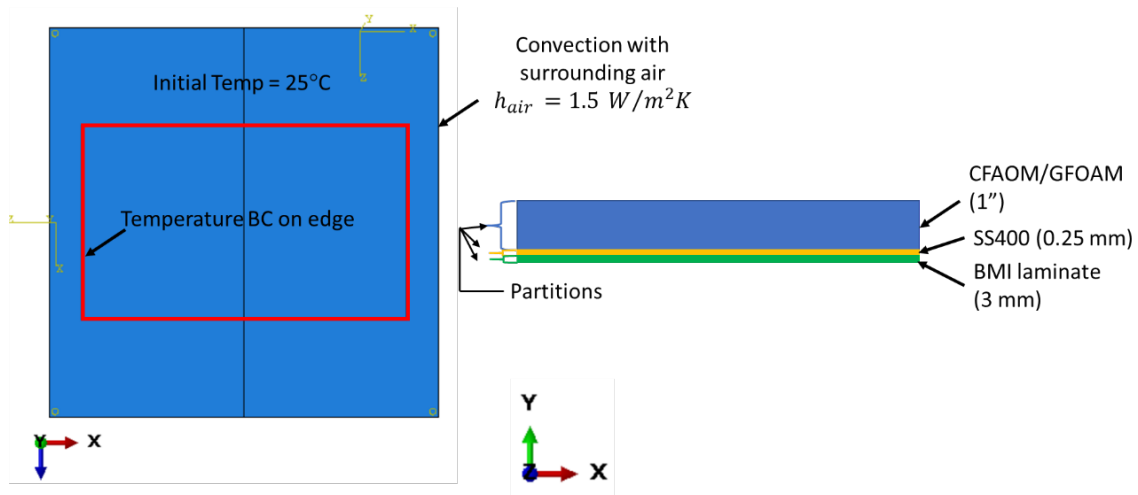


Figure 3.10: 3D Model setup for Flat plate heat transfer analysis

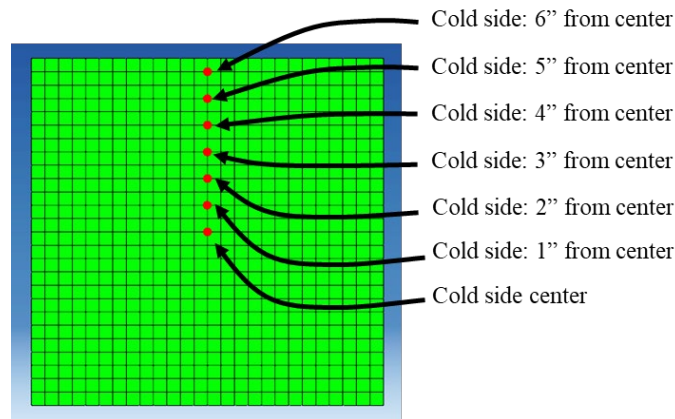


Figure 3.11: Seven temperature measurement locations on cold side of plate mesh

3.3.2 Curing analysis

Preliminary curing simulations were performed for epoxy based CFRP composite laminate. For the current analysis, COMPRO software plugin was used with *AbaqusTM*. The complete analysis consists of 3 steps namely the thermo-chemical analysis, flow-compaction analysis, and stress-deformation analysis. COMPRO has an elaborate material library with predefined material properties. Material properties for the composite laminate were predefined due to the fact that the material was used directly from the COMPRO material library. Whereas, the material properties for the tool were defined as provided in the Table 3.4. The curing simulation performed here required material properties for all three steps. Note that the thermo-chemical step required thermal properties of tool materials, while the flow-compaction and stress-deformation analysis required elastic properties.

A GFOAM core design concept was considered for the present study. Accordingly, the tool consisted of a bottom heater, GFOAM core and BMI laminate. The composite

laminates were modeled on top of the tool resting on the BMI surface (see Figure 3.13). A 2D cross section was used for performing the curing analysis. However, 3D heat transfer elements (brick elements) are preferred for the curing simulation. The reason for this is that the brick elements capture through thickness shrinkage strains better as compared to the standard 4-noded shell elements. Therefore, a single layer of brick elements were modeled out of plane of the cross section direction to make the model computationally efficient. C3D20 brick elements were used for the analysis. The section thickness in the out-of-cross section direction was determined based on the composite laminate thickness and number of elements through thickness. An aspect ratio of 5:1 was recommended for the brick elements. Accordingly, section thickness was calculated as-

$$\frac{\text{Laminate thickness}}{\text{Number of elements through thickness of laminate}} \times \text{Aspect ratio}$$

Also, boundary conditions for the flow-compaction and stress-deformation analysis were defined in a way to satisfy 2D model assumption [83].

As explained earlier, a composite prepreg was treated with a temperature curve known as a cure cycle in order to complete the curing process. Accordingly, in this case, a cure cycle was defined as a temperature boundary condition to the heater surfaces using an amplitude table in the software. The cure cycle is shown in Figure 3.12. The composite laminate was assigned Hexcel AS4-8552 material from the COMPRO built-in library. This material is a Unidirectional CFRP tape with epoxy (thermoset) resin. A composite solid section was created for the composite laminate. Individual plies were then defined to the laminate by specifying the ply thickness, orientation angle and number of integration points. Orientation was defined for the laminate by assigning a local coordinate (1,2,3)

system. The 3-axis is defined corresponding to the through-thickness direction of the laminate and 1-axis is defined along the 0° direction of the fibers.

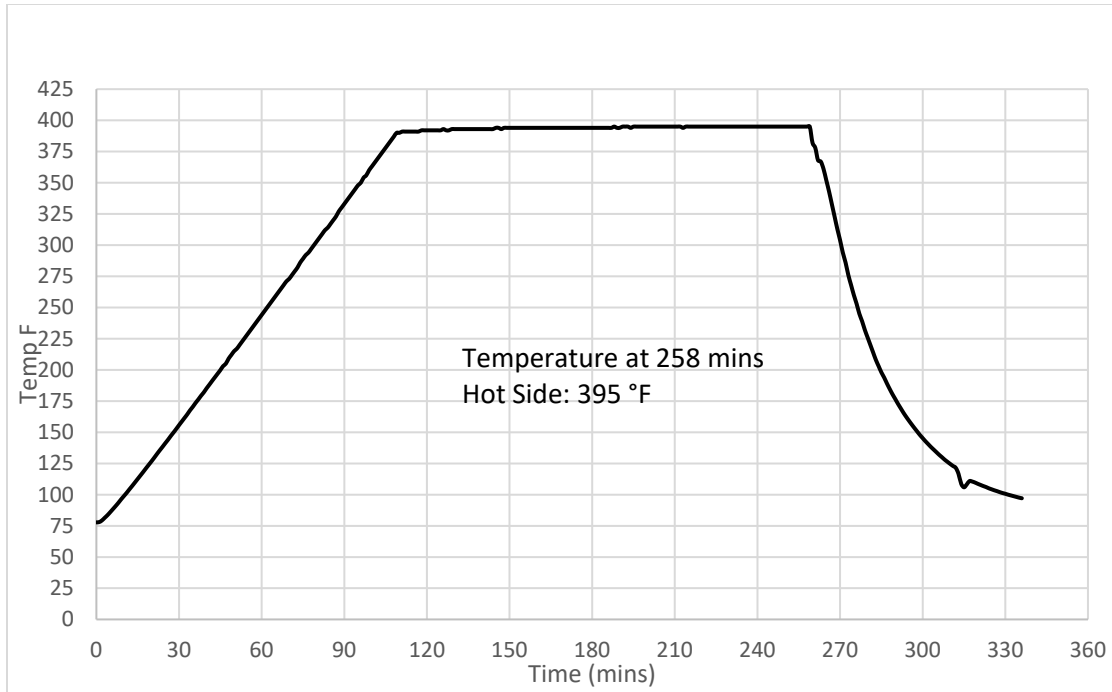


Figure 3.12: Thermocouple measured cure profile on the heater surface. Total time = 20160 sec

3.3.2.1 Thermo-chemical analysis

The thermo-chemical step is a heat transfer analysis step which takes into account thermal interactions of the composite laminate with the surrounding air and the tool surface. The composite laminate cures when it goes through the cure cycle and the resin hardens over time. The curing of the resin leads to an exothermic reaction and generates heat during the analysis. The thermo-chemical analysis also considers this internally generated heat. The governing equation for the thermo-chemical analysis is given as [84]:

$$\frac{\partial}{\partial t}(\rho C_p T) = \nabla(k \nabla T) + \dot{Q} \quad (3.3)$$

where ρ is the density of the composite laminate, C_p is the specific heat, k is the anisotropic thermal conductivity and \dot{Q} is the resin heat generation rate which is given as

$$\dot{Q} = \frac{d\alpha}{dt} (1 - V_f) \rho_r H_R \quad (3.4)$$

Where α is the degree of cure which is a measure of the extent of cross-linking in the thermosetting polymer, $\frac{d\alpha}{dt}$ is the cure rate, V_f is the fiber volume fraction, ρ_r is the resin density and H_R is the total heat evolved during the curing process. The degree of cure can be determined experimentally using the differential scanning calorimetry technique. The finite element formulation for the thermo-chemical analysis is provided in [84].

The model setup for this analysis is shown in Figure 3.13 and described here. The heater surfaces in the tool were defined temperature curve (cure cycle shown in Figure 3.12) boundary condition. Convection boundary condition with a coefficient of $1.5 \text{ W/m}^2\text{K}$ was defined on the tool and composite laminate surface to model heat loss to the surrounding air. A tie constraint was modeled at the interface between the tool and the GFOAM core. All components of the tool and the composite laminate were defined an initial temperature of 25°C . This analysis was used to obtain the temperature profile and degree of curing of the composite laminate. Refer to Appendix B Table B-3 I for detailed procedure of thermo-chemical analysis.

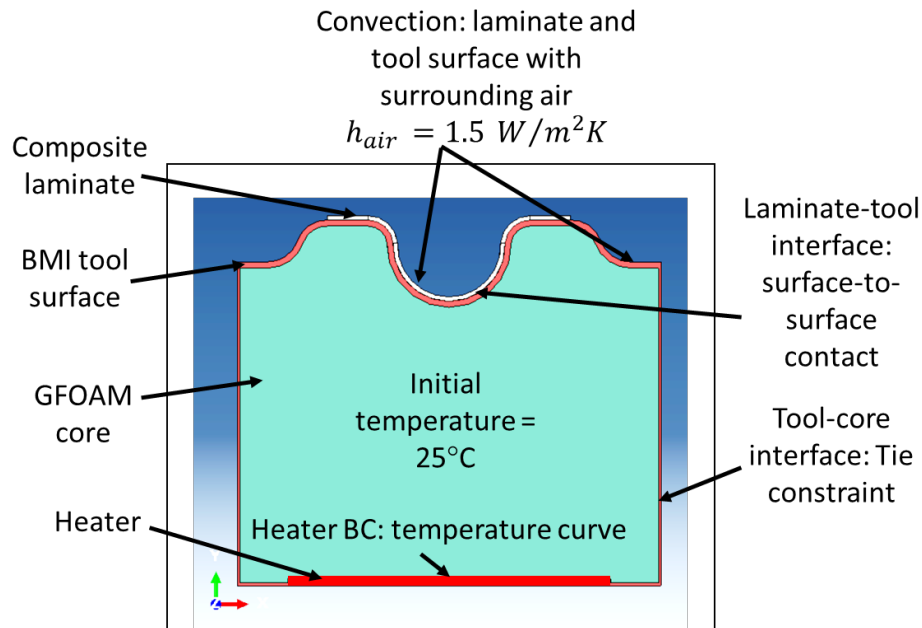


Figure 3.13: Model setup for cure analysis

3.3.2.2 Flow-compaction analysis

As mentioned earlier, the processing of composite laminate requires application of temperature and pressure. Temperature is applied by way of cure cycle while pressure is applied by vacuum bagging technique. When pressure is applied, resin flow occurs in the composite laminate resulting in variations of fiber and resin volume fractions as well as thickness variations. An important assumption made is that the composite laminate which consists of fiber bed reinforced in resin is void free. Further, the fibers are assumed to be incompressible and the resin as incompressible Newtonian fluid. The governing equations for the flow-compaction analysis are provided here. Considering a representative element of a composite part, the equilibrium equation for the differential composite element is as [85]-

$$(\overline{\sigma}_{ij} - \delta_{ij}P)_j + F_i = 0 \quad (3.5)$$

Where $\overline{\sigma}_{ij}$ is the effective stress of fiber bed, δ_{ij} is the Kronecker delta ($\delta_{ij} = 1$ for $i=j$ and $\delta_{ij} = 0$ for $i \neq j$), P is the pressure of curing resin and F_i are the internal body forces.

The resin flow follows Darcy's law. Applying the law of mass conservation, we have

$$(\dot{u}_i)_{,i} + (v_i)_{,i} = 0 \quad (3.6)$$

Where $(\dot{u}_i)_{,i}$ is the fiber bed velocity, $(v_i)_{,i}$ is the resin velocity relative to the fiber bed which is given as

$$v_i = -\frac{K_{ij}}{\mu} (P + \rho_r g h)_{,i} \quad (3.7)$$

where K_{ij} is the fiber bed permeability tensor, μ is the viscosity of resin, ρ_r is the resin density, g is the gravitational acceleration and h is the height above reference point. Therefore, the flow continuity equation for the composite by substituting Equation (3.7) in Equation (3.6) is given as

$$(\dot{u}_i)_{,i} = \left(\frac{K_{ij}}{\mu} (P + \rho_r g h)_{,i} \right)_{,i} \quad (3.8)$$

The finite element formulation for the flow-compaction analysis is provided in [85]. The modeling procedure for this step is explained here. This analysis mainly concerns with the interaction between the composite laminate and the tool surface. In the present study, a pressure load of 14 psi was applied on the top surface of the composite laminate. Next, pore pressure (resin pressure) was defined as a boundary condition to the composite laminate. A mechanical contact was defined between the laminate and tool interface. The

tangential behavior of the contact was defined with a friction coefficient of 0.15 and normal behavior was defined with a “Hard” contact. Next, displacement boundary conditions were defined to constrain the tool from rigid body movement. The bottom edge of the tool was specified with zero displacement in X and Y directions (The model cross section is in XY plane). The entire tool and the laminate surface were defined zero displacement in the Z direction. Lastly, all the components were assigned initial temperature equal to 25°C. This analysis was used to capture the volume fraction of resin within the composite. Refer to Appendix B Table B-3 II for detailed procedure of flow-compaction analysis.

3.3.2.3 Stress-Deformation analysis

The third and the last step in the curing analysis considers residual stress-induced deformation in the composite laminate due to the cure cycle. These residual stresses are developed due to a) mismatch of thermal expansion coefficients between the fiber and resin, b) volumetric shrinkage of the resin due to temperature gradient in the through thickness direction and, c) interaction between the composite laminate and the tool. The governing equations for the stress-deformation analysis are provided here [84]. The potential energy function for the composite system is given as

$$\boldsymbol{\pi}_p = \boldsymbol{U} + \boldsymbol{\Omega}_w \quad (3.9)$$

Where U is the strain energy of the system, $\boldsymbol{\Omega}_w$ is the work done by body forces and surface tractions during deformation. The detailed expression of the potential energy of the system is given as

$$\pi_p = \int_{\Omega} \left(\frac{1}{2} \{\boldsymbol{\varepsilon}\}^T [\mathbf{C}] \{\boldsymbol{\varepsilon}\} - \{\boldsymbol{\varepsilon}\}^T [\mathbf{C}] \{\boldsymbol{\varepsilon}_0\} + \{\boldsymbol{\varepsilon}\}^T \{\boldsymbol{\sigma}_0\} \right) d\Omega - \int_{\Omega} \{\mathbf{u}\}^T \{\mathbf{F}_B\} d\Omega - \int_{\Gamma} \{\mathbf{u}\}^T \{\boldsymbol{\varphi}\} d\Gamma \quad (3.10)$$

Where $\{\boldsymbol{\varepsilon}\}$ is the strain field, $[\mathbf{C}]$ is the plain strain material stiffness matrix, $\{\boldsymbol{\varepsilon}_0\}$ are initial strains, $\{\boldsymbol{\sigma}_0\}$ are initial stresses, $\{\mathbf{u}\}$ is the displacement field, $\{\mathbf{F}_B\}$ are the body forces and $\{\boldsymbol{\varphi}\}$ are the surface tractions. The detailed finite element procedure is provided in [84].

This analysis consisted of two steps namely the stress-deformation step and tool-removal step. For the stress-deformation step, the modeling setup was the same as for flow-compaction analysis. For the tool removal step, the tool was disconnected from the composite laminate. This was done by defining an interaction called Model change. On the model change interaction window, all the tool components namely Tool surface and GFOAM core were selected and deactivated from the model. Further, the mechanical contact between the Tool surface and composite laminate was deactivated. The composite laminate was thus separated from the rest of the tool. Next, the composite laminate surface was defined zero displacement in the Z-direction. Also, the laminate was defined zero displacement in the X and Y directions at center location. These boundary conditions were defined to restrict rigid body motion. This analysis was used to predict the process induced deformation (displacement) of the composite laminate. Refer to Appendix B Table B-3 III for detailed procedure of stress-deformation analysis.

3.3.2.4 Model Cases

Two cases of composite laminate were considered for the preliminary study of cure process.

1. 2 mm thick composite laminate with $[(0/90)_2]_S$ layup was considered. That is a total number of 8 plies each of 0.25 mm thickness are defined. Number of elements through thickness of laminate = 4, Section thickness = 2.5 mm
2. Thin-ply (< 0.0635 mm/ply) laminate 0.16 mm in thickness with $[45/0/45]$ layup was considered. That is a total number of 3 plies with each of the 45° orientation plies 0.06 mm thick and 0° ply 0.04 mm thick. Number of elements through thickness of laminate = 1, Section thickness = 0.8 mm

All three analyses were carried out for Case 1. Note that the results obtained from thermochemical analysis were fed as input to the flow-compaction step and subsequently flow-compaction results were fed as input to the stress-deformation analysis. While for Case 2, a uniform resin volume fraction was assumed since thin-ply laminate is estimated to have negligible resin flow. As a result, thermo-chemical analysis was followed by stress-deformation analysis.

3.4 Results and Discussion

3.4.1 Model Validation results

Thermal profiles at the seven defined thermocouple locations are obtained both from the experiments and simulations. A comparison between these profiles is presented in this section. The material properties used for the heat transfer simulations are provided

in Table 3.1. Each plate sample was heated in the experiments for a certain period of time. The temperatures at the seven thermocouple locations are compared at the end of that time period for each case. For example, for the CFOAM case the predicted and measured temperatures are compared at time = 140 min. Also, temperature uniformity is calculated for each case. Temperature uniformity for the flat plate samples refers to the difference in temperatures at the 1st and 7th thermocouple locations along the length of the plate. Table 3.2 provides temperature uniformity results of the flat plate samples. As can be seen, the temperature uniformity is poor for the CFOAM case but improves with the addition of the SS400 layer. This is because the SS400 has high in-plane thermal conductivity. This allows improved heat transfer in the in-plane direction and thus produces better uniformity. This is further aided with the addition of the BMI laminate layer. Graphite plate offers the best temperature uniformity due to its excellent conductivity. There is some discrepancy observed between the experimental and analysis results. This discrepancy will be discussed on case-by-case basis.

Table 3.1: Material properties used for the transient heat transfer analysis

Materials	Density	Thermal Conductivity		Specific Heat	
	ρ (g/cm^3)	k ($\frac{W}{mK}$)		c_p ($\frac{J}{g^{\circ}C}$)	
CFOAM with BMI Laminate Facesheet	0.662 ²	Temp ($^{\circ}C$) ¹	k^1	Temp ($^{\circ}C$)	c_p
		38	0.458	25	0.837
		93	0.518		
		149	0.565	160	2.512
		204	0.612		
Fiber Reinforced BMI Laminate (10- ply)	1.480 ²	Temp ($^{\circ}C$) ¹	k^3	Temp ($^{\circ}C$)	c_p^4
		38	0.502	25	0.77
		93	0.448		
		149	0.296	160	1.68
		204	0.222		
Carbon Foam	0.565 ²	Temp ($^{\circ}C$) ¹	k^1	Temp ($^{\circ}C$)	c_p
		38	.453	38	0.729
		93	.525	93	0.880
		149	.591	149	1.018
		204	0.649	204	1.140
Heat Spreader (SS400)	1.672	In-plane k^5	Through- plane k^5	Temp ($^{\circ}C$)	c_p

		400	3.7	38	0.729
				93	0.880
				149	1.018
				204	1.140
Graphite (GM-10)	1.82 ⁶	83 ⁶		Temp (□C)	c_p
				38	0.729
				93	0.880
				149	1.018
				204	1.140
Graphite Foam (GFOAM)	0.3	Temp (°C) ¹	k^1	Temp (□C)	c_p
		38	13.3	38	0.755
		93	14.2	93	0.932
		149	14.8	149	1.086
		250	15.3	250	1.306

1 Thermal conductivity of CFOAM and Epoxy-coated CFOAM: from NETZSCH

2 Experimental/Measured values

3 Values estimated using rule of mixtures.

4 BMI specific heat assumed to be equivalent to thermoset polymers. Reference R.W.Warfield et.al, "The Specific Heat For Thermoset Polymers", U. S. NAVAL ORDNANCE LABORATORY Report 6255, 1973

5 SurSeal TDS

6 Graphtek LLC GM-10 Datasheet

Table 3.2: Flat Plate test cases

Sample ID	Dimensions (TxWxL) (in)	Heater Temp @ Steady State (F)	Test Temp Uniformity ΔT (F)	Analysis Temp Uniformity ΔT (F)
CFOAM	1x12x12	367	151	139
CFOAM + 0.25mm SS400	1x12x12	357	51	30.36
CFOAM+0.25mm SS400+BMI	1x12x12	443	32	38.1
Graphite	1x12.7x12.7	354	6	2.06

3.4.1.1 Case 1: CFOAM plate

The temperature characteristics of CFOAM plate obtained from the analysis were compared with the experimental result at time = 140 min in Figure 3.14. Accordingly, the thermocouple locations are plotted on the x-axis and temperatures correspondingly to the locations are plotted on y-axis of the plot. The test and analysis curves represent the temperatures obtained from experiment and simulation respectively at time = 140 min. A maximum discrepancy of 33.65F at 3” location was observed between the test and the analysis. There are several possible causes for the noticed discrepancy:

1. The heat losses through the system during the test cannot be estimated accurately for the plate.

2. Heater center thermal profile is used as input (temperature BC) for the heater surface in the analysis. Although in reality there could be some gradient in the heater temperature along the length and width of the heater element.
3. The sensitivity of the thermocouple probes could lead to some error in the temperature measurements.

The overall temperature uniformity along the plate length from center to 6" from center was observed to be 139 F.

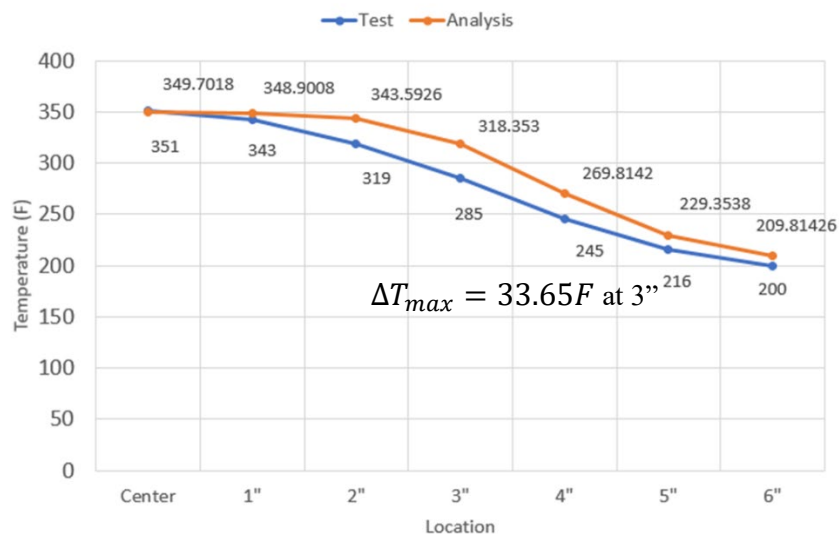


Figure 3.14: Thermal characteristics of CFOAM at specific locations on cold side of plate at t = 140 min

3.4.1.2 Case 2: CFOAM plate + 0.25mm SS400 heat spreader

The thermal characteristics of CFOAM plate + 0.25mm SS400 heat spreader obtained from the analysis were compared with the test result at time = 236 min in Figure 3.15. A maximum discrepancy of 11.42F at 6" was observed. Similar factors as the

CFOAM case could be attributed to the difference in temperature values between the test and analysis. Additionally, thermal gap conductance at the interface of the CFOAM and SS400 material could be a reason for the inconsistency. Thermal gap conductance is a contact property defined at the interface of two contacting surfaces. This property is very specific to the contacting pairs and the geometry. Also, it is difficult to determine experimentally. For the current study, the method of partitioning was used as described in section 3.3.1.2. This does not allow to take into account the contact conductance and as a result, could be a cause of the inconsistency between test and analysis results.

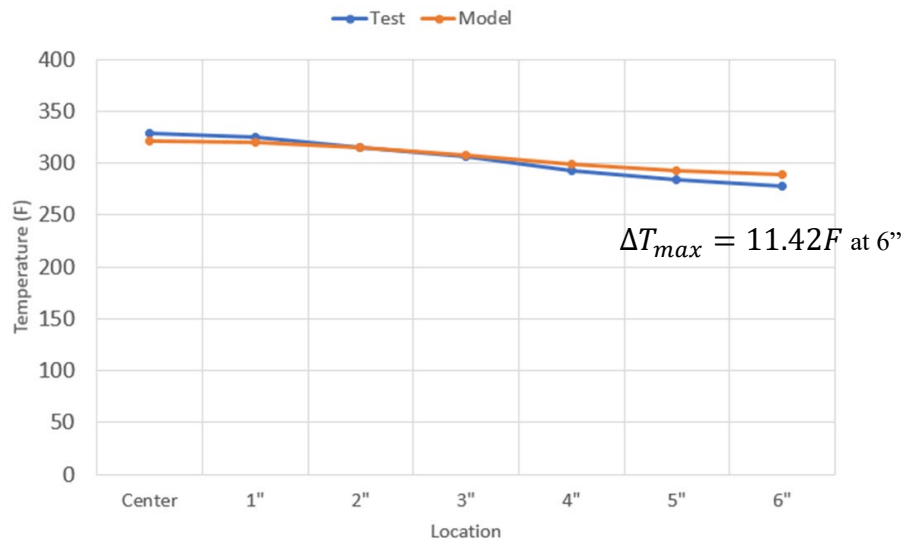


Figure 3.15: Thermal characteristics of CFOAM + 0.25mm SS400 at specific locations on cold side of plate at t = 236 min

3.4.1.3 Case 3: CFOAM plate + 0.25mm SS400 heat spreader + BMI laminate (12 plys)

The thermal characteristics of CFOAM plate + 0.25mm SS400 heat spreader + BMI laminate (12 plys) obtained from the analysis were compared with the test result at time = 269 min in Figure 3.16. A good agreement was observed between the test and analysis with

a maximum discrepancy of $9.49F$ at $4''$. The BMI laminate has higher conductivity normal-to-fiber direction as compared to along-the-fiber direction. Thus, ideally the BMI laminate should be defined as an orthotropic material. However, for the current analysis the BMI laminate was idealized as an isotropic material. The discrepancy of temperature uniformity between the test and the analysis could be attributed to this assumption of BMI laminate material.

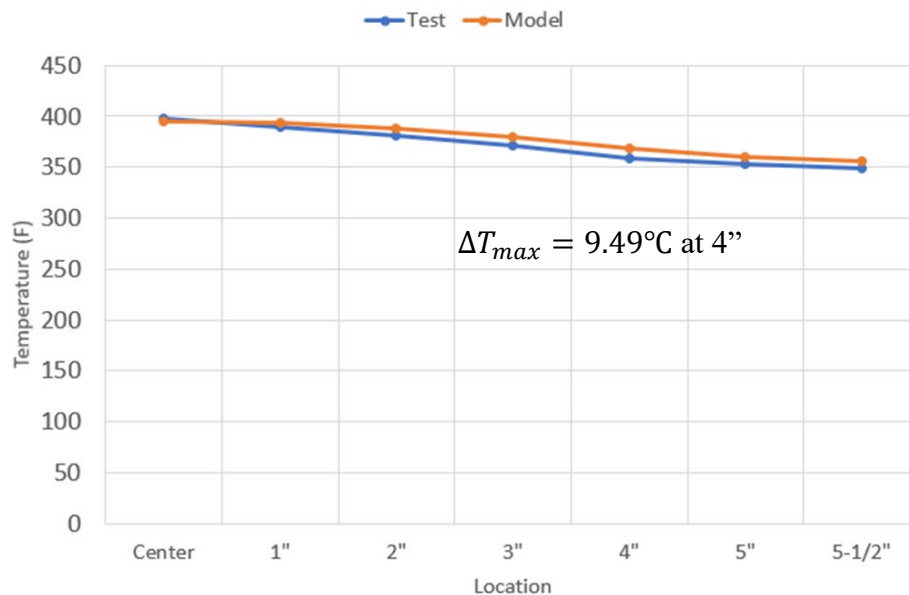


Figure 3.16: Thermal characteristics of CFOAM + 0.25mm SS400 + BMI laminate 12 plies at specific locations on cold side of plate at $t = 269$ min

3.4.1.4 Case 4: Graphite plate

The thermal characteristics of graphite plate obtained from the analysis were compared with the test result at time = 240 min in Figure 3.17. An excellent agreement was observed between the test and analysis results with a maximum discrepancy of $2.5F$ at $4''$ location. The temperature uniformity along the plate length from center to $6''$ from center

was observed to be $2.06F$. The significantly higher temperature uniformity is due to the high thermal conductivity of graphite.

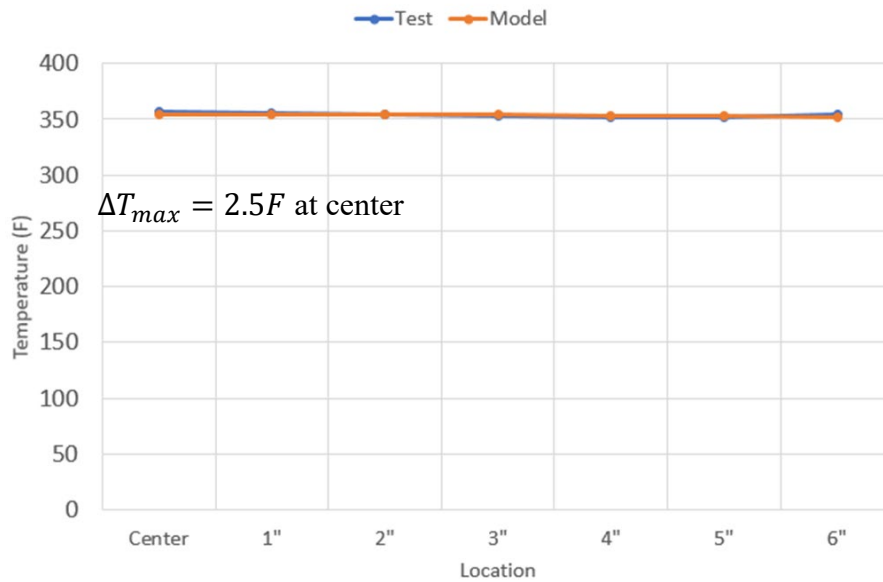


Figure 3.17: Thermal characteristics of graphite plate at specific locations on cold side of plate at $t = 240$ min

3.4.2 2D Heat Transfer analysis results

3.4.2.1 Optimization approach

Once the computational models for the heat transfer analysis were validated, 2D models were then used to carry out numerical studies to identify optimal designs and provide guidance with regard to the choice of materials and location of heaters. The 2D model described in Section 3.3.1.1 was employed to investigate the most relevant parameters of the tool. The identified parameters were number of heaters, heater locations in the tool, heat spreader and core materials. More than one heater could be used in the tool to expedite the heating process. The location of these heaters would in turn decide the heat transfer characteristics. Heat spreader (SS400) material has high in-plane thermal

conductivity. As a result, use of heat spreader would facilitate uniformity of temperature on the tool surface. Finally, two core materials under consideration namely CFOAM and GFOAM influence the thermal transport characteristics especially gradient in the tool. The temperature gradient in the tool would in turn induce thermal stresses and strains in the tool. It was therefore understood that each parameter could have considerable effect on the thermal behavior of the tool. As a result, it was necessary to identify and analyze different configurations of these parameters.

The design of experiments (DOE) method was used for determining the effect of the design options and parameters. Accordingly, nine concepts were designed for the CFOAM core material. These concepts have carefully chosen combinations of the abovementioned parameters. Further, three different concepts were evaluated for GFOAM core. A total of twelve design concepts were evaluated using the 2D model.

3.4.2.2 Design of experiments (DOE)

Figure 3.18 shows the DOE consisting of a total of 9 concepts (C1-C9) all utilizing CFOAM as the core material. Three heater element types namely Polyimide (L), Silicone (M) and MICA (H) were evaluated. The symbols in the parenthesis are used in the figure for simplified representation. Four heater locations namely bottom (B), sides (S), top (T) and internal (Int) were identified. Two choices of application of heat spreader with thickness 0.25 mm (1) and 0.9 mm (2) were considered. Lastly, for the tool surface BMI laminate (C) and graphite (GR) materials were considered.

Materials	Concepts	C1	C2	C3	C4	C5	C6	C7	C8	C9
Max Heater Temperature Capability ¹	Symbol									
Polyimide ² (392F)	L	L								
Silicone (450F)	M		M	M	M	M				
MICA (572F)	H						H	H	H	H
Heater Location	Symbol									
Bottom	B		B		B		B		B	
Sides	S			S	S			S	S	
Top	T	T								
Internal	Int					Int				Int
Spreader Thickness ³ (mm)	Symbol									
0.25 (Apply to top surface only)	1	1	1	1	1		1	1	1	
0.9 (Apply internal, sides and bottom as needed)	2		2	2	2		2	2	2	
Tool Surface	Symbol									
BMI (composite)	C	C	C	C	C		C	C	C	
Graphite	GR					GR				GR
¹ All heater watt density assumed to be 10W/in ²										
² Polyimide heater top surface mount only (flexible)										
³ Only 0.25mm spreader can be applied to complex shape on surface, but if added thickness is needed multiple plies can be considered. Assume a single 0.25mm for initial study. 0.9mm will be used on all other internal, sides and/or bottom surfaces when applicable.										

Figure 3.18: DOE: A study of design space

Following the DOE, all concepts (C1-C9) were evaluated at maximum temperature output as described in section 3.3.1.1. The maximum temperature out is 392F for Polyimide heaters, 450F for Silicone heaters and 572F for MICA heaters. The material properties used for the heat transfer analysis are provided in Table 3.1. Transient heat transfer analyses for all concept designs were performed to steady state conditions. Accordingly, a time period of 26000 sec was defined for each analysis. Steady state is said to be achieved when the temperature change in a time increment is less than the defined value. The minimum allowable temperature change was defined as 0.0001. When the temperature change dropped lower than the defined value, the analysis was terminated considering steady state was reached. Five model configurations are shown in Figure 3.19 where similar concepts are combined together and described here. Concept 1(C1) consists of a carbon foam

(CFOAM) core, polyimide heater and BMI tool surface. Polyimide heater is mounted on the upper surface of the core and was sandwiched between the BMI laminate and CFOAM core. The BMI tool surface envelops the CFOAM core as shown in Figure 3.19(a). Concepts 2 and 6 (C2 and C6) consists of a CFOAM core, Silicone heater for C2 whereas MICA heater for C6 and BMI tool surface. The heat spreader (SS400) envelops the CFOAM core. The SS400 layer is 0.9 mm thick on sides and bottom whereas a thinner 0.25 mm layer is used on the upper surface. The reason for using a thinner SS400 layer on the upper surface is that it would conform to the omega shaped contour of the tool top. The BMI tool surface envelops the heat spreader material. The heater is located at the bottom sandwiched between CFOAM core and heat spreader (SS400) as shown in Figure 3.19(b). Concepts 3 and 7 (C3 and C7) have the exact same configuration as the C2 and C6. The only difference is the location of heaters. The heaters are located on the sides sandwiched between CFOAM core and heat spreader (SS400) as shown in Figure 3.19(c). Again, Concepts 4 and 8 (C4 and C8) have similar construction as C2 and C6. The heaters in these concepts are located on the sides as well as the bottom sandwiched between CFOAM core and heat spreader (SS400) as shown in Figure 3.19(d). Concepts 5 and 9 (C5 and C9) consist of a CFOAM core, Silicone heater for C5 whereas MICA heater for C9 and graphite tool surface. The heater is located internally between CFOAM core and graphite tool surface as shown in Figure 16e. Concepts C10, C11 and C12 utilize GFOAM core instead of CFOAM core and heat spreader (SS400) layer is not used. Apart from the two modifications, the concepts C10, C11 and C12 have the same configuration as concepts C1, C2 and C6 respectively. The reason for eliminating the SS400 material in the GFOAM

concepts is that the GFAOM itself has high thermal conductivity and as a result, does not require additional spreader material. Dimensions of tool materials for each of the nine concepts are provided in Appendix C.

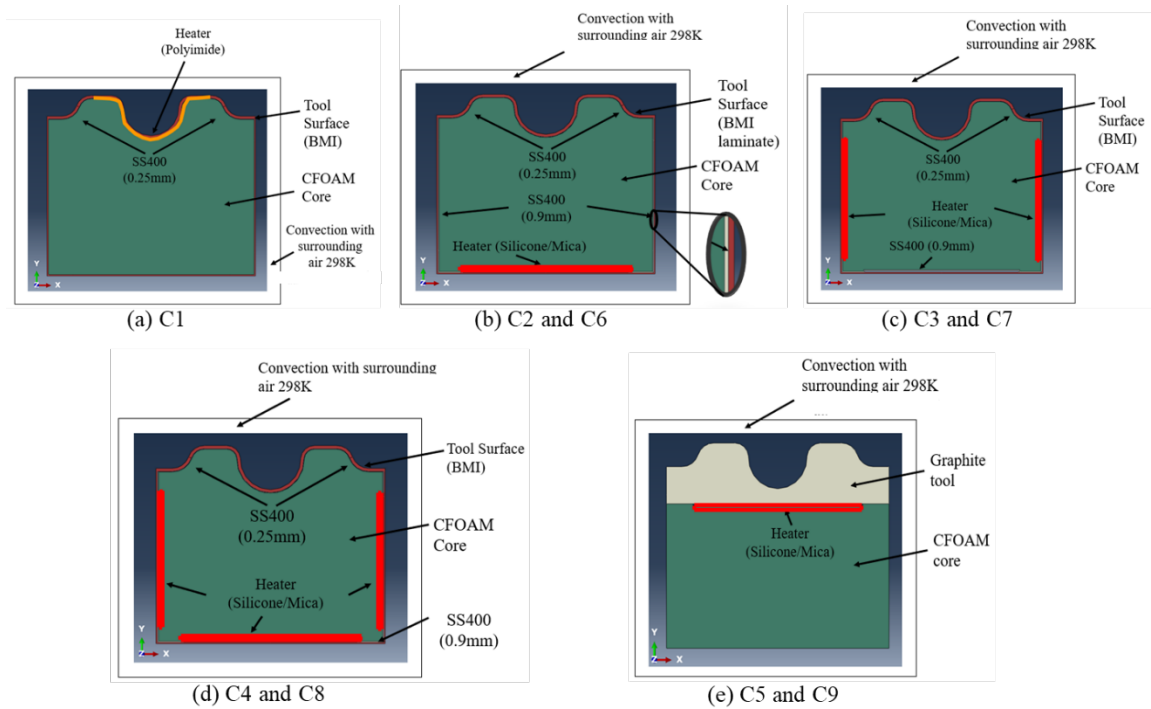


Figure 3.19: Model configurations for concepts C1 – C9

3.4.2.3 Results of model concepts

As described in section 3.3.1.1, transient heat transfer analysis was performed for each of the 12 concepts. All the concepts were evaluated to steady state condition. The results studied here are 1. Temperature uniformity on the surface of the tool, 2. Temperature drop between heater and tool surface, 3. Time required to reach steady state, 4. Temperature evolution and gradient in the tool. Study of each of these results is significant because they offer guidance regarding the choice of materials and heater

placement. Additionally, these results provide useful information about the thermal stability and energy efficiency of the tool.

1. **Temperature uniformity on the surface of the tool:** Temperature uniformity in the present work is defined as the difference of temperature between the points 1 and 2 at steady state as shown in Figure 3.20. Point 1 corresponds to the center of the tool surface and point 2 corresponds to the center of the top flat land. The composite laminate cured on the tool surface runs between the center of one flat land to the center of the other. The tool is symmetry about the line of symmetry shown in Figure 3.20. As a result, the temperature uniformity is calculated only between points 1 and 2 neglecting the surface beyond point 2. The calculated values for all 12 concepts are provided in Table 3.3. Concept pairs C2 & C6, C3 & C7, C4 & C8 have 1, 2 and 3 heaters respectively where C2-C4 have silicone heaters and C6-C8 use Mica heaters. These contact pairs have comparable temperature uniformity values. However, for the Mica heater (Max temp = 572F) concepts, the value is slightly higher because of higher gradient between the tool and the surrounding air allowing more heat loss via convection. C1, C5 and C9 concepts have excellent temperature uniformity. For C1, this is due to the flexible polyimide heater placed just underneath the BMI laminate. While for C5 and C9, Graphite is used as the upper tool surface which offers high thermal conductivity. The GFOAM concept C10 shows very similar trend as C1. Again, for C10 and C11, the values are slightly higher than C2 and C6 respectively due to better heat transport characteristics of GFOAM as compared to CFOAM core.

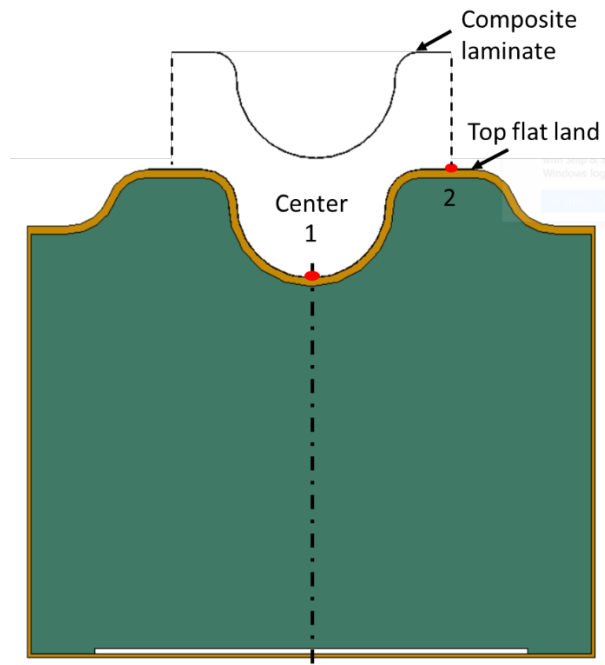


Figure 3.20: Point 1: Tool surface center, Point 2: Tool flat land center, temperature at Points 1 and 2 are used for calculating Temperature uniformity. Dotted line passing through point 1 is the line of symmetry of the tool

Table 3.3: Composite Boom tool thermal analysis results for CFOAM and GFOAM core concepts

Concept	Core Material	Heater element/ Temperature (°F)	Average temperature on tool surface (°F)	Temperature drop (°F)	Temperature uniformity of tool surface	Time required to reach Steady state (min)	Temperature gradient (°F)
C1	CFOAM	Polyimide/392	390.59	1.41	0.54	417	65.34
C2	CFOAM	Silicone/450	388.87	61.13	1.97	229	66.46
C3	CFOAM	Silicone/450	422.06	27.94	4.68	164	37.3
C4	CFOAM	Silicone/450	421.7	28.3	4.34	155	36.76
C5	CFOAM	Silicone/450	449.56	0.44	0.16	368	140.62
C6	CFOAM	MICA/572	491.96	80.04	2.63	236	88.02
C7	CFOAM	MICA/572	535.42	36.58	6.22	168	48.96
C8	CFOAM	MICA/572	533.08	38.92	5.77	158	48.24
C9	CFOAM	MICA/572	571.96	0.04	0.21	380	181.8
C10	GFOAM	Polyimide/392	390.57	1.43	0.55	51	7.02
C11	GFOAM	Silicone/450	432.68	17.32	3.06	48	20.92
C12	GFOAM	MICA/572	549.56	22.44	4.05	50	27.18

2. **Temperature drop between heater and tool surface:** The maximum temperature output for each heater element used in the concepts is provided in the Table 3.3. The temperature drop is defined as the difference in heater temperature and average tool surface temperature at steady state. The average temperature on tool surface is calculated with nodal temperatures between the centers of the top flat lands (see Figure 3.20). Figure 3.21 and Figure 3.22 show the maximum and minimum temperature drop in concepts C6 and

C9 respectively. Bottom heater concepts namely C2 and C6 produce a notable temperature drop. This is due to the poor heat transport in CFOAM material. While for the same configuration, GFOAM concepts C11 and C12 show considerably lower drop suggesting better heat transfer. The performance improves to some extent with multiple heaters but at the expense of additional power consumption. C1&C10, C5&C9 show minimal temperature drop. This result is important to study the energy efficiency of the tool. The concept with a high temperature drop indicates poor energy efficiency and vice versa.

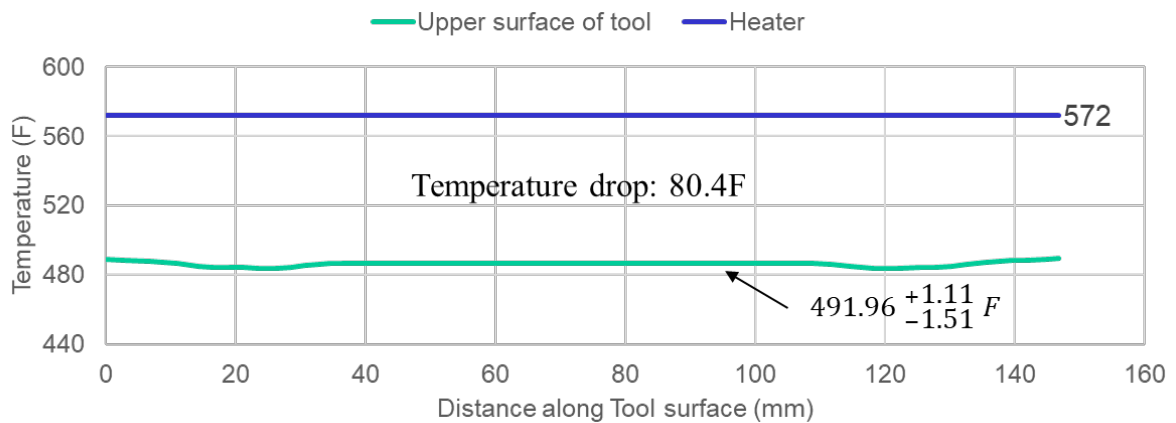


Figure 3.21: Temperature uniformity and drop in Concept C6 at steady state

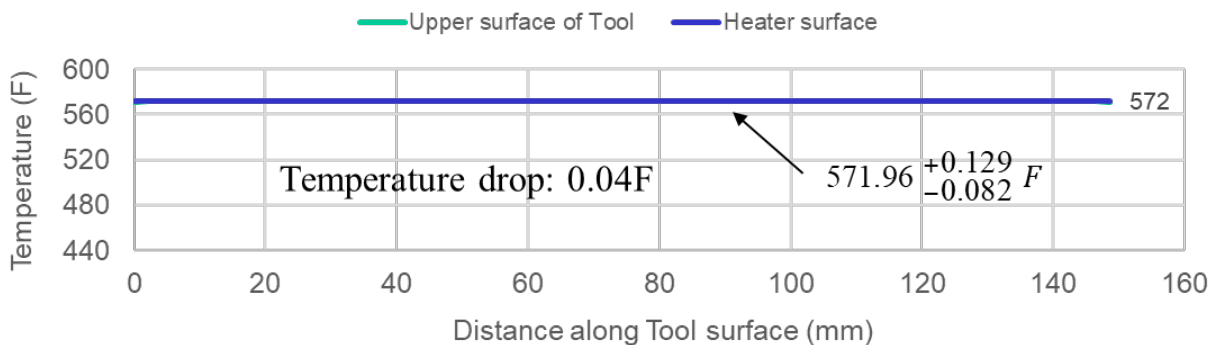


Figure 3.22: Temperature uniformity and drop in Concept C9 at steady state

3. **Time required to reach steady state:** Time required to reach steady state is defined as the time required to achieve thermal equilibrium in the tool. This result indicates the time which the tool needs to be heated to the required temperature before curing the composite laminate. Thus, it indirectly influences the energy efficiency of the tool. The time periods to reach steady state observed in the concepts are presented in Table 3.3. The concept pairs C2 & C6, C3 & C7, C4 & C8 have comparable time periods with a decreasing trend as heaters are added. All GFOAM concepts C10, C11 and C12 take exceptionally low time to reach steady state which is again attributed to the excellent heat transfer characteristics of GFOAM. On the other hand, C1, C5&C9 take longest time to reach steady state. This is because they consist of CFOAM occupying majority volume of the tool. The thermal behavior of these concepts can be better understood by observing the temperature evolution in the tool.

4. **Temperature evolution and gradient in the tool:** Temperature gradient in the tool is defined as the temperature variation in the tool at steady state. This result indicates the heat transport characteristics of the tool materials. The temperature gradient within the tool can induce thermal stresses and strains which may lead to warpage in the tool. This in-turn would affect the performance and the life of the tool. The temperature gradients observed in the concepts are presented in Table 3.3. The temperature evolution in the tool with respect to time influences the temperature uniformity on the tool surface as well as the time required to achieve steady state. Figure 3.23 shows the temperature evolution in the C1 concept at four time instances namely 1 min, 10 min, 100 min and 400 min. A rapid temperature rise is seen in the upper region of the tool due to vicinity with the polyimide

heater. However, it takes a long time for the heat to travel down through the bulk of the CFOAM core. As a result, a considerable (65.34F) temperature gradient is observed in this concept at steady state. However, substituting the CFOAM core with GFOAM in C10 improves the heat transport drastically yielding a temperature gradient of only 7F. Figure 3.24 shows temperature contour of tool at steady state in C1 and C10 concepts with CFOAM and CFOAM respectively. Similarly, concepts C11 and C12 shown significant decline in temperature gradients than their CFOAM counterparts (that is C2 and C6). Thus, GFOAM concepts can be said to be more thermally stable.

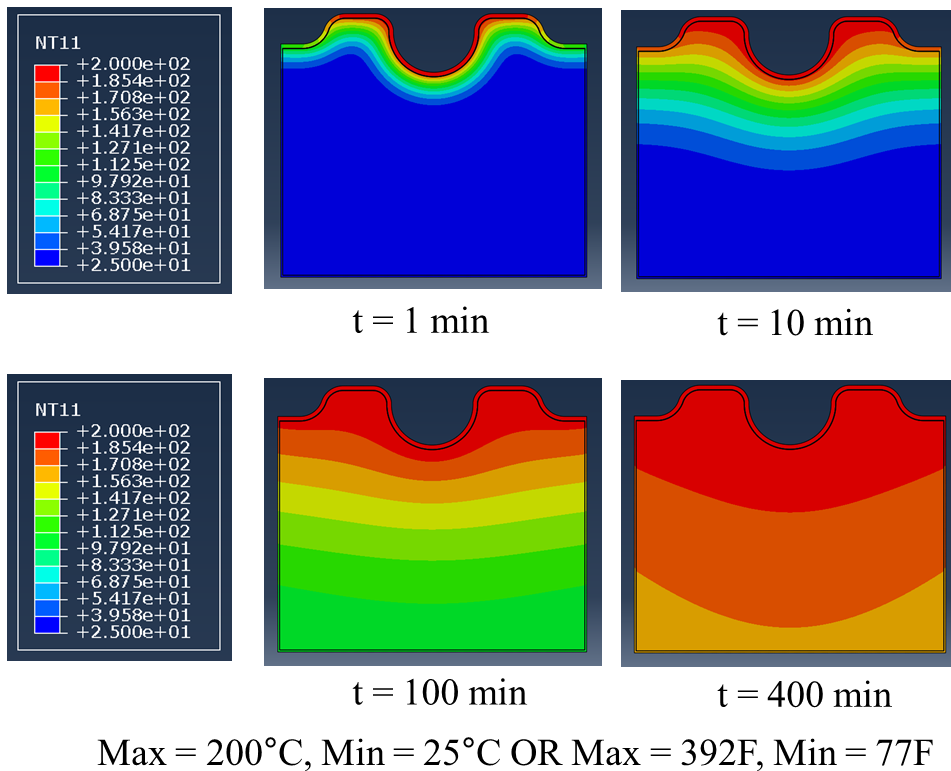


Figure 3.23: Temperature evolution contours in C1 concept at t = 1min, 10 min, 100 min and 400 min

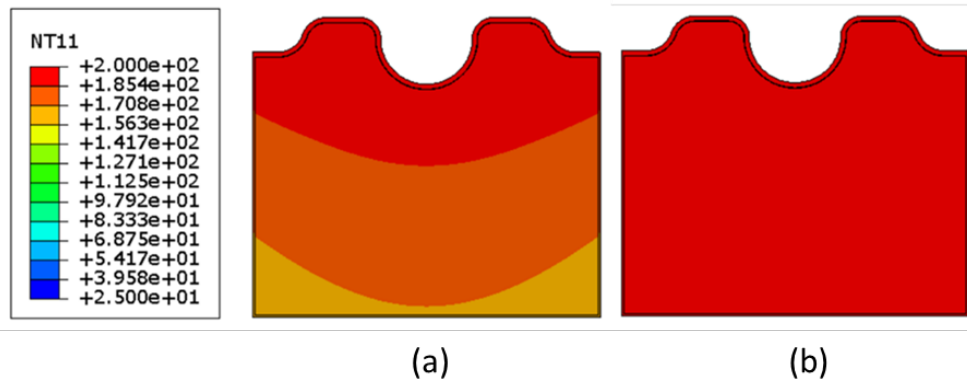
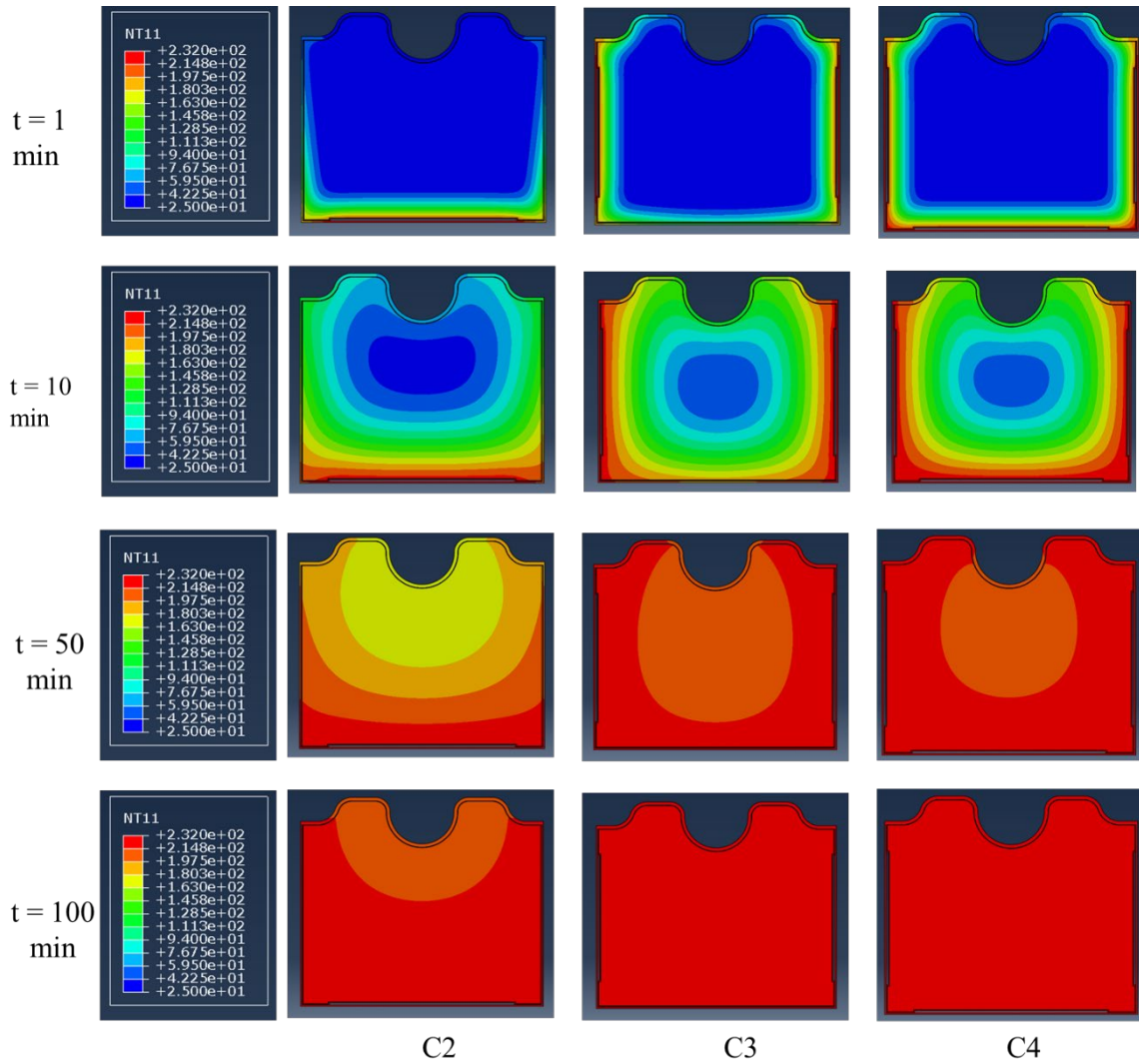


Figure 3.24: Temperature contour plots for (a) C1 and (b) C10

Figure 3.25 shows temperature evolution contours for concepts C2, C3 and C4 at time instances 1min, 10 min, 50 min and 100 min. Heat transport characteristics were seen to have improved with the increase in the number of heaters from 1 to 3. From C2-C4, a decline in time required to reach steady state was observed. Also, temperature gradient in the tool followed a decreasing trend. A very similar trend was observed in concepts C6, C7 and C8 using MICA heater. Further, temperature evolution contours for C5 is shown in Figure 3.26. Similar to C1, this concept shows a huge gradient towards the bottom of the tool owing to the poor heat transport through the CFOAM core. Concept C9 displays similar behavior as C5.



Max = 232°C, Min = 25°C OR Max = 450F, Min = 77F

Figure 3.25: Temperature evolution contours of concepts C2,C3 and C4 at t=1 min, 10 min, 50 min and 100 min

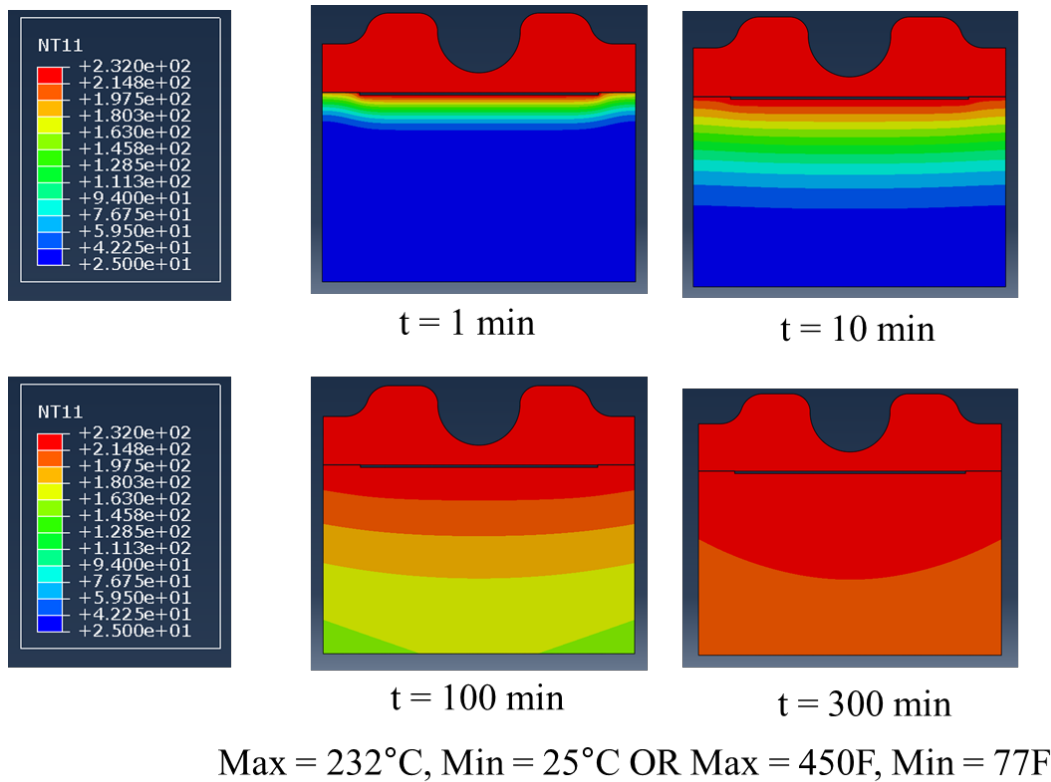


Figure 3.26: Temperature evolution contour of concept C5 at t=1 min, 10 min, 100 min and 300 min

3.4.2.4 Summary of Composite Boom tool design results

Four result types were studied for the Composite Boom tool design namely temperature uniformity on the surface of the tool, temperature drop between heater and tool surface, time required to reach steady state, temperature evolution and gradient in the tool. Considering thermal stability and energy efficiency as the determining parameters for the tool design, it was inferred that the GFOAM concepts namely C10, C11 and C12 perform much better compared to the CFOAM concepts. Further, the cure temperature requirement of epoxy based CFRP composite sheets is generally around 350F. This was

satisfied by all three GFOAM concepts. In fact, the high temperature achieved by C12 is actually not required. The C10 concept utilizes polyimide heater which is a thin flexible film. This film is sandwiched between the tool surface and GFOAM core. The use of this film requires extremely careful handling due its flimsy nature. Essentially, certain manufacturing constraints discourage the adoption of the C10 concept. Thus, we are reduced to the C11 concept which consists of GFOAM core enveloped by BMI laminate with a bottom silicone heater. The C11 concept is used further for curing simulations. The curing simulation results are presented in the next section.

3.4.3 Cure simulation results

Once the composite boom tool design was optimized, the C11 concept was used to carry out curing simulations. 2 cases were studied and the results for the same are described here. The material properties used for the curing simulations are provided in Table 3.4.

Table 3.4 Material properties used for cure analysis

Materials	Density	Thermal Conductivity		Specific Heat		Elastic modulus E (GPa)
	ρ (g/cm^3)	k ($\frac{W}{mK}$)		c_p ($\frac{J}{g^{\circ}C}$)		
Graphite Foam (GFOAM)	0.3	Temp ($^{\circ}C$) ¹	k ¹	Temp ($^{\circ}C$)	c_p	2.266
		38	13.3	38	0.755	
		93	14.2	93	0.932	
		149	14.8	149	1.086	
		250	15.3	250	1.306	
Fiber Reinforced BMI Laminate (10-ply)	1.480 ²	Temp ($^{\circ}C$) ¹	k ³	Temp ($^{\circ}C$)	c_p ⁴	57.2 ^A
		38	0.502	25	0.77	
		93	0.448			
		149	0.296	160	1.68	
		204	0.222			
A. BMI preliminary Datasheet, Aldila Composite materials						
Refer Table 3.1 for references 1, 3 and 4						

3.4.3.1 Case 1

As described in section 3.3.2, three analyses namely thermo-chemical, flow-compaction and stress-deformation were performed for thick laminated composite. The results studied from the thermo-chemical analysis are the cure profiles (temperature vs. time curves) and degree of cure at selected locations of the laminate. Two location were

selected on the composite laminate; first at the laminate center and second at the center of the top flat land of the laminate (see Figure 3.27). The cure profiles for the two locations are plotted along with the cure cycle supplied by the heater. The two cure profiles shown in Figure 3.28(a) were very consistent suggesting excellent temperature uniformity in the composite laminate. The degree of cure profiles in Figure 3.28(b) showed a maximum value of 0.9 at the end of the cure cycle indicating 90% cure of the resin. Also, the degree of cure profiles for the two locations were matching closely. This indicated uniform cure of the composite laminate.

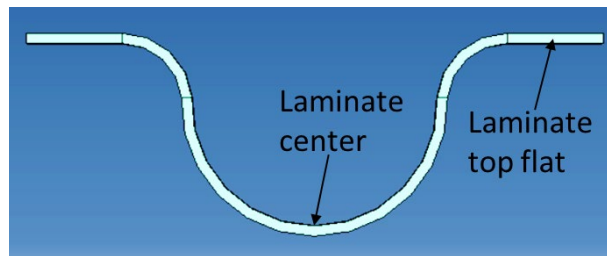


Figure 3.27: Laminate locations used for plotting cure profiles and degree of cure

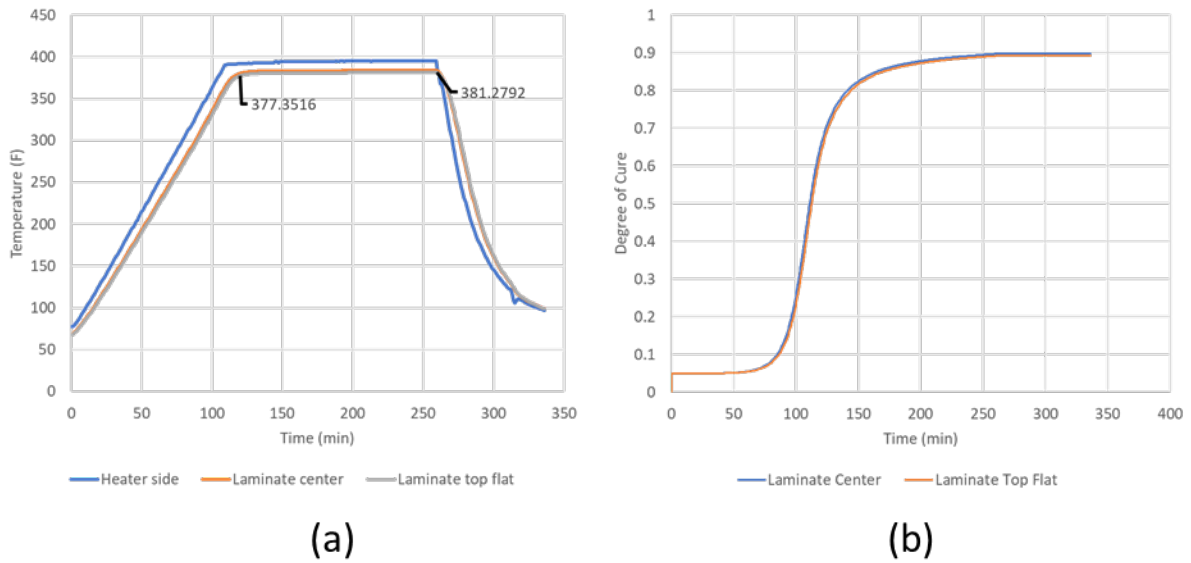


Figure 3.28: (a) Cure profiles, (b) Degree of cure curves at Laminate center and Laminate top flat locations

The temperature and degree of cure results from the thermo-chemical analysis were provided as input to the flow-compaction analysis. Thick laminates are susceptible to resin volume fraction change during the curing process leading to thinning of laminate. As a result, resin volume fraction contour was studied. Figure 3.29 shows the resin volume fraction in the composite laminate at the end of the curing process. The initial value of resin volume fraction is 0.426 which was predefined for the material used. Resin volume fraction was observed to drop in the top flat regions and increase near the center region of the laminate. This suggested a resin flow from the top flat edges towards the center of the laminate during the curing process.

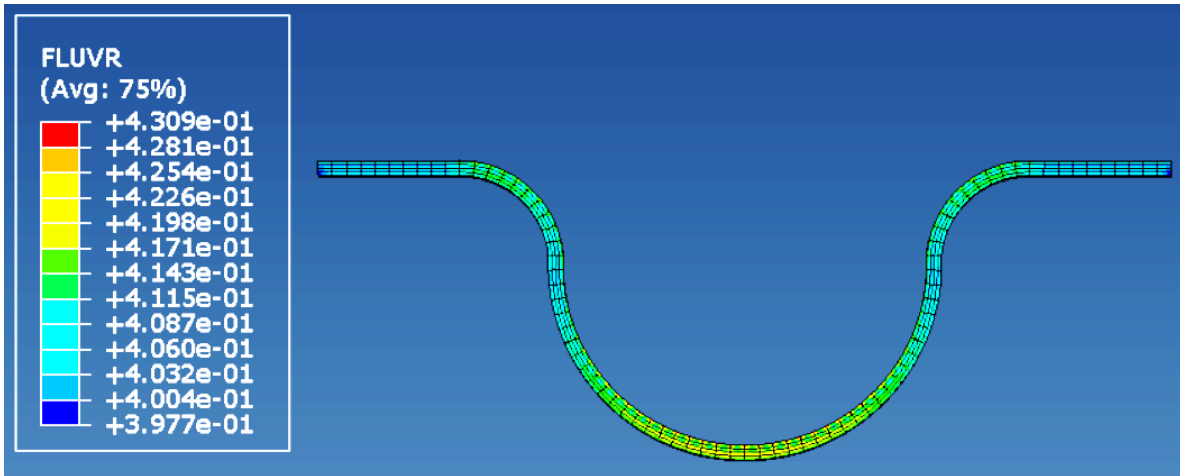


Figure 3.29: Resin volume fraction obtained at the end of Flow-compaction analysis

The temperature and degree of cure results from the thermo-chemical analysis as well as the resin-volume fraction results from the flow-compaction analysis were provided as inputs to the stress-deformation analysis. Once the curing process is completed, the upper tool is retracted, and the composite laminate is then simply resting on the lower tool. In the present analysis, the laminate was free to deform. It was only constrained in the y direction at the center of the laminate to avoid rigid body motion. Figure 3.30 shows the deformation contour plot of the laminate at the end step of stress-deformation analysis. A symmetrical deformation was observed in the laminate with a maximum displacement of 0.85 mm (contour scale in m) on the top flat regions.

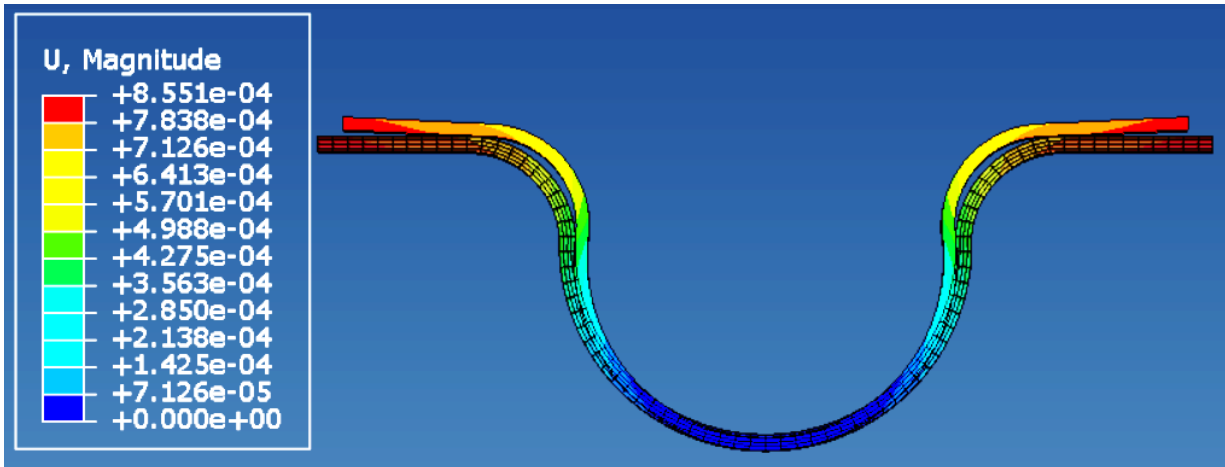


Figure 3.30: Process-induced deformation observed at the end of the stress-deformation analysis. Deformation scale factor: 5

3.4.3.2 Case 2

Results of curing analyses performed for thin-ply composite laminate are presented here. For these thin-ply composites, the resin volume fraction was assumed to be constant and as a result flow-compaction analysis was not performed. Two locations were selected on the thin-ply composite laminate similar to Case 1 for plotting results. The cure profiles at the two locations are shown in Figure 3.31(a) along with the heater cure profile plotted as reference. The two profiles were consistent suggesting uniform curing temperature in the laminate. Also, the degree of cure profiles showed good agreement (Figure 3.31(b)) and a maximum cure of 0.89 at the end of the cure cycle.

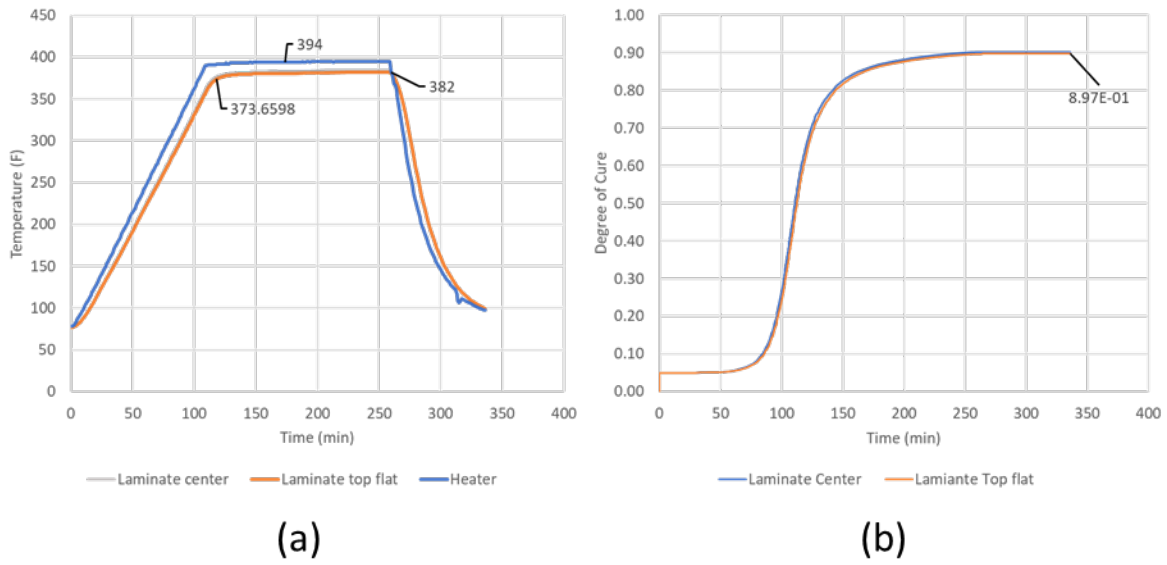


Figure 3.31: (a) Cure profiles, (b) Degree of cure curves at laminate center and laminate top flat locations for thin-ply laminate

The temperature and degree of cure results from the thermo-chemical analysis were provided as input to the stress-deformation analysis. The boundary condition applied to constrain the laminate in this case is same as Case 1. Figure 3.32 shows the deformation plot of the laminate at the end step of Stress-deformation analysis. A maximum deformation of 0.58 mm (contour scale in m) was observed on one of the top flat regions.

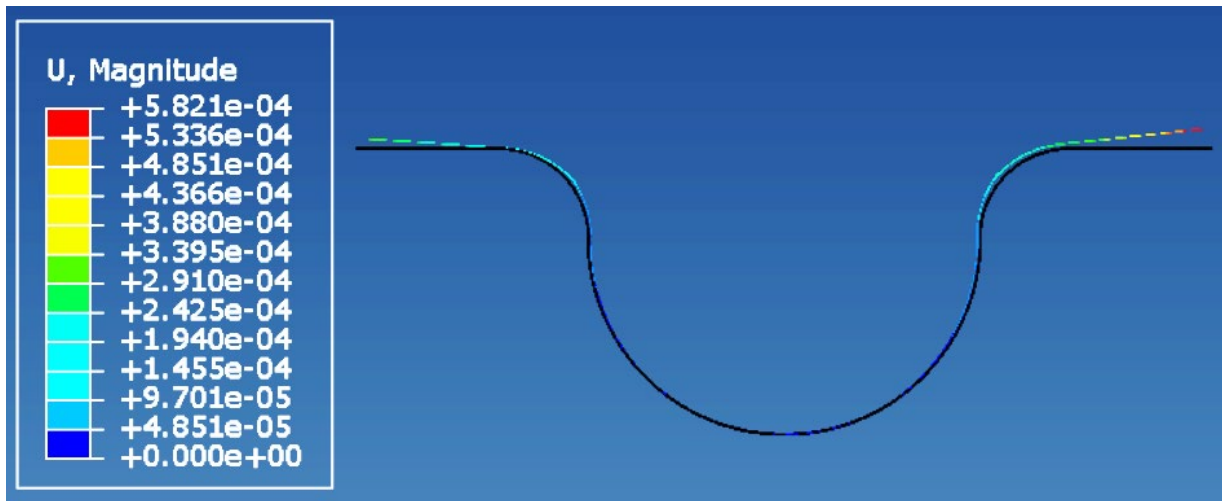


Figure 3.32: Process-induced deformation observed at the end of Stress-deformation analysis for thin-ply laminate

3.5 Conclusions and Future work

A model was developed for the Composite Boom tool to study thermal characteristics and make optimum design choice. As a first step, flat plate test data obtained experimentally was utilized to validate the plate model build for the purpose. Four cases were considered and validation results as well as possible reasons for the discrepancies between the model and test results were provided. Further, parameters of the tool affecting heat transfer characteristics namely heater locations, heat spreader and core material were identified. These parameters were thoroughly investigated by executing a design of experiment (DOE). Concept 1 was found to have the best temperature uniformity but produced a considerable thermal gradient in the tool which was undesirable. The GFOAM concepts namely C10, C11 and C12 were found to have notable advantages over their CFOAM counterparts in terms of the heat transfer time and temperature gradient. The model developed thus proved valuable for quick and reliable analysis to support the

iterative design and material selection process for the Composite Boom tool. **In summary, using tool surface temperature uniformity as the primary evaluation criterion, and taking into account several secondary factors including (1) tool manufacturing complexity, (2) robustness of the tool, (3) repair cost, (4) maximum reachable tool surface temperature, (5) time to reach steady state, (6) interior temperature gradient of the core, the GFOAM core design concept 11 was identified as optimum for the present work.** In addition, preliminary cure analysis of laminate on the Composite Boom tool was performed to study the thermal profiles as well as process-induced deformations of the composite laminate. The stress-deformation plots for both cases indicated that the curing process induced warpage in a composite laminate. This showed the significance of incorporating the curing process effects in any further testing/ mechanical analysis.

As future work, the validated 2-D heat transfer model of the DCB tool will be extended to 3-D cases. This is because the DCB tool, although having uniform geometry in the longitudinal direction, is of finite length. There is a temperature gradient in the longitudinal direction near the two ends of the tool. In addition, due to the large length of the tool, multiple tool sections are necessary, and hardware is required for joining the sections. For the same reason, as it is infeasible to have a single heater along the entire length of the tool, it is envisioned that multiple heaters will be placed along the length of the tool with gaps between them. In that case, the temperature distribution will have a periodic variation along the length of the tool. The magnitude of the temperature variation directly influences the curing process of the laminate. Therefore, 3D thermal analysis is necessary for accurately modeling the heating of the DCB tool.

Also, the curing analysis will be extended to the 3D tool geometry for the candidate designs. The effects of tool's finite length, heater distribution along the length, and the joints of the tool sections will be considered in the 3D model. The residual stress and deformation in the longitudinal direction will be evaluated. The 3D curing model will be validated through a set of experiments. The changes in fiber orientation and distribution obtained from the simulations are compared with SEM or micro-XCT images. The warpage predicted is validated using a 3D coordinate measuring machine. The predicted residual stresses are validated using the DIC hole-drilling measurements.

Additionally, the last two steps of the MTR pathway that is mapping of curing process effects and mechanical simulations will be performed. The predicted residual stresses, warpage and fiber distributions/orientations will be incorporated into the static and dynamic FE setup in ABAQUS™ and LS-DYNA, by using a mapping procedure. The last step, Step five of the MTR pathway will involve numerical evaluation of the mechanical response under the static and dynamic loading conditions which will be validated by experimental tests.

CHAPTER 4 : CONCLUSIONS

- The MTR pathways established for the two case studies provide a systematic approach for composite structure development. Implementation of these pathways will allow to 1) study manufacturing process effects on structural responses, 2) optimize the design parameters and process effects by carrying out multiple iterations or potentially automating the pathway, 3) reduce development time and improve cost effectiveness.
- In the first case study, MTR pathway was established and implemented for thermoforming process of thermoplastic based continuous CFRP hat structure. The pathway meets the critical requirements of integrating the design and manufacturing of lightweight thermoplastic composite parts by directly linking the manufacturing process effects to the mechanical responses.
- Additionally, a study of thermoforming induced large variations in process effects namely fiber orientation, thickness and residual stress was performed. Each process effect demonstrated a substantial impact on the static and dynamic performance of the hat structure. This study was representative of process effects likely to be observed in manufacturing complex automotive structures which further reinforces the need to tie together manufacturing and structural simulations.
- In the second case study, another MTR pathway was established and implemented partially for OOA molding process using self-heated tool of thermoset based CFRP composite boom structure. The curing simulation performed showed considerable

residual stress induced deformation in the composite boom structure indicating the significance of the pathway to minimize these deformations.

REFERENCES

- [1] A. K. Kaw, *Mechanics of composite materials, second edition*. 2005.
- [2] W. D. Callister and D. G. Rethwisch, *Materials Science and Engineering 9th Edition*. 2014.
- [3] D. K. Rajak, D. D. Pagar, P. L. Menezes, and E. Linul, “Fiber-reinforced polymer composites: Manufacturing, properties, and applications,” *Polymers*. 2019, doi: 10.3390/polym11101667.
- [4] T. Ozbakkaloglu, J. F. Chen, S. T. Smith, and J. G. Dai, “Applications of Fiber Reinforced Polymer Composites,” *International Journal of Polymer Science*, vol. 2016. 2016, doi: 10.1155/2016/5804145.
- [5] H. Fang, Y. Bai, W. Liu, Y. Qi, and J. Wang, “Connections and structural applications of fibre reinforced polymer composites for civil infrastructure in aggressive environments,” *Composites Part B: Engineering*, vol. 164. 2019, doi: 10.1016/j.compositesb.2018.11.047.
- [6] R. Kumar, M. I. Ul Haq, A. Raina, and A. Anand, “Industrial applications of natural fibre-reinforced polymer composites—challenges and opportunities,” *International Journal of Sustainable Engineering*, vol. 12, no. 3. 2019, doi: 10.1080/19397038.2018.1538267.
- [7] P. Beardmore and C. F. Johnson, “The potential for composites in structural automotive applications,” *Compos. Sci. Technol.*, 1986, doi: 10.1016/0266-3538(86)90002-3.
- [8] M. E. Botkin, “Modelling and optimal design of a carbon fibre reinforced composite automotive roof,” *Eng. Comput.*, 2000, doi: 10.1007/s003660050033.
- [9] S. A. Pradeep, R. K. Iyer, H. Kazan, and S. Pilla, “Automotive Applications of Plastics: Past, Present and Future,” in *Applied Plastics Engineering Handbook: Processing, Materials, and Applications*, 2nd ed., M. Kutz, Ed. Oxford: Elsevier, 2017, pp. 651–674.
- [10] I. L. Chiu, J. R. Kolb, and H. A. Newey, “EPOXY RESIN SYSTEM FOR COMPOSITE FLYWHEELS.,” *Compos. Technol. Rev.*, 1983.
- [11] M. Carello and A. G. Airale, “Composite suspension arm optimization for the city vehicle XAM 2.0,” *Adv. Struct. Mater.*, 2014, doi: 10.1007/978-3-319-07383-5_18.
- [12] D.-H. Kim, D.-H. Choi, and H.-S. Kim, “Design optimization of a carbon fiber reinforced composite automotive lower arm,” *Compos. Part B Eng.*, vol. 58, pp. 400–407, Mar. 2014, doi: 10.1016/j.compositesb.2013.10.067.
- [13] G. Zhu, Z. Wang, A. Cheng, and G. Li, “Design optimisation of composite bumper beam with variable cross-sections for automotive vehicle,” *Int. J. Crashworthiness*, vol. 22, no. 4, pp. 365–376, Jul. 2017, doi: 10.1080/13588265.2016.1267552.
- [14] A. Kothari *et al.*, “A Finite Element Design Study and Performance Evaluation of an Ultra-Lightweight Carbon Fiber Reinforced Thermoplastic Composites Vehicle Door Assembly,” in *SAE Technical Papers*, Apr. 2020, vol. 2020-April, no. April,

- doi: 10.4271/2020-01-0203.
- [15] H. Ning, U. Vaidya, G. M. Janowski, and G. Husman, “Design, manufacture and analysis of a thermoplastic composite frame structure for mass transit,” *Compos. Struct.*, 2007, doi: 10.1016/j.compstruct.2006.04.036.
 - [16] J. C. Halpin, J. L. Kardos, and M. P. Dudukovic’, “Processing science: An approach for prepreg composite systems,” *Pure Appl. Chem.*, 1983, doi: 10.1351/pac198355050893.
 - [17] H. M. EL-Dessouky and C. A. Lawrence, “Ultra-lightweight carbon fibre/thermoplastic composite material using spread tow technology,” *Compos. Part B Eng.*, vol. 50, pp. 91–97, Jul. 2013, doi: 10.1016/J.COMPOSITESB.2013.01.026.
 - [18] Z. Liu, J. Lu, and P. Zhu, “Lightweight design of automotive composite bumper system using modified particle swarm optimizer,” *Compos. Struct.*, vol. 140, pp. 630–643, Apr. 2016, doi: 10.1016/j.compstruct.2015.12.031.
 - [19] P. Bere, E. Sabău, C. Dudescu, C. Neamtu, and M. Fărtan, “Experimental research regarding carbon fiber/epoxy material manufactured by autoclave process,” *MATEC Web Conf.*, vol. 299, 2019, doi: 10.1051/mateconf/201929906005.
 - [20] A. W. Smith, K. Goyette, C. Kazanas, and P. Hubert, “Development of a heated tooling solution to improve process flexibility for out-of-autoclave prepregs,” 2013.
 - [21] H. Xiong, N. Hamila, and P. Boisse, “Consolidation modeling during thermoforming of thermoplastic composite prepregs,” *Materials (Basel)*., 2019, doi: 10.3390/ma12182853.
 - [22] A. Crosky, C. Grant, D. Kelly, X. Legrand, and G. Pearce, “Fibre placement processes for composites manufacture,” in *Advances in Composites Manufacturing and Process Design*, 2015.
 - [23] N. Jayasree, S. Omairey, and M. Kazilas, “Novel multi-zone self-heated composites tool for out-of-autoclave aerospace components manufacturing,” *Sci. Eng. Compos. Mater.*, 2020, doi: 10.1515/secm-2020-0033.
 - [24] D.-H. Kim, H.-G. Kim, and H.-S. Kim, “Design optimization and manufacture of hybrid glass/carbon fiber reinforced composite bumper beam for automobile vehicle,” *Compos. Struct.*, vol. 131, pp. 742–752, Nov. 2015, doi: 10.1016/j.compstruct.2015.06.028.
 - [25] M. Hou, K. Friedrich, and R. Scherer, “Optimization of stamp forming of thermoplastic composite bends,” *Compos. Struct.*, 1994, doi: 10.1016/0263-8223(94)90077-9.
 - [26] T. G. Donderwinkel, B. Rietman, S. P. Haanappel, and R. Akkerman, “Stamp forming optimization for formability and crystallinity,” in *AIP Conference Proceedings*, 2016, p. 170029, doi: 10.1063/1.4963585.
 - [27] G. F. Nino, O. K. Bergsma, H. E. Bersee, and A. Beukers, “Influence of fiber orientation on mechanical performance for thermoformed composites,” *ICCM Int. Conf. Compos. Mater.*, pp. 1–7, 2007.
 - [28] N. A. Jayasree, A. G. Airale, A. Ferraris, A. Messana, L. Sisca, and M. Carello, “Process analysis for structural optimisation of thermoplastic composite

- component using the building block approach,” *Compos. Part B Eng.*, vol. 126, pp. 119–132, Oct. 2017, doi: 10.1016/j.compositesb.2017.06.007.
- [29] I. Baran, K. Cinar, N. Ersoy, R. Akkerman, and J. H. Hattel, “A Review on the Mechanical Modeling of Composite Manufacturing Processes,” *Arch. Comput. Methods Eng.*, 2017, doi: 10.1007/s11831-016-9167-2.
- [30] N. Mayer, J. Prowe, T. Havar, R. Hinterhölzl, and K. Drechsler, “Structural analysis of composite components considering manufacturing effect,” *Compos. Struct.*, vol. 140, pp. 776–782, 2016, doi: 10.1016/j.compstruct.2016.01.023.
- [31] L. Kärger *et al.*, “Forming optimisation embedded in a CAE chain to assess and enhance the structural performance of composite components,” *Compos. Struct.*, vol. 192, no. January, pp. 143–152, 2018, doi: 10.1016/j.compstruct.2018.02.041.
- [32] D. Tatsuno, T. Yoneyama, K. Kawamoto, and M. Okamoto, “Hot press forming of thermoplastic CFRP sheets,” *Procedia Manuf.*, vol. 15, pp. 1730–1737, 2018, doi: 10.1016/j.promfg.2018.07.254.
- [33] C. Li, N. Zobeiry, K. Keil, S. Chatterjee, and A. Poursartip, “Advances in the characterization of residual stress in composite structures,” 2014.
- [34] N. Mayer, B. Van Den Broucke, J. Prowe, T. Havar, and R. Hinterhölzl, “Finite element mapping for incompatible FE meshes of composite structures,” *Adv. Eng. Softw.*, vol. 99, pp. 81–88, 2016, doi: 10.1016/j.advengsoft.2016.05.007.
- [35] L. Kärger *et al.*, “Development and validation of a CAE chain for unidirectional fibre reinforced composite components,” *Compos. Struct.*, vol. 132, pp. 350–358, Nov. 2015, doi: 10.1016/j.compstruct.2015.05.047.
- [36] S.-W. Hsiao and N. Kikuchi, “Numerical analysis and optimal design of composite thermoforming process,” *Comput. Methods Appl. Mech. Eng.*, vol. 177, no. 1–2, pp. 1–34, Jul. 1999, doi: 10.1016/S0045-7825(98)00273-4.
- [37] M. Rouse, D. C. Jegley, D. M. McGowan, H. G. Bush, and W. A. Waters, “Utilization of the building-block approach in structural mechanics research,” *Collect. Tech. Pap. - AIAA/ASME/ASCE/AHS/ASC Struct. Struct. Dyn. Mater. Conf.*, vol. 2, no. c, pp. 860–878, 2005, doi: 10.2514/6.2005-1874.
- [38] N. Sakundarini, Z. Taha, S. H. Abdul-Rashid, and R. A. R. Ghazila, “Optimal multi-material selection for lightweight design of automotive body assembly incorporating recyclability,” *Mater. Des.*, vol. 50, 2013, doi: 10.1016/j.matdes.2013.03.085.
- [39] G. Kopp, E. Beeh, R. Schöll, A. Kobilke, P. Straßburger, and M. Krieschera, “New Lightweight Structures for Advanced Automotive Vehicles—Safe and Modular,” *Procedia - Soc. Behav. Sci.*, vol. 48, 2012, doi: 10.1016/j.sbspro.2012.06.1015.
- [40] M. R. Seyedi *et al.*, “Vehicle crashworthiness and occupant protection,” *Int. J. Crashworthiness*, vol. 25, no. 3, 2004.
- [41] J. Cao *et al.*, “Characterization of mechanical behavior of woven fabrics: Experimental methods and benchmark results,” *Compos. Part A Appl. Sci. Manuf.*, vol. 39, no. 6, pp. 1037–1053, 2008, doi: 10.1016/j.compositesa.2008.02.016.
- [42] P. Harrison, J. Wiggers, and A. C. Long, “Normalization of shear test data for rate-independent compressible fabrics,” *J. Compos. Mater.*, vol. 42, no. 22, pp. 2315–2344, 2008, doi: 10.1177/0021998308095367.

- [43] G. Lebrun, M. N. Bureau, and J. Denault, “Evaluation of bias-extension and picture-frame test methods for the measurement of intraply shear properties of PP/glass commingled fabrics,” *Compos. Struct.*, vol. 61, no. 4, pp. 341–352, 2003, doi: 10.1016/S0263-8223(03)00057-6.
- [44] ASM International Handbook Committee, *ASM Handbook Vol. 2: Properties and selection--nonferrous alloys and special-purpose materials*. 2001.
- [45] “Radioss, Reference guide, starter input, interfaces, penalty method, /INTER/TYPE 21.” .
- [46] M. A. Khan, T. Mabrouki, E. Vidal-Sallé, and P. Boisse, “Numerical and experimental analyses of woven composite reinforcement forming using a hypoelastic behaviour. Application to the double dome benchmark,” *J. Mater. Process. Technol.*, vol. 210, no. 2, pp. 378–388, 2010, doi: 10.1016/j.jmatprotec.2009.09.027.
- [47] P. Harrison, R. Gomes, and N. Curado-Correia, “Press forming a 0/90 cross-ply advanced thermoplastic composite using the double-dome benchmark geometry,” *Compos. Part A Appl. Sci. Manuf.*, vol. 54, pp. 56–69, Nov. 2013, doi: 10.1016/j.compositesa.2013.06.014.
- [48] X. Peng, Z. Guo, T. Du, and W. R. Yu, “A simple anisotropic hyperelastic constitutive model for textile fabrics with application to forming simulation,” *Compos. Part B Eng.*, vol. 52, pp. 275–281, 2013, doi: 10.1016/j.compositesb.2013.04.014.
- [49] P. Boisse, A. Gasser, B. Hagege, and J. L. Billoet, “Analysis of the mechanical behavior of woven fibrous material using virtual tests at the unit cell level,” 2005, doi: 10.1007/s10853-005-5069-7.
- [50] W. R. Yu, F. Pourboghrat, K. Chung, M. Zampaloni, and T. J. Kang, “Non-orthogonal constitutive equation for woven fabric reinforced thermoplastic composites,” *Compos. Part A Appl. Sci. Manuf.*, 2002, doi: 10.1016/S1359-835X(02)00053-2.
- [51] X. Q. Peng and J. Cao, “A continuum mechanics-based non-orthogonal constitutive model for woven composite fabrics,” *Compos. Part A Appl. Sci. Manuf.*, 2005, doi: 10.1016/j.compositesa.2004.08.008.
- [52] P. P. Parlevliet, H. E. N. Bersee, and A. Beukers, “Residual stresses in thermoplastic composites—A study of the literature—Part I: Formation of residual stresses,” *Compos. Part A Appl. Sci. Manuf.*, vol. 37, no. 11, pp. 1847–1857, Nov. 2006, doi: 10.1016/j.compositesa.2005.12.025.
- [53] P. P. Parlevliet, H. E. N. Bersee, and A. Beukers, “Residual stresses in thermoplastic composites-A study of the literature-Part II: Experimental techniques,” *Composites Part A: Applied Science and Manufacturing*. 2007, doi: 10.1016/j.compositesa.2006.07.002.
- [54] P. P. Parlevliet, H. E. N. Bersee, and A. Beukers, “Residual stresses in thermoplastic composites - a study of the literature. Part III: Effects of thermal residual stresses,” *Compos. Part A Appl. Sci. Manuf.*, 2007, doi: 10.1016/j.compositesa.2006.12.005.
- [55] J. A. Barnes and G. E. Byerly, “The formation of residual stresses in laminated

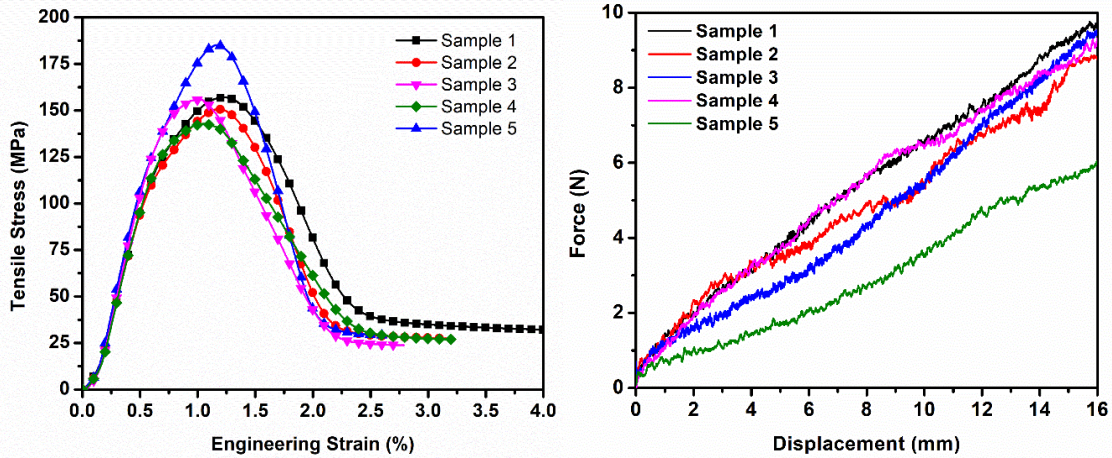
- thermoplastic composites,” *Compos. Sci. Technol.*, vol. 51, no. 4, pp. 479–494, 1994, doi: 10.1016/0266-3538(94)90081-7.
- [56] R. J. Young, R. J. Day, M. Zakikhani, and I. M. Robinson, “Fibre deformation and residual thermal stresses in carbon fibre reinforced PEEK,” *Compos. Sci. Technol.*, vol. 34, no. 3, pp. 243–258, 1989, doi: 10.1016/0266-3538(89)90031-6.
- [57] J. A. Nairn and P. Zoller, “Matrix solidification and the resulting residual thermal stresses in composites,” *J. Mater. Sci.*, vol. 20, no. 1, pp. 355–367, Jan. 1985, doi: 10.1007/BF00555929.
- [58] K. D. Cowley and P. W. R. Beaumont, “The measurement and prediction of residual stresses in carbon-fibre/polymer composites,” *Compos. Sci. Technol.*, vol. 57, no. 11, pp. 1445–1455, 1997, doi: 10.1016/S0266-3538(97)00048-1.
- [59] G. Jeronimidis and A. T. Parkyn, “Residual Stresses in Carbon Fibre-Thermoplastic Matrix Laminates,” *J. Compos. Mater.*, vol. 22, no. 5, pp. 401–415, May 1988, doi: 10.1177/002199838802200502.
- [60] C. Wang and C. T. Sun, “Thermoelastic Behavior of PEEK Thermoplastic Composite during Cooling from Forming Temperatures,” *J. Compos. Mater.*, vol. 31, no. 22, pp. 2230–2248, Nov. 1997, doi: 10.1177/002199839703102201.
- [61] J. A. E. Manson and J. C. Seferis, “Process Simulated Laminate (PSL) : A Methodology to Internal Stress Characterization in Advanced Composite Materials,” *J. Compos. Mater.*, 1992, doi: 10.1177/002199839202600305.
- [62] T. J. Chapman, J. W. Gillespie, R. B. Pipes, J.-A. E. Manson, and J. C. Seferis, “Prediction of Process-Induced Residual Stresses in Thermoplastic Composites,” *J. Compos. Mater.*, vol. 24, no. 6, pp. 616–643, Jun. 1990, doi: 10.1177/002199839002400603.
- [63] T. A. Bogetti and J. W. Gillespie, “Process-Induced Stress and Deformation in Thick-Section Thermoset Composite Laminates,” *J. Compos. Mater.*, vol. 26, no. 5, pp. 626–660, 1992, doi: 10.1177/002199839202600502.
- [64] Y. Weitsman, “RESIDUAL THERMAL STRESSES DUE TO COOL-DOWN OF EPOXY-RESIN COMPOSITES.,” *J. Appl. Mech. Trans. ASME*, 1979, doi: 10.1115/1.3424606.
- [65] B. Engel and J. Böcking, “Bending of fibre-reinforced thermoplastic tubes,” *ICCM Int. Conf. Compos. Mater.*, vol. 2015-July, no. October, 2015.
- [66] R. M. Jones, *Mechanics of Composite Materials Jones 1999*. 1999.
- [67] J. M. Whitney, *Structural Analysis Of Laminated Anisotropic Plates*. Routledge, 2018.
- [68] Y. Fung, P. Tong, and S. Bechtel, “Classical and Computational Solid Mechanics,” *Appl. Mech. Rev.*, vol. 56, no. 1, pp. B1–B2, Jan. 2003, doi: 10.1115/1.1523351.
- [69] A. Matzenmiller, J. Lubliner, and R. L. Taylor, “A constitutive model for anisotropic damage in fiber-composites,” *Mech. Mater.*, 1995, doi: 10.1016/0167-6636(94)00053-0.
- [70] Z. Hashin, “Failure criteria for unidirectional fiber composites,” *J. Appl. Mech. Trans. ASME*, 1980, doi: 10.1115/1.3153664.
- [71] J. Hallquist, *LS-DYNA® theory manual*. 2006.
- [72] S. Hashemi, A. Kinloch, and G. Williams, “Mixed-Mode Fracture in Fiber-

- Polymer Composite Laminates,” in *Composite Materials: Fatigue and Fracture (Third Volume)*, 2009.
- [73] F. K. Chang and K. Y. Chang, “A Progressive Damage Model for Laminated Composites Containing Stress Concentrations,” *J. Compos. Mater.*, vol. 21, no. 9, 1987, doi: 10.1177/002199838702100904.
- [74] S. Boria, S. Pettinari, F. Giannoni, and G. Cosimi, “Analytical and numerical analysis of composite impact attenuators,” *Compos. Struct.*, vol. 156, 2016, doi: 10.1016/j.compstruct.2015.09.032.
- [75] P. Feraboli, B. Wade, F. Deleo, M. Rassaian, M. Higgins, and A. Byar, “LS-DYNA MAT54 modeling of the axial crushing of a composite tape sinusoidal specimen,” *Compos. Part A Appl. Sci. Manuf.*, vol. 42, no. 11, 2011, doi: 10.1016/j.compositesa.2011.08.004.
- [76] P. Feraboli *et al.*, “Predictive modeling of an energy-absorbing sandwich structural concept using the building block approach,” *Compos. Part A Appl. Sci. Manuf.*, vol. 41, no. 6, 2010, doi: 10.1016/j.compositesa.2010.02.012.
- [77] J. M. Fernandez *et al.*, “An advanced composites-based solar sail system for interplanetary small satellite missions,” 2018, doi: 10.2514/6.2018-1437.
- [78] J. M. Fernandez, “Advanced Deployable Shell-Based Composite Booms For Small Satellite Structural Applications Including Solar Sails,” *Int. Symp. Sol. Sail.*, 2017.
- [79] F. Y. C. Boey and S. W. Lye, “Void reduction in autoclave processing of thermoset composites. Part 1: High pressure effects on void reduction,” *Composites*, 1992, doi: 10.1016/0010-4361(92)90186-X.
- [80] T. L. Bergman, A. S. Lavine, F. P. Incropera, and D. P. DeWitt, “Fundamentals of heat and mass transfer, 2011,” *USA John Wiley Sons. ISBN*, 2015.
- [81] Z. Bi, “Applications—Heat Transfer Problems,” in *Finite Element Analysis Applications*, 2018.
- [82] ABAQUS, “Abaqus Analysis User Manual, Version 6.14,” *Dassault Syst. Simulia Corp; ABAQUS Inc.*, 2014.
- [83] COMPRO, “COMPRO modeling guidelines,” *Converg. Manuf. Technol.*
- [84] A. a Johnston, “An integrated model of the development of process-induced deformation in autoclave processing of composite structures,” 1997.
- [85] P. Hubert, “Aspects of flow and compaction of laminated composite shapes during cure,” *Ph.D. Thesis*, 1996.

APPENDICES

Appendix A

A1. High Temperature tensile and shear plots

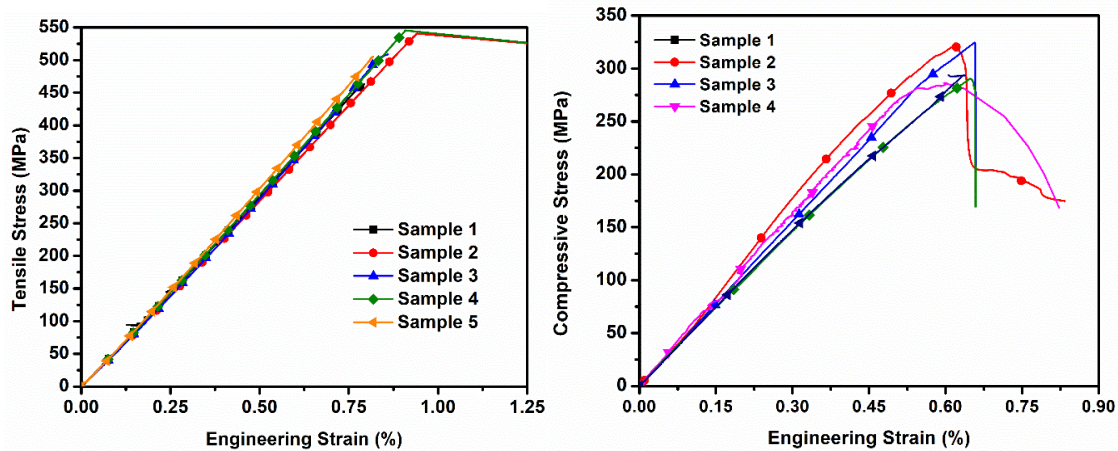


(a)

(b)

Figure A-1: (a) Experimental tensile load-displacement curves of PA6/Woven CF 0/90° orientation at 264 °C, (b) Experimental bias-extension load-displacement curves of PA6/Woven CF 45° orientation at 264 °C

A2. Room temperature tensile, compression and shear plots



(a)

(b)

Figure A-2: (a) Experimental tensile stress-strain curves of PA6/Woven CF 0/90° orientation at RT, (b) Experimental compressive stress-strain curves 0/90° orientation at RT.

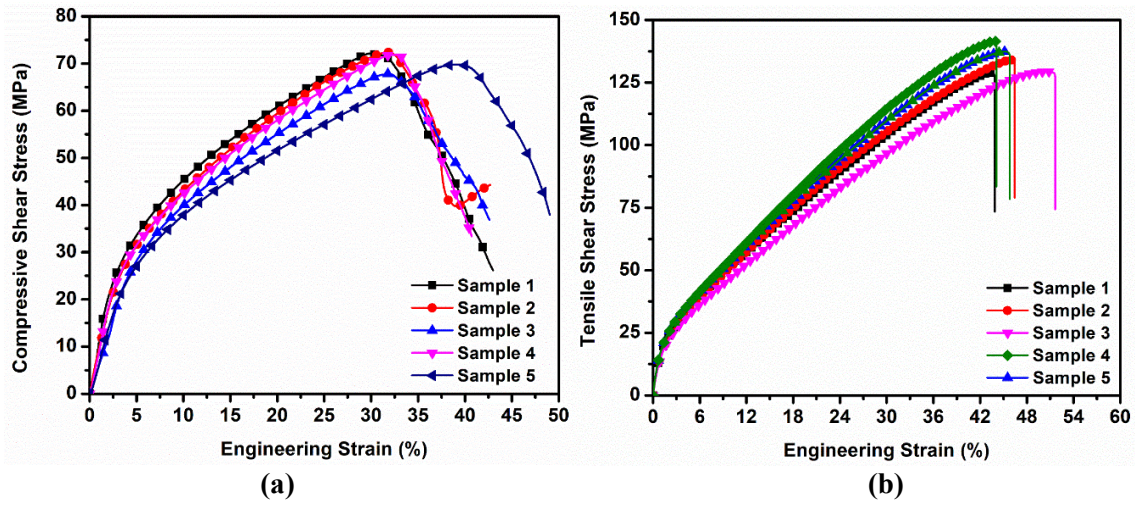

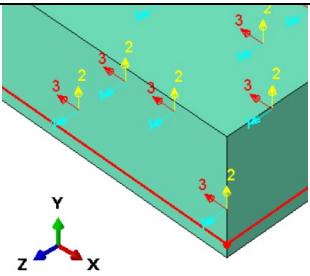


Figure A-3: (a) Experimental tensile shear stress-strain curves of PA6/Woven CF 45° orientation at RT, (b) Experimental compressive shear stress-strain curves 45° orientation at RT.

Appendix B

Table B-1 Modeling details of Flat plate 3D transient heat transfer analysis. Case CFOAM+SS400+BMI is considered here. The other cases can be modeled following the same procedure.

Analysis step	Heat transfer	Region
Part type	Flat plate: 3D deformable Flat plate partitions: CFOAM (1") + SS400 (0.25mm) +BMI Lmainate (3mm)	 <p style="text-align: center;">Set created for CFOAM, SS400 and BMI laminate</p>
Section	<p><u>CFOAM:</u></p> <p>Solid, Homogeneous</p> <p>Material: isotropic (Refer Table 3.1)</p> <p><u>BMI Laminate:</u></p> <p>Solid, Homogeneous</p> <p>Material: isotropic (Refer Table 3.1)</p> <p><u>SS400:</u></p> <p>Solid, Homogeneous</p>	

	Material: orthotropic (Refer Table 3.1)	
Element Type	<u>GFOAM core, BMI Laminate, SS400:</u> C3D8, Standard, Linear, 8 node linear brick	
Material orientation	SS400 set: Create Local coordinate system (1,2,3): 1- axis along Z, 2-axis along Y and 3-axis along X.	
Step details	Heat transfer, Transient, Time period = 16140 sec <u>Incrementation:</u> Automatic, Maximum number of increments: 1e5, Increment size: Initial=0.1, Minimum=0.00001, Maximum=100, Max. allowable temperature change per increment: 10, All other parameters = default	

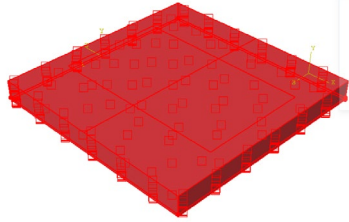
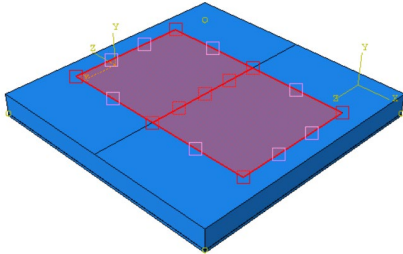
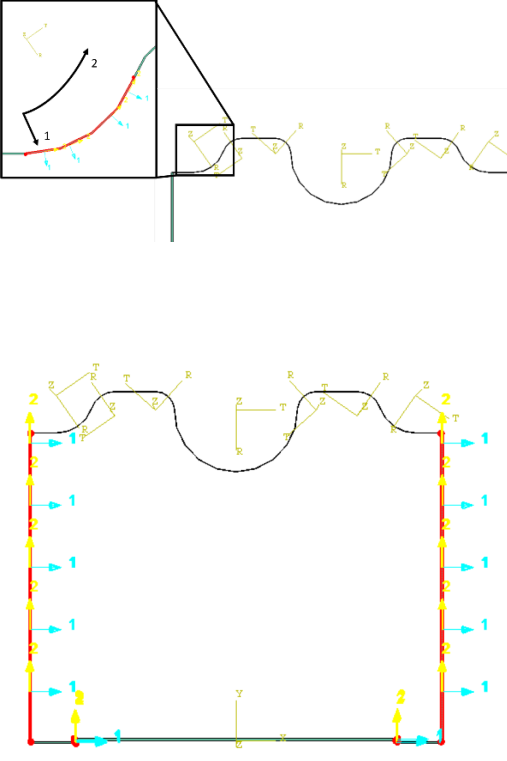
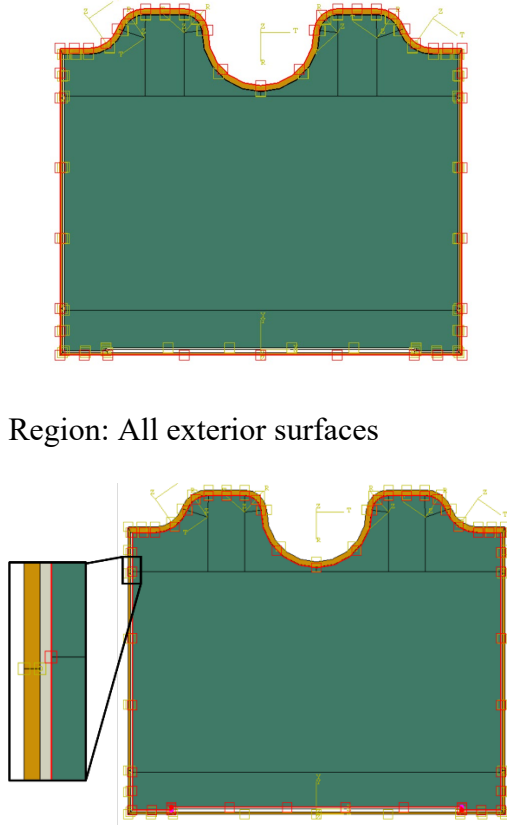
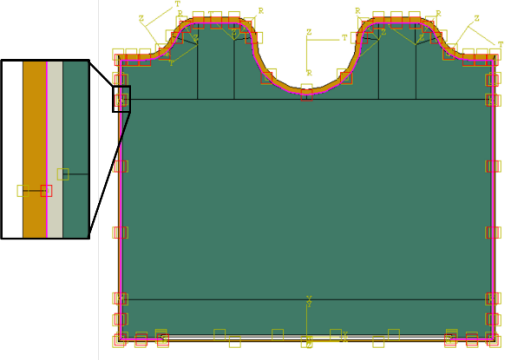
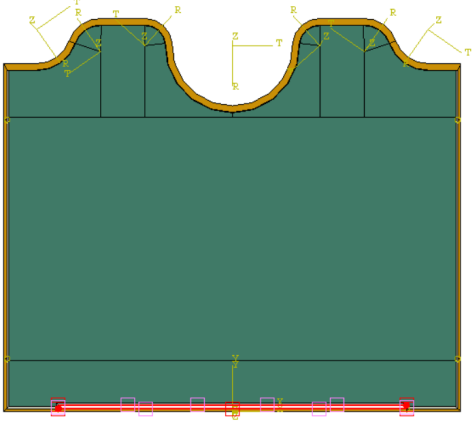
Interaction	<p>Surface film condition:</p> <p>Film</p> <p>coefficient=$1.5\text{W/m}^2\text{K}$,</p> <p>Sink temp=20°C</p>	 <p>Region: All exterior surfaces</p>
Boundary conditions	<p>Temperature: Magnitude = 1</p> <p>Amplitude: Heater center thermal profile (See figure)</p>	 <p>Region: Heater location (6''*10'') set</p>
Initial condition	Predefined field: Step-Initial	Region: CFOAM set, BMI set and SS400 set.
Field output, History output	Default	
Analysis run	Create job→Submit job	

Table B-2 Modeling details of Composite Boom tool 2D heat transfer analysis. C2 concept is considered here for description. However, following the provided procedure, any concept can be modeled.

Analysis step	Heat transfer	Region
Part type	CFOAM, BMI Laminate, Heat spreader (SS400): 2D planar, deformable, shell	
Section	<p><u>CFOAM:</u></p> <p>Solid, Homogeneous</p> <p>Plain stress/strain thickness = 1</p> <p>Material: isotropic (Refer Table 3.1)</p> <p><u>BMI Laminate:</u></p> <p>Solid, Homogeneous</p> <p>Plain stress/strain thickness = 1</p> <p>Material: isotropic (Refer Table 3.1)</p> <p><u>SS400:</u></p> <p>Solid, Homogeneous</p> <p>Plain stress/strain thickness = 1</p> <p>Material: orthotropic (Refer Table 3.1)</p>	

<p>Material orientation</p>	<p>SS400 set:</p> <p>1. Create cylindrical Datum CSYS for each curved segment (R,T,Z): R-axis along radius, T-axis tangent to curve, and Z-axis out of plane of part.</p> <p>Material orientation: 1-axis normal to curved path, 2-axis along curved path.</p> <p>1. Create rectangular Datum CSYS for straight segments (X,Y,Z)</p> <p>Material orientation: 1-axis in through-thickness direction, 2-axis in-plane direction</p>	 <p>Region: SS400 set</p>
<p>Step details</p>	<p>Heat transfer, Transient, Time period = 26000 sec</p> <p><u>Incrementation:</u> Automatic,</p> <p>Maximum number of increments: 1e6, Increment size: Initial=0.1, Minimum=3e-6, Maximum=120,</p>	

	<p>End step when temperature change is less than = 0.0001, Max. allowable temperature change per increment: 10, All other parameters = default</p>	
<p>Interaction</p>	<p>1. Surface film condition: Film coefficient=$1.5\text{W/m}^2\text{K}$, Sink temp=25°C</p> <p>1. Surface-to-surface contact Master surface: CFOAM outer surface Slave surface: SS400 inner surface (Refer figure)</p> <p>2. Surface-to-surface contact Master surface: SS400 outer surface</p>	 <p>Region: All exterior surfaces</p>

	<p>Slave surface: BMI laminate inner surface (Refer figure)</p> <p>Contact interaction property: Thermal conductance, tabular (common to 2. And 3.)</p> <table border="1" data-bbox="414 682 836 819"> <thead> <tr> <th>Conductance</th> <th>Clearance</th> </tr> </thead> <tbody> <tr> <td>0.263</td> <td>0</td> </tr> <tr> <td>0</td> <td>0.01</td> </tr> </tbody> </table>	Conductance	Clearance	0.263	0	0	0.01	
Conductance	Clearance							
0.263	0							
0	0.01							
<p>Boundary conditions</p>	<p>Temperature: Magnitude = 232°C</p>	 <p>Region: Set of four heater edges</p>						
<p>Initial condition</p>	<p>Predefined field: Step-Initial</p>	<p>Region: CFOAM set, BMI set and SS400 set.</p>						
<p>Field output,</p>	<p>Default</p>							

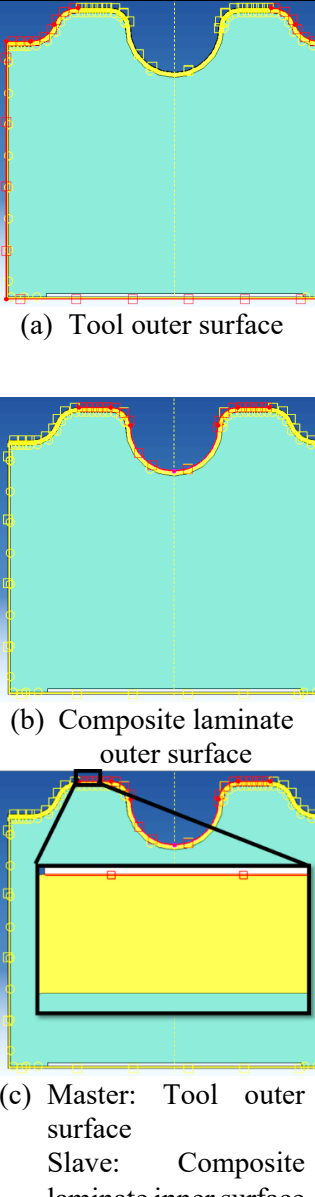
History output		
Analysis run	Create job→Submit job	

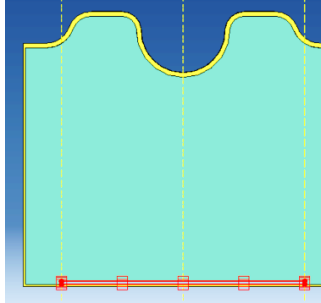

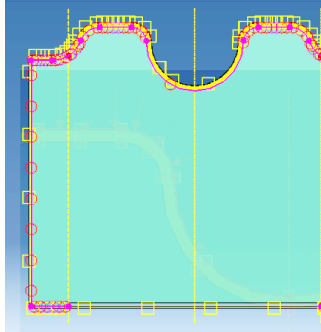
Table B-3 Modeling details of Curing analysis

I. Thermo-chemical analysis

Analysis step	Thermo-chemical	Region
Part type	<u>GFOAM core</u> : 3D deformable <u>BMI Tool</u> : 3D deformable <u>Composite laminate</u> : 3D deformable Note: depth = Refer to section thickness of individual cases.	
Section	<u>GFOAM core</u> : Solid, Homogeneous Material: GFOAM <u>BMI Tool</u> : Solid, Homogeneous Material: Fiber reinforced BMI <u>Composite Laminate</u> :	

	<p>Solid, Composite</p> <p>Material: COMPRO plugin → Materials→Composite→Hexcel_8552_AS4_Tape_Open</p> <p>Element relative thickness: 1, Orientation angle: 0° or 45° based on the case, Integration points: 5</p>	
Material Properties	<p><u>GFOAM core:</u></p> <p>Refer Table 3.4, row 2</p> <p><u>BMI Tool:</u></p> <p>Refer Table 3.4, row 3</p>	
Element Type	<p><u>GFOAM core, BMI Tool, Composite laminate:</u></p> <p>C3D20, Standard, Quadratic, 20 node quadratic brick</p>	
Step details	<p>COMPRO plugin → Analysis steps →Thermo-chemical</p> <p>Heat transfer, Transient, Time period = 20160 sec</p> <p><u>Incrementation:</u> Automatic, Maximum number of increments: 6e5, Increment size: Initial=1, Minimum=0.0001, Maximum=1000, Max.</p>	

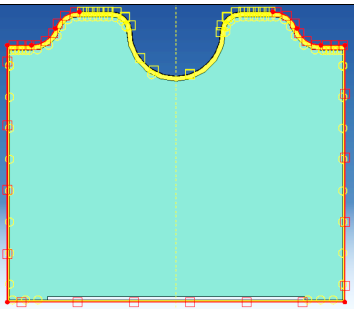
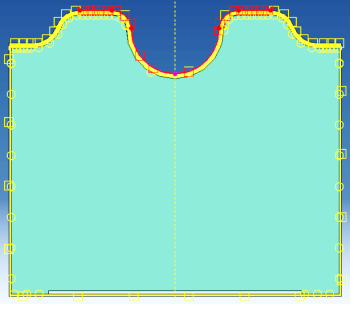
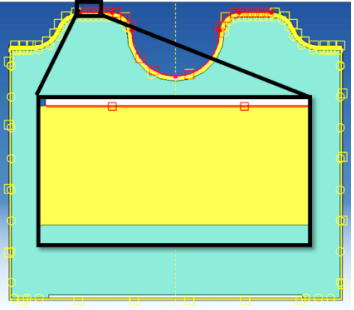
	allowable temperature change per increment: 10, All other parameters = default	
Interactions (See edges/surfaces highlighted in red in the adjacent figures)	<ol style="list-style-type: none"> <u>Surface film condition</u> Region: (a) Tool surface, (b) Composite laminate: Film coefficient=$1.5\text{W/m}^2\text{K}$, Sink temp=20°C <u>Surface-to-surface contact:</u> Region- Composite laminate (Slave surface) and Tool (Master surface) (Refer (c)): Interaction property- a) Tangential behavior: Friction Coeff. = 0.15 b) Normal behavior: Hard contact All the other parameters = default 	 <p>(a) Tool outer surface</p> <p>(b) Composite laminate outer surface</p> <p>(c) Master: Tool outer surface Slave: Composite laminate inner surface</p>

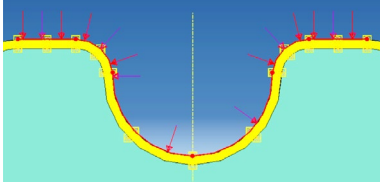
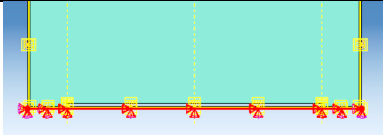
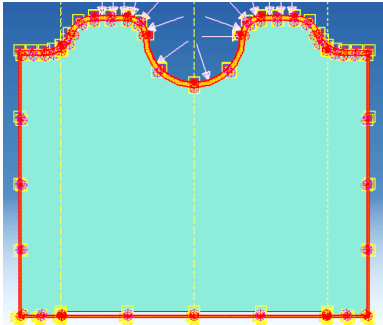
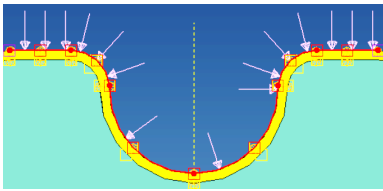
Boundary conditions	<p>1. Temperature: Magnitude = 1</p> <p>Amplitude: Cure cycle (See figure)</p>	 <p>Set: Outer 3 edges  of GFOAM and Inner bottom edge of Tool</p>
Constraint	<p>Type: Tie</p> <p>Master surface: GFOAM outer surface</p> <p>Slave surface: Tool inner surface (Refer figure)</p>	 <p>(Region: See surfaces in pink and red colors)</p>
Initial condition	<p>Predefined field: Step-Initial, Region</p>	<p>All components</p>
Field output, History output	<p>Default</p>	

Analysis run	COMPRO plugin → Analysis→Run thermo-chemical analysis, Use predefined fiber/resin volume fraction field→Submit job	
--------------	--	--

II. Flow-compaction analysis

Analysis step	Flow-compaction	Region
Step details	<p>COMPRO plugin → Analysis steps →Flow-compaction</p> <p>Type: Soils, Transient consolidation, Time period = 20160 sec</p> <p><u>Incrementation:</u> Automatic,</p> <p>Maximum number of increments: 6e5, Increment size: Initial=0.1, Minimum=1e-6, Maximum-1000, Max. pore pressure change per increment: 1e5, All other parameters = default</p>	

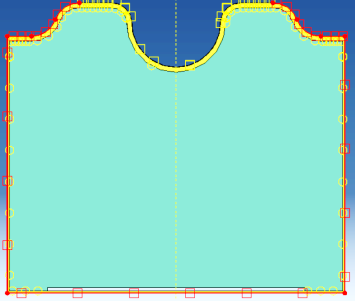
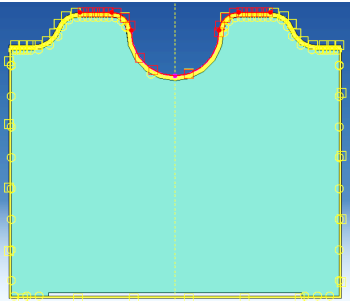
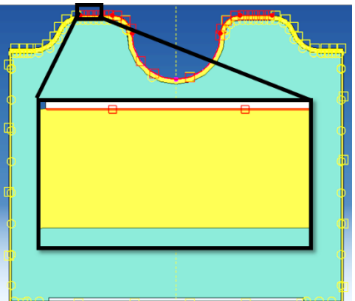
<p>Interactions</p> <p>(See edges/surfaces highlighted in red in the adjacent figures)</p>	<p>1. <u>Surface film condition</u> <u>(deactivated)</u></p> <p>Region: (a) Tool surface, (b) Composite laminate: Film coefficient=$1.5W/m^2K$, Sink temp=$20^{\circ}C$</p> <p>2. <u>Surface-to-surface</u> <u>contact:</u> <u>(modified)</u></p> <p>Region- Composite laminate (Slave surface) and Tool (Master surface) (Refer (c)):</p> <p>Interaction property-</p> <p>c) Tangential behavior: Friction Coeff. = 0.15</p> <p>d) Normal behavior: Hard contact</p> <p>All the other parameters = default</p>	 <p>(d) Tool outer surface</p>  <p>(e) Composite laminate outer surface</p>  <p>(f) Master: Tool outer surface Slave: Composite laminate inner surface</p>
--	---	--

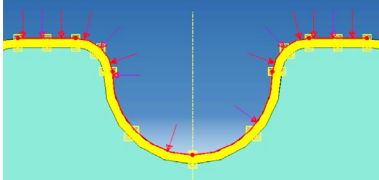
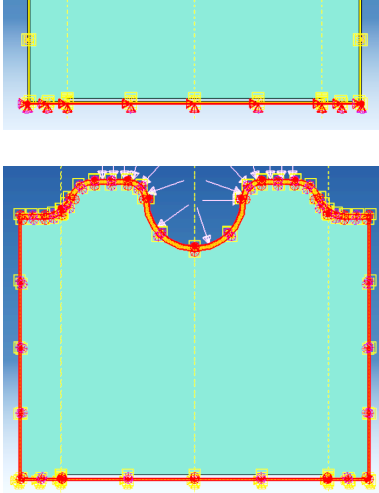
<p>Load</p>	<p>Type: Pressure, Region: Laminate upper surface (see Figure) Magnitude=1 Amplitude:</p> <table border="1" data-bbox="532 768 886 1003"> <thead> <tr> <th>Time (sec)</th> <th>Pressure (Pa)</th> </tr> </thead> <tbody> <tr> <td>0</td> <td>0</td> </tr> <tr> <td>6600</td> <td>96500</td> </tr> <tr> <td>15480</td> <td>96500</td> </tr> <tr> <td>20160</td> <td>0</td> </tr> </tbody> </table>	Time (sec)	Pressure (Pa)	0	0	6600	96500	15480	96500	20160	0	
Time (sec)	Pressure (Pa)											
0	0											
6600	96500											
15480	96500											
20160	0											
<p>Boundary conditions</p>	<p>1. Type: Displacement/Rotation Region: refer figure $U_1=U_2=0$</p> <p>2. Type: Displacement/Rotation Region: refer figure $U_3=0$</p>	  <p>Region: Laminate Set, Tool set and GFOAM set</p> 										

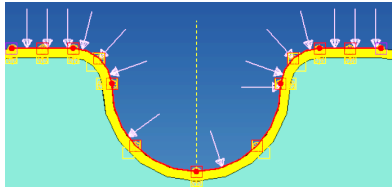
	3. Type: Pore pressure Magnitude=0	Region: Laminate upper surface set
Initial condition	Predefined field: Step-Initial, Region (Propagated)	All components
Field output, History output	Default	
Analysis run	COMPRO plugin → Analysis→Use thermo-chemical results→Upload .odb file, Run flow-compaction analysis→Submit job	

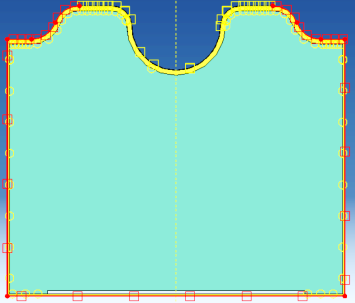
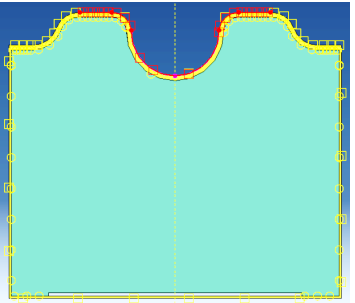
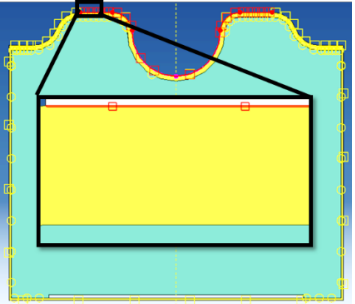
III. Stress-deformation analysis

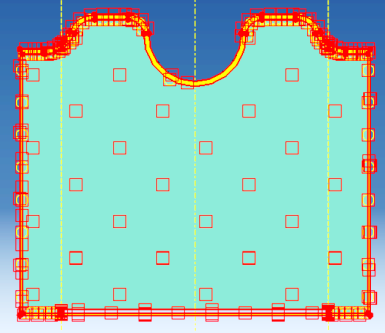
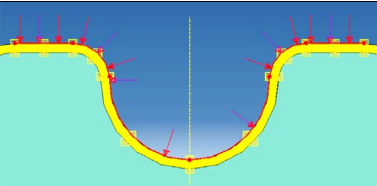
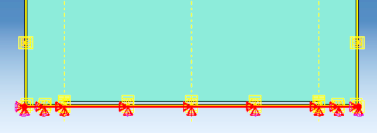
Analysis step	Stress-deformation	Region
Step details	COMPRO plugin → Analysis steps →Stress-deformation Type: Static, General Time period = 20160 sec	

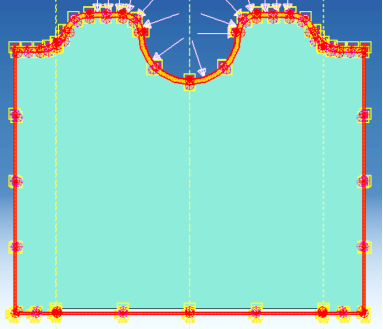
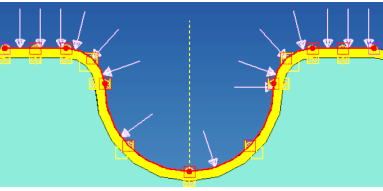
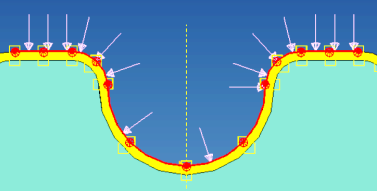
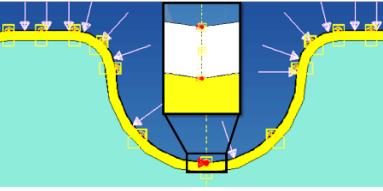
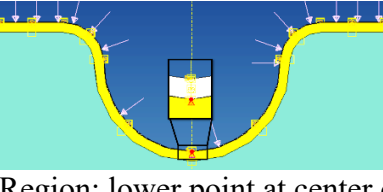
	<p>Incrementation: <u>Automatic</u>,</p> <p>Maximum number of increments: 6e5, Increment size: Initial=0.1, Minimum=0.1, Maximum=2000,</p> <p>All other parameters = default</p>	
<p>Interactions</p> <p>(See edges/surfaces highlighted in red in the adjacent figures)</p>	<p>1. <u>Surface film condition</u> (deactivated)</p> <p>Region: (a) Tool surface, (b) Composite laminate: Film coefficient=1.5W/m²K, Sink temp=20°C</p> <p>2. <u>Surface-to-surface contact</u>: (propagated)</p> <p>Region- Composite laminate (Slave surface) and Tool (Master surface) (Refer (c)):</p> <p>Interaction property-</p> <p>e) Tangential behavior: Friction Coeff. = 0.15</p>	 <p>(g) Tool outer surface</p>  <p>(h) Composite laminate outer surface</p>  <p>(i) Master: Tool outer surface Slave: Composite laminate inner surface</p>

	<p>f) Normal behavior: Hard contact</p> <p>All the other parameters = default</p>											
<p>Load</p>	<p>(Propagated) Type: Pressure, Region: Laminate upper surface (see Figure)</p> <p>Magnitude=1</p> <p>Amplitude:</p> <table border="1" data-bbox="506 1037 859 1270"> <thead> <tr> <th>Time (sec)</th> <th>Pressure (Pa)</th> </tr> </thead> <tbody> <tr> <td>0</td> <td>0</td> </tr> <tr> <td>6600</td> <td>96500</td> </tr> <tr> <td>15480</td> <td>96500</td> </tr> <tr> <td>20160</td> <td>0</td> </tr> </tbody> </table>	Time (sec)	Pressure (Pa)	0	0	6600	96500	15480	96500	20160	0	
Time (sec)	Pressure (Pa)											
0	0											
6600	96500											
15480	96500											
20160	0											
<p>Boundary conditions</p>	<p>1. Type: Displacement/Rotation</p> <p>Region: refer figure</p> <p>$U1=U2=0$</p> <p>(propagated)</p>	 <p>Region: Laminate Set, Tool set and GFOAM set</p>										

	<p>3. Type: Displacement/Rotation Region: refer figure $U_3=0$ (propagated)</p> <p>4. Type: Pore pressure Magnitude=0 (propagated)</p>	 <p>Region: Laminate upper surface set</p>
Initial condition	<p>Predefined field: Step-Initial, Region (Propagated)</p>	All components
Analysis step	Tool-removal	Region
Step details	<p>Type: Static, General Time period = 1 sec <u>Incrementation:</u> Automatic, Maximum number of increments: 6e5, Increment size: Initial=1, Minimum=1, Maximum=1, All other parameters = default</p>	

<p>Interactions</p> <p>(See edges/surfaces highlighted in red in the adjacent figures)</p>	<p>1. <u>Surface film condition</u> <u>(deactivated)</u> Region: (a) Tool surface, (b) Composite laminate: Film coefficient=$1.5W/m^2K$, Sink temp=$20^{\circ}C$</p> <p>2. <u>Surface-to-surface contact:</u> <u>(deactivated)</u> Region- Composite laminate (Slave surface) and Tool (Master surface) (Refer (c)):</p> <p>Interaction property-</p> <p>g) Tangential behavior: Friction Coeff. = 0.15</p> <p>h) Normal behavior: Hard contact All the other parameters = default</p> <p>3. Type: Model change, Definition: Region, Region</p>	 <p>(j) Tool outer surface</p>  <p>(k) Composite laminate outer surface</p>  <p>(l) Master: Tool outer surface Slave: Composite laminate inner surface</p>
--	---	---

	<p>type: Geometry, Deactivated in this step</p>	 <p>Region: Region: Laminate Set, Tool set and GFOAM set</p>										
<p>Load</p>	<p>(Propagated) Type: Pressure, Region: Laminate upper surface (see Figure) Magnitude=1 Amplitude:</p> <table border="1" data-bbox="508 1123 860 1354"> <thead> <tr> <th>Time (sec)</th> <th>Pressure (Pa)</th> </tr> </thead> <tbody> <tr> <td>0</td> <td>0</td> </tr> <tr> <td>6600</td> <td>96500</td> </tr> <tr> <td>15480</td> <td>96500</td> </tr> <tr> <td>20160</td> <td>0</td> </tr> </tbody> </table>	Time (sec)	Pressure (Pa)	0	0	6600	96500	15480	96500	20160	0	
Time (sec)	Pressure (Pa)											
0	0											
6600	96500											
15480	96500											
20160	0											
<p>Boundary conditions</p>	<p>1. Type: Displacement/Rotation Region: refer figure $U1=U2=0$ (deactivated) 2. Type: Displacement/Rotation</p>											

	<p>Region: refer figure</p> <p>$U_3=0$</p> <p>(deactivated)</p> <p>3. Type: Pore pressure</p> <p>Magnitude=0 (deactivated)</p> <p>4. Type:</p> <p>Displacement/Rotation</p> <p>Region: refer figure</p> <p>$U_3=0$</p> <p>5. Type:</p> <p>Displacement/Rotation</p> <p>Region: refer figure</p> <p>$U_1=0$</p> <p>6. Type:</p> <p>Displacement/Rotation</p> <p>Region: refer figure</p> <p>$U_2=0$</p>	 <p>Region: Laminate Set, Tool set and GFOAM set</p>  <p>Region: Laminate upper surface set</p>  <p>Region: Laminate set</p>  <p>Region: Upper and lower point at center of laminate</p>  <p>Region: lower point at center of laminate</p>
--	--	--

Initial condition	Predefined field: Step-Initial, Region (Propagated)	All components
Field output, History output	Default	
Analysis run	COMPRO plugin → Analysis→Use existing thermo-chemical results→Upload .odb file, Use existing flow-compaction results→Upload .odb file, Run stress-deformation analysis →Submit job	

Appendix C

Dimensions of Composite Boom Tool concepts are provided here in Figure C-1 to C-5. For each concept, the core was sketched in Abaqus. However, the Heat spreader and BMI laminate parts were offset using the core sketch. Heater was not modeled as a part and is shown in the figures below for representation purposes. Note that Heat spreader is not used in the GOAM concepts namely C10, C11 and C12. Apart for that, C10 is similar in construction to C1. C11 and C12 are similar to C2 and C6.

I. Concept C1

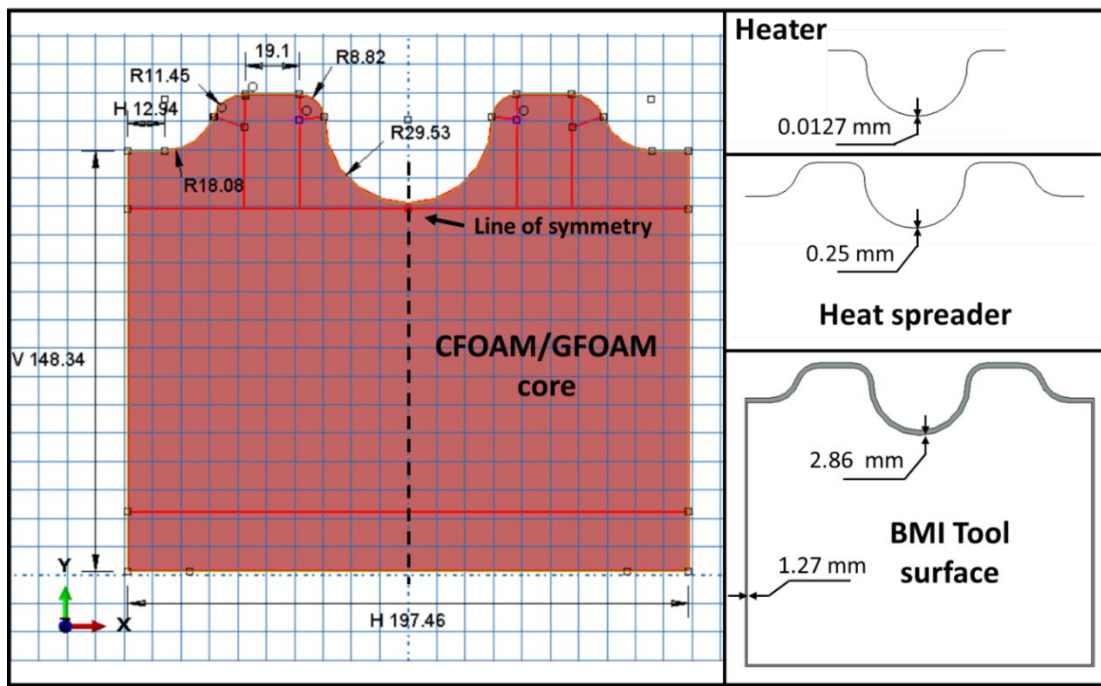


Figure C-1: Dimensions (in mm) of materials used for modeling of C1 concept

II. Concepts C2 and C6

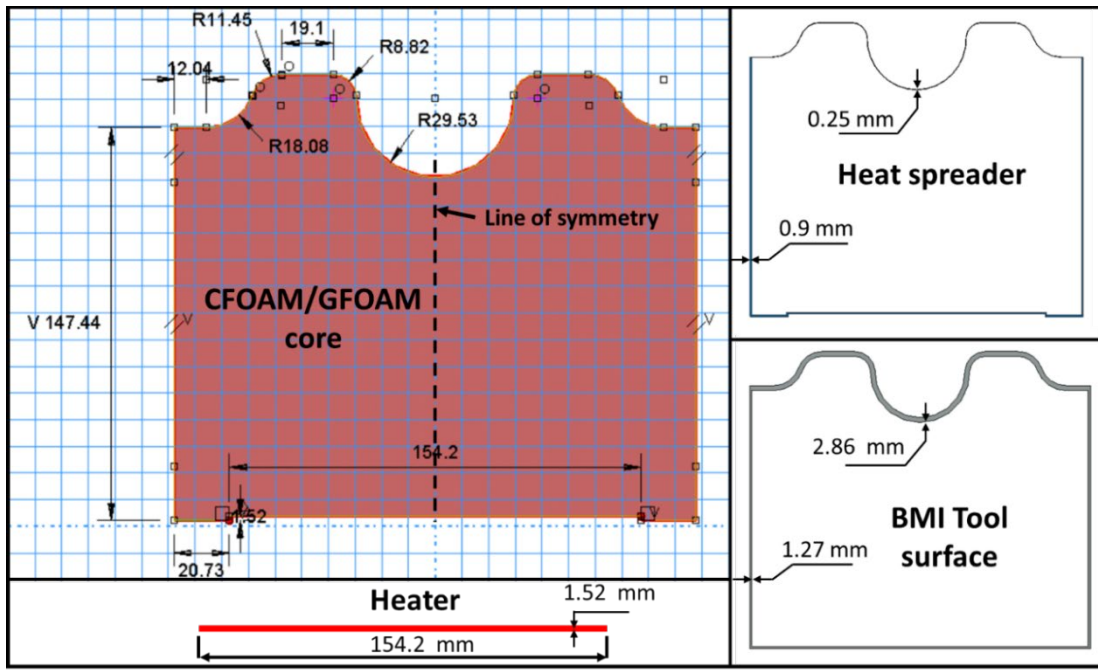


Figure C-2: Dimensions (in mm) of materials used for modeling of C2 and C6 concepts

III. Concepts C3 and C7

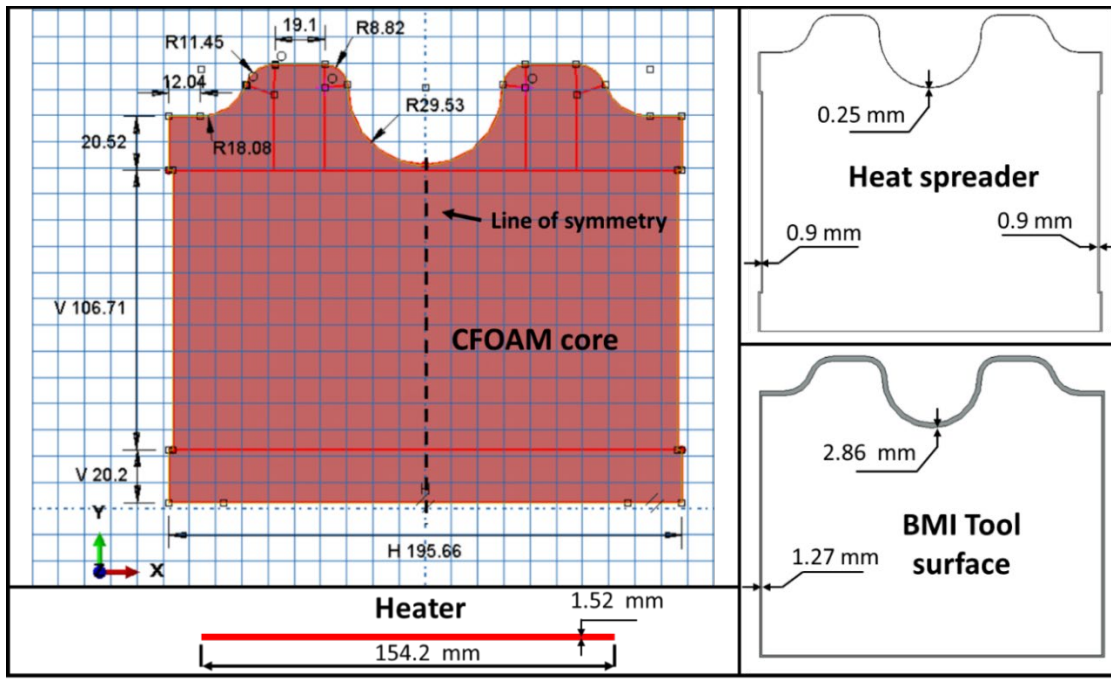


Figure C-3: Dimensions (in mm) of materials used for modeling of 32 and C7 concepts

IV. Concepts C4 and C8

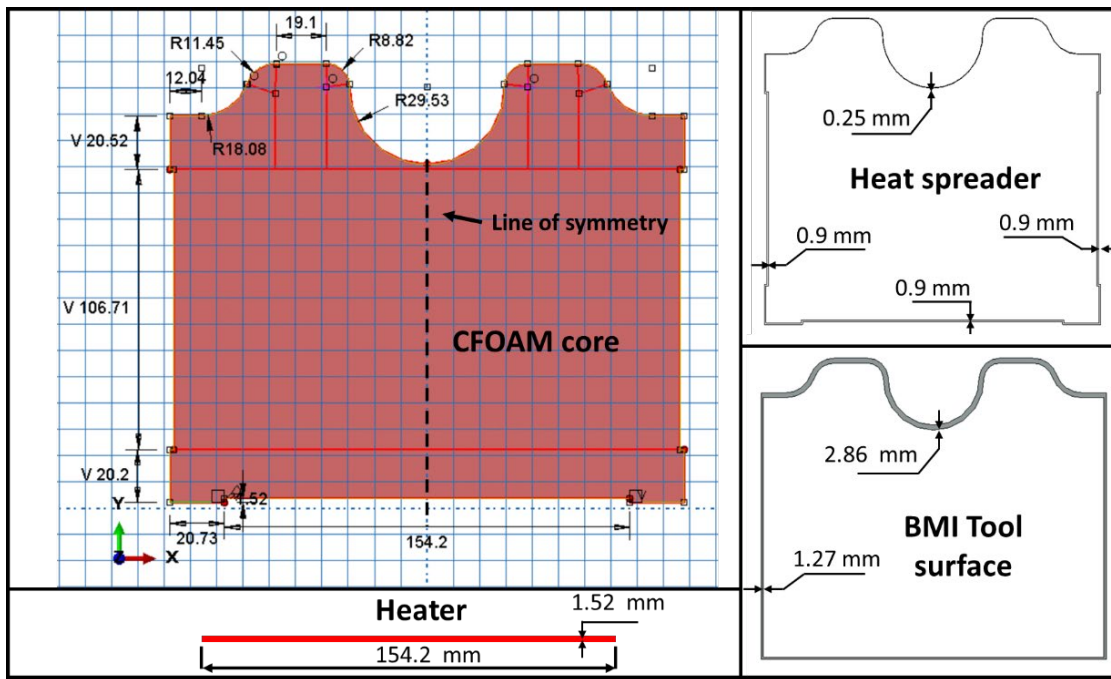


Figure C-4: Dimensions (in mm) of materials used for modeling of C4 and C8 concepts

V. Concepts C5 and C9

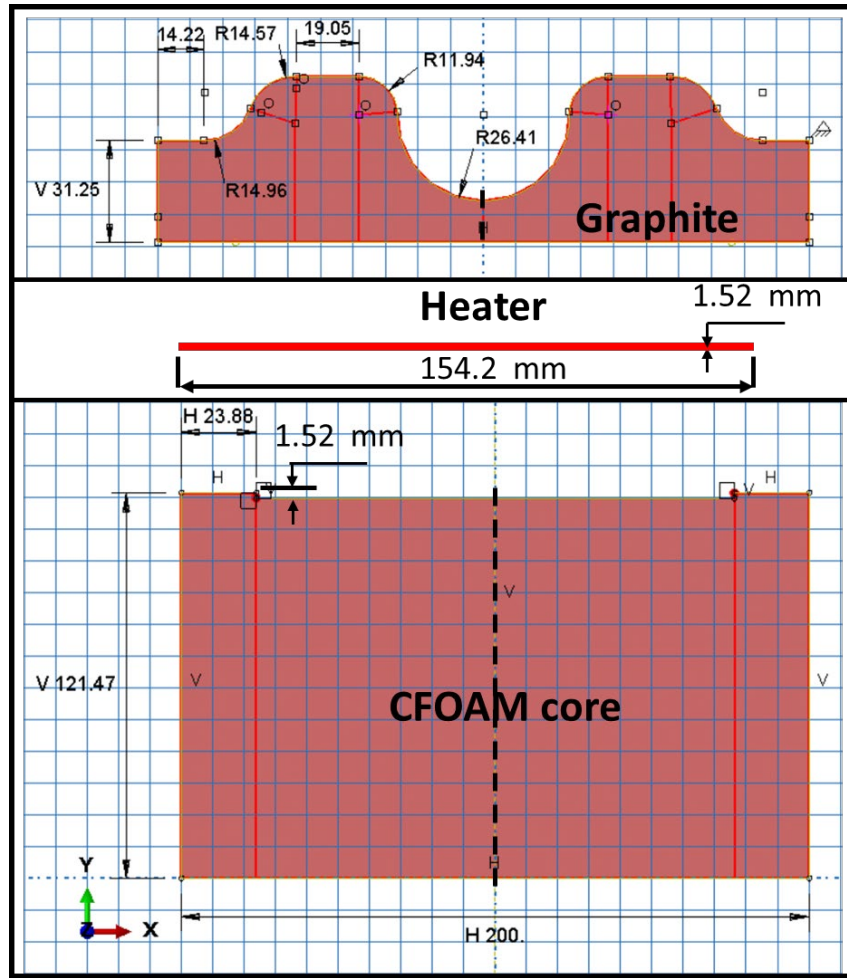


Figure C-5: Dimensions (in mm) of materials used for modeling of C5 and C9 concepts

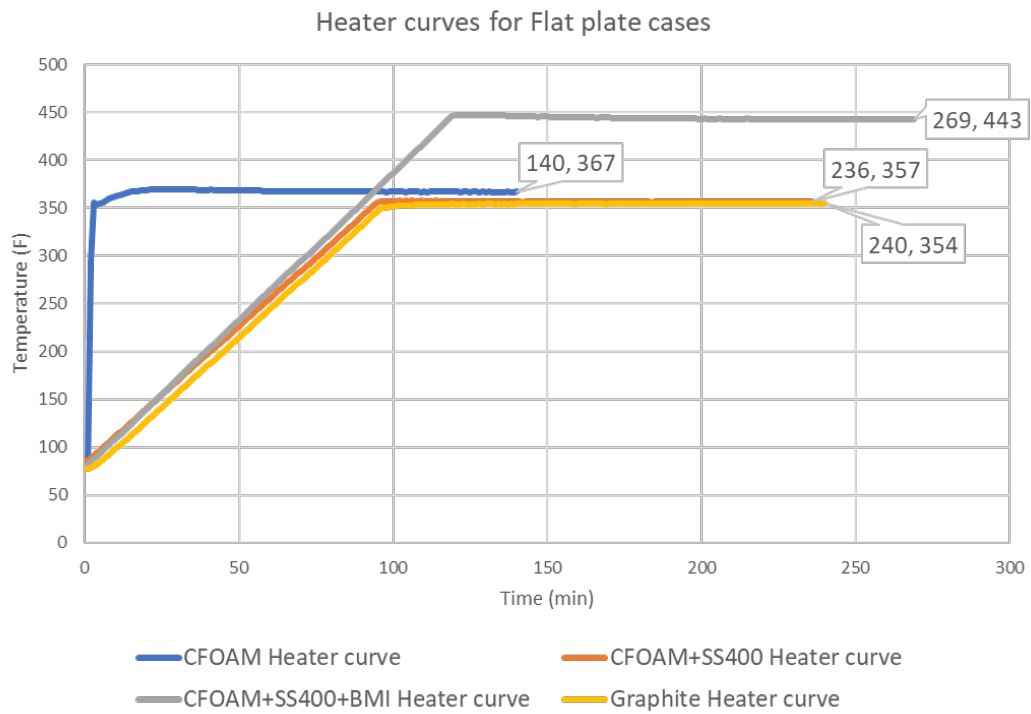


Figure C-6: Heater side thermal profiles for flat plate cases